University of California
Santa Barbara

Experimental and theoretical approaches to trapped matter-wave interferometry and exotic quantum matter

A dissertation submitted in partial satisfaction
of the requirements for the degree

Bachelor of Science
in
Physics

by

Xuanwei Liang

Committee in charge:

Professor David Weld, Chair
Professor Tengiz Bibilashvili

June 2025

The Dissertation of Xuanwei Liang is approved.

Professor Tengiz Bibilashvili

Professor David Weld, Committee Chair

June 2025

Experimental and theoretical approaches to
trapped matter-wave interferometry and exotic quantum matter

by

Xuanwei Liang

It is not about the destination,

but about the journey and the people you meet along the way.

当你的才华不足以支撑起你的野心的时候，你就应该静下心来学习。

When your knowledge is insufficient to meet your ambition,

you should sit down and learn.

Acknowledgements

It is with mixed feelings to complete this last section of the thesis. On one hand, the long, perhaps ungodly long, writing grind has come to a stop, but on the other, it marks the end of a life chapter saying goodbye to many mentors, colleagues, and friends. Many of them have wholeheartedly helped me grow both as a person and as an "amateur physicist". It would be lying if I said that there hadn't been full of ups and downs during my undergrad. Fortunately, many downs occurred at the beginning and the middle of the journey, with everyone pouring support and encouragement till the end.

First and foremost, this thesis would not exist without my advisor, Professor David Weld. I still remember the first time I stepped into your office the summer three years ago. You taught me how a RF box worked and gave me a tour on the lithium machine, where I later spent three years in those exact spots and for which I built many boxes. The patience and scientific enthusiasm (and dry humor) in you shipped the whole team through various difficult times, whether it be the generation transition or the first attempt in seeing an interferometry signal. I have learned, or at least tried to learn, so much from you in how one could be creative and scientifically rigorous as a physicist, as well as how one might become an open-minded leader who genuinely cares about their students. A large portion of my undergrad research trainings and personal developments would not have been possible without meeting you and joining this lab. I must also thank my academic advisor, Professor Tengiz Bibilashvili. It was you who brought me to CCS when I was a naive college sophomore barely knowing anything. I could not say how much I appreciated when you reached out and invited me to visit UCSB and to attend your lecture. The trust you had in me back then is still beyond my imagination to this date. When I said I was interested in AMO physics, the fact that you immediately emailed every AMO professor at UCSB to find research opportunities for me demonstrates the

amount of caring you have towards students. Every advice you had given proved to be valuable insights that I would have not known otherwise. From your CCS cohort, I am so fortunate to meet some of the brightest and most driven students that I have no doubt to be my lifelong friends and colleagues. I can confidently argue that all my achievements at UCSB can be attributed to David and Dr. B, who played critical and transforming roles in altering my life trajectory. I am extremely glad that there were many and there will be many more who have been and continue to be in this life-changing UCSB "pipeline".

To Dr. Xiao Chai, the person who single-handedly taught me the most bread and butter ingredients in an AMO experiment, the amount of knowledge you know at every aspect of the experiment is astonishing. I am so grateful to slowly learn piece by piece with the non-stopping Slack notifications throughout days and nights. You have not only presented me the knowledge themselves, but also the methods to independently do science when we walk into an unknown territory and encounter unfamiliar stuff. I am more than happy if I could walk away with ten percent of everything you know. To Dr. Toshihiko Shimasaki, I truly enjoyed every late-night interaction we had when we chatted everything from science to gossips to anecdotes. I wish I could have more time learning from you about science than distracting you to talk about random stuff. You represented the lab spirits for a long time and left truly remarkable positive influence on the lab. I am sure we will meet again in the future to continue our random discussion. To Dr. Peter Dotti, I had always impressed by your patience and clarity in explaining fundamental concepts and electronics to junior students like myself. I extremely respect your desire to deeply understand every subject over light exposure on them; it strikes me to dive in and truly have a good grasp on various topics. I am glad that you have found your callings, and I look forward to hearing the Dotti contributions in energy with all the expertise you have developed along the way. I still cannot believe that putting the Earth on air conditioners is not a feasible idea for once and for all solving the energy crisis. To

Dr. Ethan Quinn Simmons, I am very grateful for all the encouragements and mentoring you had given to me when I was lost in the sea of AMO physics. You could always find intuitive explanations for my questions, despite my lack of foundational knowledge. You inspired me through our conversations that everyone could do great things as long as we keep trying and put in hard work and efforts. To Dr. Roshan Sajjad, my first mentor in the Weld lab, your creativity and optimism are something I wish I could have. It was a pleasure overlapping with you and seeing how you approach science and life in earnest and stress-free fashions. You amazing writing and editing skills are also critical in many of my applications.

I must also acknowledge my lithium teammates who sincerely treat me as a colleague instead of a trouble-making undergrad. I have been a slow learner in the past three years, seizing every opportunity in battling with this giant, complicated cold-atom machine, which necessarily meant that I must have had stopped progress at some points. I hope that I was able to contribute, no matter how slightly, to the experiment and to the team in any positive ways. To Jeremy Tanlimco, you invitation to running the machine was the starting point for me to see how all my projects (boxes) are really connected to the machine and could potentially upgrade it into a better state. Since then, I have been able to zoom out and view everything in a bigger picture. You consistent organizations of game night and Wiki editing, as well as monthly snack supplies, are important fuels to keep us productive. It was also always fun to discuss our common Asian heritages and discover how similar they could be. To Eber Nolasco-Martinez, I always appreciate how you often check in with junior students and patiently explain ideas in details. You always encourage everyone to explore different ideas on the machine and put out the best efforts in coordinating machine schedule and planing with the team. Despite my initial viability doubts, your deep and creative insights have saved us many times in numerous parameter space scans when debugging the machine, and that is something I wish I could develop in

my PhD. To Nicole Halawani, though we did not overlap for a long time, I have no doubt that the machine will be in great hands. Your organizing and stylish editing skills are unique additions to the lithium machine toolkit (on top of the light mass and Feshbach resonance). It is great to see that you have been increasingly more involved in the team and I look forward to all the amazing stuff you will do in this fantastic platform. To Eric Zhu, a.k.a the secret theorist, keep up the good work! Your theoretical perspectives are often very valuable in the team. Pursue what you find the most interesting and enjoy the excitement of combining experiment and theory.

I am also grateful for having the opportunity of knowing and learning from everyone in the Weld lab. To Yifei Bai, you are the walking library in our lab and the go-to person for any AMO literature. I am amazed by your big picture analyses and plannings. Although we are not in the same team, your scientific interest delocalizes you into all three experiments and you effectively are involved in many technical and scientific discussions of the lithium team. In addition, despite your constant denials of being a theorist, your analytical and numerical capabilities push our understandings beyond experimental results. To Anna Dardia, we joined the lab at around the same time, and it has been awesome to see you leading all the group's ultrafast efforts. I enjoyed chatting with you about classes and crazy undergrad anecdotes, especially during our increased interactions in the core when the chiller became problematic. To Petros Kousis, it was fun getting to know you and playing Seven Wonders together. You intrigued my interest in Cyprus, and I will have to check it out at some point now. To Sidd Mukherjee, it was very fond memory to have late-night chat in Fort Worth and thank you for all the graduate school application suggestions you had. To Shravan Ramanand, I wish we could have overlapped longer together. You have been doing great work, and I am sure you will be a much stronger undergrad researcher than me soon. To Jared Pagett, I have always been able to learn something from you in most of our conversations. Your great communications really

leverage the whole group to solve collectively each experiment's technical problems. It was rather memorable to have one of the silliest conversation that night when we found out that three-year efforts of making potassium BECs could easily go to waste if inappropriate phase contrast imaging actions are taken. To Jeremy Estes, the strongest machinist with the largest biceps, I am so grateful to have you machined countless back panels for my boxes. It was so cool hearing about your pre-industry and academy experience and interesting visits to China. To Madeleine Bow Jun Leibovitch, our paths did not cross often except the "rare" occasions of me going into the potassium room borrowing various components and cables, for which the entire K team has been particularly generous. To Jing-Wei Yang, your yo-yo tricks are just as amazing as your physics understandings. I appreciate for all the homework helps during the many-body physics sequence, without which I cannot imagine getting through the classes. To Samyuktha Ramanan, it has been fun and very helpful to have an "identical" person walk through every step together – building identical boxes, navigating through the steep AMO learning curve, and applying for graduate schools at the same time. To Jack Kingdon, an interesting British character, I enjoyed many of our conversations and especially admired your determined interests in pursuing space technology. Witnessing all your growth and your persistence in field stabilization, I am excited to hear about your future contributions to space explorations.

I must express my gratitude to all the mentors I had before I transferred to UCSB. Professor Guillem Pratx offered me the first physics research experience at Stanford, with Dr. Hieu Nguyen being a fantastic mentor giving me supports and career advice. Professor Yong Zheng further expanded my horizons on research and showed me the importance of literature review. Professor David Marasco and Professor Frank Cascarano provided me the necessary foundations in physics and research to make everything above possible. Sophia Kim and the Foothill Science Learning Institute hosted all the valuable research experiences above so that newbies like me were able to benefit from all these

amazing resources.

It has been so important to have a group of like-minded friends to share this journey. To the Circus: Aidan Ireland, Filippo Delzanno, Hari Stoyanov, Luka Sever-Walter, Reef Sweeney, and Simon Blanch, you have really convinced me that physics is only fun when doing it together. I would not have been the same person without you guys (and the beer balls). All the gym workout sessions, homework and lab grinds, presentation and interview practices, application reviews, and the late-night chats and games will always be some of my most precious memories, constituting a large part of my undergrad life outside of the lab. To Aaron Huang, I enjoyed getting to know you and hanging out together, especially when I first came to UCSB. You have been a reliable and genuine friend from whom I learned many good qualities. To Tommy Dan, my dinner buddy, it has been fun comparing ions and atoms, precision measurements and many-body physics, and exploring different restaurants in IV and Goleta. Your curiosity and determination is infectious and I wish you to be the first person to measure non-zero EDM.

I must thank my partner Isabelle for her patient and her understandings of spending countless hours in the library and cafés throughout the last few years. I cannot wait for continuing the many more life chapters and experiencing all little daily moments together. Lastly, there are no words I can use to describe everything my parents have done for me. They sacrificed their comfortable life in exchange for giving me a better future. Their unconditional love and supports are the reasons I can freely adventure in the physics world.

Curriculum Vitæ

Xuanwei Liang

Education

2025	B.S. in Physics (Expected), University of California, Santa Barbara.
2022	A.S.T in Physics, Foothill College.

Publication

Chai X., Tanlimco J.L., Nolasco-Martinez E., **Liang X.**, Simmons E.Q., Zhu E., Sajjad R., Mas, H., Halawani N., & Weld D.M., "Continuously trapped matter-wave interferometry in magic Floquet-Bloch band structures," arXiv:2506.11881v1 (2025).

Natarajan A., Khan S., **Liang X.**, Nguyen H., Das N., Anders D., Malik N., Oderinde O.M., Chin F.T., Rosenthal E.L. & Pratx G., "Preclinical evaluation of 89Zr-Panitumumab for biology-guided radiotherapy," *Int. J. Radiat. Oncol. Biol. Phys.* 116(4), pp. 927-934 (2023).

Awards

2025	UCSB Physics Academic Excellence Award
2025	NSF Graduate Research Fellowships Program (GRFP)
2024	UCSB CCS Summer Undergraduate Research Fellowship (SURF)
2024	Barry Goldwater Scholarship
2024	UCSB CCS Traveling Undergraduate Research Fund (TURF)
2024	UCSB Physics Conner Family Undergraduate Travel Grants
2023	UCSB Physics Worster Summer Research Fellowship
2022	Foothill Academic Achievement Scholarship
2022	Foothill Prip Memorial Scholarship
2022	Foothill Donald M. and Shirley M. Hewitt Scholarship

Abstract

Experimental and theoretical approaches to
trapped matter-wave interferometry and exotic quantum matter

by

Xuanwei Liang

Driven quantum degenerate gases present a rich landscape for understanding quantum dynamics, from the perspectives of precision quantum sensing and exploration of fundamental many-body quantum phenomena. In this thesis, I will discuss relevant experimental efforts with Bose condensed lithium in amplitude modulated optical lattices. In particular, I will first describe experimental and theoretical techniques used for controlling and understanding quantum gas systems with tunable interaction and periodic driving. I will then introduce a new class of quantum sensor based on programmable trapped matter-wave interferometry in magic Floquet-Bloch structures. I will also outline numerical results towards realizing a quantum many-body Kapitza pendulum.

Contents

Chapter 1

Introduction

Since the birth of quantum mechanics more than 100 years ago, the world of quantum physics has been constantly unveiled by humans through many cycles of revolution in our understanding. Throughout the entire exploration, atoms played a key role serving as one of the ultimate experimental testbeds for new theoretical possibilities. The history of atomic physics is very much tied to the development of quantum mechanics, starting from the explanation of discrete atomic energy spectra, to the observation of lamb shift, to the modern application of atomic clocks and neutral atom quantum computers. Today society is witnessing a significant breakthrough in quantum technology and many aspects of applying quantum mechanics to real-world application are related to modern atomic, molecular, and optical (AMO) physics experiments.

AMO physics explores matter-matter and light-matter interactions. In particular, the field of cold atoms has reached unprecedented quantum control, since the two major breakthroughs of laser cooling and the experimental realization of Bose-Einstein condensates (BECs). The rich collection of experimental techniques developed over the years has been exploited for obtaining some of the best metrological measurements to-date, constructing state-of-the-art quantum computers, and studying fundamental quantum

many-body phenomena.

One such technique, the optical lattice, has opened up new pathways to simulate generic Hamiltonians that are analytically or numerically intractable, as well as to challenge existing sensing precision. Neutral atoms in optical lattices utilize this flexible feature to engineer many-body Hamiltonians that can describe electrons in solids, establishing many successes in quantum simulation and quantum metrology [1].

More recent experimental efforts are devoted to probing non-equilibrium dynamics for quantum many-body systems, thanks to the experimentally accessible timescales and a wide range of fully tunable experimental parameters in cold atom experiments. The slow relaxation rate and controllable interaction make it convenient to observe long time evolution and realize different quantum phases of matter. One topic that is of significant interest is driven quantum systems, manipulated in a time periodic manner. Such coherent control of a system's Hamiltonian is known as Floquet engineering. Combined with optical lattices, it offers an additional dimension of periodicity that gives rise to exciting realizations, such as dynamic localization, artificial gauge fields, and topological non-trivial structures. The powerful interplay between spatial and temporal orderings along with tunable interaction has the potential to address many unexplored questions in non-equilibrium many-body quantum dynamics.

1.1 Dissertation Overview

This dissertation discusses most of my work completed in the Weld lab at UCSB for the ^{7}Li apparatus, including experimental upgrades, numerical simulations, and science projects that I have been fortunate to be involved in. It is intended to serve as a documentation and reference for future generations of the lithium team.

- **Chapter 1** provides a brief introduction to AMO physics and the significance of

research done in this community.

- **Chapter 2** contains some background information and fundamental atomic physics necessary for the rest of the dissertation.
- **Chapter 3** discusses a variety of electronic projects integrated to the lithium machine for future references.
- **Chapter 4** includes some optic components integrated to the lithium machine for future references.
- **Chapter 5** introduces some standard numerical simulation techniques used in BEC experiments, especially concerning spatially and temporally periodic Hamiltonians.
- **Chapter 6** reports experimentally a trapped atom interferometer with Floquet-Bloch bands.
- **Chapter 7** describes some preliminary numerical simulations for the realization of a quantum many-body Kapitza pendulum.
- **Appendix** A gives an introductory review on quantum chaos and thermalization.

1.2 Permissions and Attributions

1. The content of Chapter 6 is the result of a collaboration with the Lithium team in the Weld group.

Chapter 2

Background

2.1 Bose-Einstein Condensate

Bose-Einstein condensation was first theoretically predicted by Einstein in 1924, considering a gas of non-interacting, massive bosons [2]. One remarkable feature of Bose-Einstein condensates (BECs) is the macroscopic occupation of the ground state of the quantum system.

2.1.1 Basic Ideas

One of the intuitive ways to imagine the phase transition into BECs is considering the particles' de Broglie wavelength:

$$\lambda_{dB} = \frac{h}{p} = \frac{h}{\sqrt{2mk_BT}} \tag{2.1}$$

We can define a critical temperature T_c at which the BEC transition occurs. For a uniform Bose gas in a three-dimensional box of volume V, the critical temperature T_c is

[3]:

$$T_c \approx 3.31 \frac{\hbar^2 n^{\frac{2}{3}}}{m} \tag{2.2}$$

where $n = \frac{N}{V}$ is the number density.

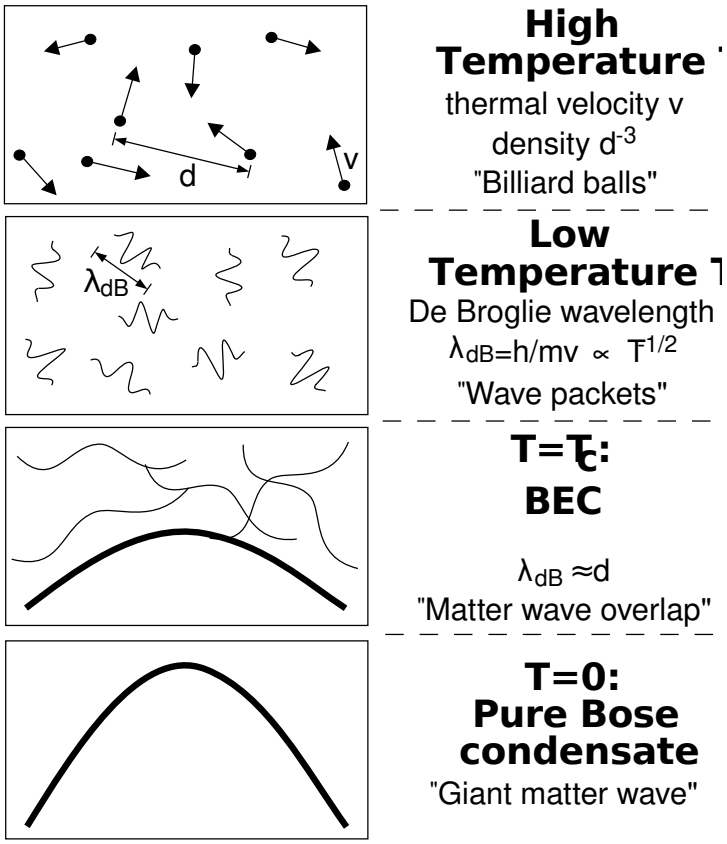

Figure 2.1: The transition from thermal "billiard balls" at high temperature to matter wave Bose-Einstein condensate below the critical temperature T_c. Figure retrieved from [4]

Fig. 2.1 shows the phase transition from thermal atoms to BECs. When the system is at high temperature $T >> T_c$, the particles' de Broglie wavelength is extremely small compared to the interparticle spacing. As the temperature decreases to the critical temperature $T \approx T_c$, the de Broglie wavelength becomes comparable to the interparticle spacing, and the particle's wave nature is more prominent. The matter waves overlap and become indistinguishable from one another. At zero temperature, we obtain a pure BEC

with the entire system in the ground state. At a finite temperature T, the condensate fraction n_0 is given by:

$$n_0 = \frac{N_0}{N} = 1 - \left(\frac{T}{T_c}\right)^{\frac{3}{2}} \tag{2.3}$$

with N_0 being the number of particles in the ground state and N the total particle number. Eqn. 2.3 is valid for particles in a homogeneous box potential in three dimensions [3].

The first experimental realizations of BECs in dilute atomic gases were in 1995 [5, 6]. Since then, there has been a large development in both theoretical understandings and experimental techniques about BECs. The experimental procedure in BEC preparations are well described in the literature, which typically involved laser cooling and trapping, as well as evaporative cooling [7, 3, 4]. The BEC production method for the lithium apparatus can be found in the group theses [8, 9, 10, 11, 12].

2.1.2 Gross–Pitaevskii Equation

Here I briefly introduce the interacting Bose-Einstein condensate with a mean-field approximation, following the discussion from [3]. In a BEC, all bosons are in the same single-particle state $\phi(\mathbf{r})$, and the overall many-body wavefunction for the N-particle system is:

$$\Psi(\mathbf{r}_1,\ \mathbf{r}_2, \cdots,\ \mathbf{r}_N) = \prod_{i=1}^{N} \phi(\mathbf{r}_i) \tag{2.4}$$

The effective Hamiltonian for this N-particle system with a two-body contact interaction in position space is:

$$H = \sum_{i=1}^{N} \left[\frac{\mathbf{p}_i^2}{2m} + V(\mathbf{r}_i)\right] + g \sum_{i<j} \delta(\mathbf{r}_i - \mathbf{r}_j) \tag{2.5}$$

with $V_{\mathbf{r}}$ being the external potential and g the two-particle interaction. In the momentum-space representation, it is a constant given by:

$$g = \frac{4\pi\hbar^2 a_s}{m} \tag{2.6}$$

where a_s is the s-wave scattering length, typically controlled by a magnetically-tuned Feshbach resonance [13]. Around a Feshbach resonance, the s-wave scattering length has the form of:

$$a_s(B) = a_{\text{bg}}\left(1 - \frac{\Delta}{B - B_0}\right) \tag{2.7}$$

where a_{bg} is the background scattering length, B_0 is the magnetic field at the Feshbach resonance, and Δ is the width of the resonance.

The energy functional of the system can be written as:

$$E(\psi) = \int d\mathbf{r}\left[\frac{\hbar^2}{2m}|\nabla\psi(\mathbf{r})|^2 + V(\mathbf{r})|\psi(\mathbf{r})|^2 + \frac{1}{2}g|\psi(\mathbf{r})|^4\right] \tag{2.8}$$

with the wavefunction of the condensed state $\psi(\mathbf{r})$ and the particle density $n(\mathbf{r})$ defined as:

$$\psi(\mathbf{r}) = N^{\frac{1}{2}}\phi(\mathbf{r}) \tag{2.9}$$

$$n(\mathbf{r}) = |\psi(\mathbf{r})|^2 \tag{2.10}$$

Using Lagrange multipliers to minimize the quantity at fixed chemical potential μ gives the time-independent Gross-Pitaevskii equation:

$$\left[-\frac{\hbar^2}{2m}\nabla^2 + V(\mathbf{r}) + g|\psi(\mathbf{r})|^2\right]\psi(\mathbf{r}) = \mu\psi(\mathbf{r}) \tag{2.11}$$

This resembles the Schrodinger equation with an extra non-linear, mean-field interaction term $\propto |\psi(\mathbf{r})|^2$. For a non-interacting system (g=0), Eqn. 2.11 recovers the time-independent Schrodinger equation. Similarly, the dynamics of BEC is governed by the time-dependent Gross-Pitaevskii equation:

$$\left[-\frac{\hbar^2}{2m}\nabla^2 + V(\mathbf{r}) + g|\psi(\mathbf{r},\ t)|^2\right]\psi(\mathbf{r},\ t) = i\hbar\frac{\partial\psi(\mathbf{r},\ t)}{\partial t}. \tag{2.12}$$

2.1.2.1 Thomas-Fermi Approximation

For sufficiently large atomic clouds, one way to approximate the ground state is by neglecting the system's kinetic energy. Then, Eqn. 2.11 becomes:

$$\left[V(\mathbf{r}) + g|\psi(\mathbf{r})|^2\right]\psi(\mathbf{r}) = \mu\psi(\mathbf{r}) \tag{2.13}$$

This has a solution when:

$$V(\mathbf{r}) \quad + \quad g|\psi(\mathbf{r})|^2 = \mu \tag{2.14}$$

$$\rightarrow n(\mathbf{r}) \quad = \quad |\psi(\mathbf{r})|^2 = \frac{\mu - V(\mathbf{r})}{g} \tag{2.15}$$

This is known as the Thomas-Fermi approximation. The correponding Thomas-Fermi radii are:

$$R_i^2 = \frac{2\mu}{m\omega_i^2} \tag{2.16}$$

with ω_i being the i-th dimension trapping angular frequency of an anisotropic three-dimensional harmonic oscillator potential.

2.1.2.2 One-Dimensional Nonpolynomial Nonlinear Schrodinger Equation

In a true one-dimensional system, dimensionality reduction can be performed to the three-dimensional Gross-Pitaevskii equation and obtain a one-dimensional equation of motion. Here I will present one example for the cigar-shaped BECs, following the derivation in [14].

For a cylindrical symmetric potential $V($**r** with the form of:

$$V(\mathbf{r},\ t) = V(x,\ t) + \frac{1}{2}m\omega_\perp^2(y^2+z^2) \tag{2.17}$$

where the transverse confinement is harmonic and the axial potential is $V(x)$. We can minimize the energy functional using a trial wavefunction:

$$\begin{aligned} \psi(\mathbf{r},\ t) &= f(x,\ t)\cdot g(y,\ z,\ t;\ \sigma(x,\ t)) & (2.18)\\ g(y,\ z,\ t;\ \sigma_(x,\ t)) &= \frac{1}{\sqrt{\pi}\sigma(x,\ t)}e^{-\frac{y^2+z^2}{2\sigma^2(x,\ t)}} & (2.19)\end{aligned}$$

where the transverse components are assumed to be a Gaussian. After substituting the ansatz into the functional and working through the derivation, one finds the so-called time-dependent nonpolynomial nonlinear Schroginer equation (1D NPSE):

$$\begin{aligned}\Bigg[&-\frac{\hbar^2}{2m}\frac{\partial^2}{\partial x^2} + V(x,\ t) + \frac{gN}{2\pi l_\perp^2}\frac{|f(x,\ t)|^2}{\sqrt{1+2a_sN|f(x,\ t)|^2}} \\ &+ \frac{\hbar\omega_\perp}{2}\left(\frac{1}{\sqrt{1+2a_sN|f(x,\ t)|^2}} + \sqrt{1+2a_sN|f(x,\ t)|^2}\right)\Bigg] f(x,\ t) = i\hbar\frac{\partial f(x,\ t)}{\partial t}\end{aligned} \tag{2.20}$$

where $l_\perp$ is the transverse oscillator length defined as $l_\perp = \frac{\hbar}{m\omega_\perp}$. In the weakly limiting case $a_s N|f|^2 << 1$, Eqn. 2.20 reduces to:

$$i\hbar\frac{\partial f(x,\ t)}{\partial t} = \left[-\frac{\hbar^2}{2m}\frac{\partial^2}{\partial x^2} + V(x,\ t) + \frac{gN}{2\pi l_\perp^2}|f(x,\ t)|^2\right] f(x,\ t) \tag{2.21}$$

we can define the new one-dimensional interaction coefficient as $g_{1\mathrm{d}} \equiv \frac{g}{2\pi l_\perp^2}$, the reduced 1d NPSE becomes:

$$i\hbar\frac{\partial f(x,\ t)}{\partial t} = \left[-\frac{\hbar^2}{2m}\frac{\partial^2}{\partial x^2} + V(x,\ t) + g_{1\mathrm{d}}N|f(x,\ t)|^2\right] f(x,\ t) \tag{2.22}$$

This equation will be used for simulating one-dimensional interacting BEC dynamics throughout the thesis.

2.2 Optical Lattice

Optical lattices are one of the most essential ingredients for many material in this thesis, and generically for the study of many-body physics with ultracold atoms [1, 15]. An optical lattice is an optical standing wave potential experienced by the atoms. Similar to an optical dipole trap [16], an optical lattice is generated through a far off-resonant, red-detuned laser field, where the atoms are trapped through a effect known as the AC Stark shift. Trapping through the AC Stark shift is known as an optical trap, as opposed to a radiation-pressure trap (e.g. magneto-optical trap) or a magnetic trap. In this section, I will discuss the mechanism behind the AC Stark shift, and the one-dimensional optical lattice and its band structure.

2.2.1 AC Stark Shift

The AC Stark shift states how an atom with an electric dipole moment interacts with an oscillating electromagnetic field. It can be explained by both a classical and a quantum mechanical models, when the atom is modeled as a classical dipole or with a electric dipole operator in quantum mechanics [3].

2.2.1.1 Classical Model

Assuming an atom is inside an electromagnetic field generated by a laser, the dominant atom-light interaction is the electric dipole interaction. The electric field of the laser $\mathbf{E}$ induces an atomic dipole moment $\mathbf{d}$ that oscillates at the laser frequency ω,

$$\mathbf{d} = \alpha(\omega)\mathbf{E} \tag{2.23}$$

where $\alpha(\omega)$ is the complex polarizability. The potential the atom experiences is:

$$\begin{aligned} V(\mathbf{x}) &= -\frac{1}{2} < \mathbf{d} \cdot \mathbf{E}(\mathbf{x}) >_t \\ &= -\frac{1}{2\epsilon_0 c}\mathrm{Re}(\alpha) I(\mathbf{x}) \end{aligned} \tag{2.24}$$

where $< ... >_t$ denotes the time-average. The classical dipole force is introduced as

$$\begin{aligned} \mathbf{F}(\mathbf{x}) &= -\nabla V(\mathbf{x}) \\ &= \frac{1}{2\epsilon_0 c}\mathrm{Re}(\alpha)\nabla I(\mathbf{x}). \end{aligned} \tag{2.25}$$

2.2.1.2 Quantum Mechanical Model

For an electric dipole interaction with the dipole operator $\mathbf{d}$, the Hamiltonian is:

$$\begin{aligned} H' &= -\mathbf{d}\cdot\mathbf{E}(\mathbf{x},t) \\ &= -\mathbf{d}\cdot\mathbf{E}(\mathbf{x})\cos(\omega t) \\ &= -\frac{\mathbf{d}\cdot\mathbf{E}(\mathbf{x})}{2}\left(e^{i\omega t}+e^{-i\omega t}\right) \end{aligned} \tag{2.26}$$

By perturbation theory, the first order correction to the ground state energy is zero, and the second order correction yields:

$$\begin{aligned} \Delta\epsilon_g &= -\sum_e \frac{|\langle e|H'|g\rangle|^2}{E_e-E_g} \\ &= \sum_e |\langle e|\mathbf{d}\cdot\hat{\mathbf{E}}|g\rangle|^2|E|^2\left(\frac{1}{\epsilon_g-\epsilon_e-\hbar\omega}+\frac{1}{\epsilon_g-\epsilon_e+\hbar\omega}\right) \\ &= -\alpha(\omega)|E|^2 \\ &= -\frac{1}{2}\alpha(\omega)<|E|^2>_t \end{aligned} \tag{2.27}$$

with the $<...>_t$ being the time average, and the polarizability $\alpha(\omega)$ is:

$$\begin{aligned} \alpha(\omega) &= \sum_e \langle e|\mathbf{d}\cdot\hat{\mathbf{E}}|g\rangle|^2\left(\frac{1}{\epsilon_g-\epsilon_e-\hbar\omega}+\frac{1}{\epsilon_g-\epsilon_e+\hbar\omega}\right) \\ &\approx \frac{\langle e|\mathbf{d}\cdot\hat{\mathbf{E}}|g\rangle|^2}{\epsilon_e-\epsilon_g-\hbar\omega} \end{aligned} \tag{2.28}$$

where in the second expression, a rotating approximation is used hence neglecting the second term in the parenthesis. Also, only the first excited state is considered since it contributes the largest correction.

Note that here I did not consider the finite lifetime of the excited states from spontaneous emission. Accounting for this, we would need to include a complex energy term

in the second order correction ϵ_g that is proportional to Γ_e, the lifetime for the excited state $|e\rangle$:

$$\Delta\epsilon_g = V_g - i\frac{\hbar}{2}\Gamma_e \tag{2.29}$$

Then the polarizability becomes complex:

$$\alpha(\omega) \approx \frac{\langle e|\,\mathbf{d}\cdot\hat{\mathbf{E}}\,|g\rangle\,|^2}{\epsilon_e - i\frac{\hbar}{2}\Gamma_e - \epsilon_g - \hbar\omega} \tag{2.30}$$

The real part of the correction ϵ_g is the potential V_g the atom experiences:

$$V_g = -\frac{1}{2}\mathrm{Re}(\alpha(\omega)) < |E|^2 >_t \tag{2.31}$$

where

$$\mathrm{Re}(\alpha(\omega)) \approx \frac{(\epsilon_e - \epsilon_g - \hbar\omega)|\,\langle e|\,\mathbf{d}\cdot\hat{\mathbf{E}}\,|g\rangle\,|^2}{(\epsilon_e - \epsilon_g - \hbar\omega)^2 + (\frac{\hbar}{2}\Gamma_e)^2} \tag{2.32}$$

Defining the detuning as the difference between laser frequency ω and the resonant frequency ω_0 as $\delta = \omega - \omega_0$, Eqn. 2.31 could be simplified to:

$$V_g = \frac{\hbar\Omega^2\delta}{\delta^2 + \frac{\Gamma_e^2}{4}} \tag{2.33}$$

where Ω is the Rabi frequency, defined as $\Omega = \frac{|\langle e|\mathbf{d}\cdot\mathbf{E}|g\rangle|}{\hbar}$.

For both classical and quantum mechanical models, we see that the dipole potential is proportional to $|E|^2$, and is therefore, proportional to the intensity I of the oscillating electric field. In addition, Eqn. 2.33 shows that the potential V_g is attractive when the detuning δ is negative, or the laser frequency ω is red detuned / smaller relative to the atomic resonant frequency ω_0. In this case, the location of an intensity maximum corresponds to the potential minimum, so the atoms would be attracted to the intensity maximum. Conversely, the potential V_g becomes repulsive if the detuning δ is posi-

tive, and the laser frequency ω is blue detuned / larger relative to the atomic resonant frequency ω_0.

2.2.2 Band Structure

2.2.2.1 Bloch's Theoreom

For a particle in a spatially periodic potential $V(x)$, where it is invariant under the discrete spatial transformation $x \to x + a$, the Hamiltonian is written as:

$$H = \frac{p^2}{2m} + V(x) \tag{2.34}$$

We also define the translation operator T_a by

$$T_a \equiv e^{-i\frac{p}{\hbar}a} \tag{2.35}$$

$$T_a\psi(x) = \psi(x-a) \tag{2.36}$$

Since the potential $V(x)$ has a periodicity of a, the translation operator T_a commutes with the Hamiltonian H, and there is a set of basis states that simultaneously diagonalizes both T_a and H.

Bloch's theorem [17] states that the set of simultaneous eigenstates to both T_a and H is given by:

$$\psi_{nq}(x) = e^{i\frac{q}{\hbar}x}u_{nq}(x) \tag{2.37}$$

where q is known as the quasimomentum and n is called the band index. $\psi_{nq}(x)$ is called the Bloch state, and $u_{nq}(x)$ is the corresponding Bloch function with the property: $u_{nq}(x) = u_{nq}(x+a)$.

2.2.2.2 1D Optical Lattice

Now we consider a Hamiltonian with an one-dimensional lattice potential:

$$H = \frac{p^2}{2m} - V_0 \cos^2(k_L x) \tag{2.38}$$

where V_0 is called the lattice depth, and H is invariant under the transformation $x \to x + a$, and thus Bloch's theorem applies. a is known as the lattice constant, and $k_L = \frac{2\pi}{\lambda} = \frac{\pi}{a}$ is the reciprocal lattice constant. The characteristic energy scale for Eqn. 2.38 is the recoil energy $E_R \equiv \frac{\hbar^2 k_L^2}{2m}$. Applying Bloch's theorem, we find the solutions of the lattice Hamiltonian to the time-independent Schrodinger's equation (TISE):

$$\begin{aligned} H\psi_{nq} &= E_{nq}\psi_{nq} \\ H[e^{iqx}u_{nq}] &= E_{nq}[e^{iqx}u_{nq}] \end{aligned} \tag{2.39}$$

with the ansatz $\psi_{nq} = e^{i\frac{q}{\hbar}x}u_{nq}$. The general solution to the time-dependent Schrodinger's equation (TDSE) is:

$$\psi(x,\ t) = \sum_{n,\ q} a_{nq} e^{-\frac{i}{\hbar}E_{nq}t}\psi_{nq}(x) \tag{2.40}$$

Expanding Eqn. 2.39 gives:

$$\left[\frac{(p+q)^2}{2m} - \frac{V_0}{2}\cos(2k_L x) - \frac{V_0}{2}\right] u_{nq} = E_{nq}u_{nq} \tag{2.41}$$

The offset $-\frac{V_0}{2}$ can be neglected and absorbed into the energy. This has the form of the Mathieu equation. Because $u_{nq}(x)$ has a spatial periodicity of a, We can express u_{nq} in the Fourier basis with a discrete Fourier series:

$$u_{nq}(x) = \sum_{j=-\infty}^{\infty} c_j^{nq} e^{i2jk_L x} \tag{2.42}$$

Similarly, the potential $V(x)$ can also be expressed as:

$$\begin{aligned} V(x) &= -\frac{V_0}{2}\cos(2k_L x) \\ &= -\frac{V_0}{4}e^{i2k_L x} + e^{-i2k_L x} \end{aligned} \tag{2.43}$$

In order to solve for E_{nq} in Eqn. 2.41 with the Fourier expansion of u_{nq}, the sum must

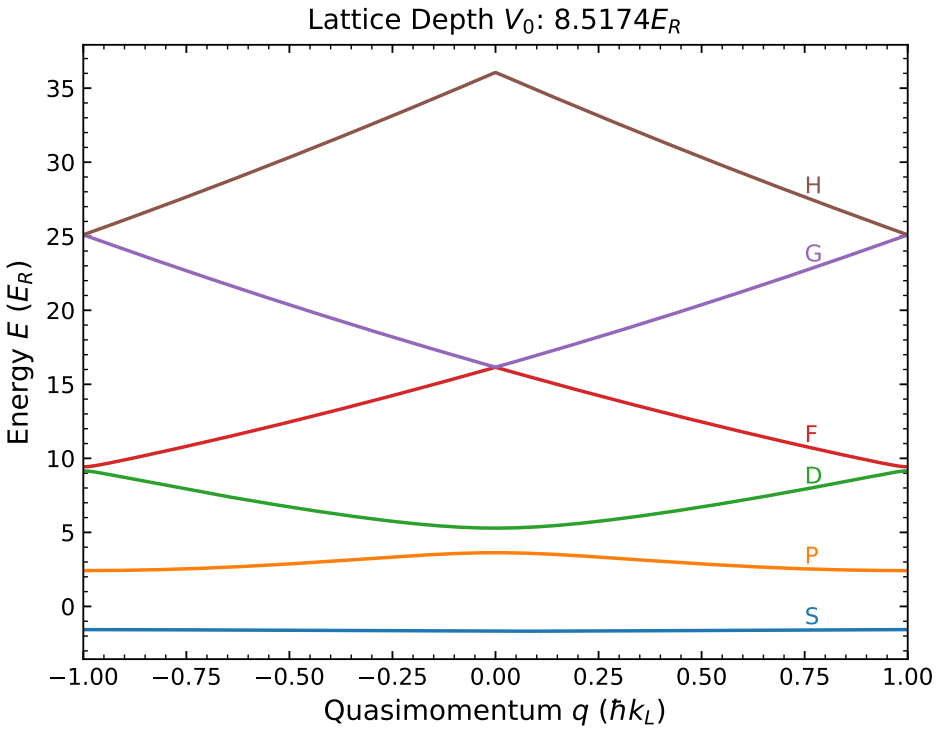

Figure 2.2: The one-dimensional optical lattice band structure with a lattice depth V_0 of 8.5174 E_R. Spectroscopic notation is used to denote each band.

be truncated to be symmetric and finite. Choosing the first $2l+1$ band indices for j, we have $u_{nq}(x) = \sum_{j=-l}^{l} c_j^{nq} e^{i2jk_L x}$. Substituting the expansions of u_{nq} and V into Eqn. 2.41, the equation becomes:

$$\left[\left(2j + \frac{q}{\hbar k_L}\right)^2\right] \frac{\hbar^2 k_L^2}{2m}\, c_j^{nq} - \frac{V_0}{4}\left(c_{j-1}^{nq} + c_{j+1}^{nq}\right) = E_{nq} c_j^{nq} \tag{2.44}$$

where $-l \leq j \leq l$. This is an eigenvalue equation for a $(2l+1) \times (2l+1)$ real symmetric tri-diagonal matrix, also known as the Bloch Hamiltonian matrix. Solving this for a specific quasimomentum q would give us the energies of the first $(2l+1)$ bands at this specific quasimomentum.

Because the Hamiltonian has a discrete translation symmetry in position space with a periodicity of a, it also has such symmetry in the momentum space with a periodicity of $2k_L = \frac{2\pi}{a}$. We define the 1st *Brillouin* zone for all the quasimomenta $q \in [-\hbar k_L,\ \hbar k_L]$, as any quasimomentum outside of this interval would yield repetitive information because of the momentum periodicity of $2\hbar k_L$. The eigenspectra to Eqn. 2.44 within the first *Brillouin* zone is shown in Fig. 2.2 at a lattice depth V_0 of 8.5174 E_R. The first sixth bands are plotted and labeled with the corresponding capitalized spectroscopic orbital letters. For example, the first / ground band is also called the S band.

2.2.3 Bloch Oscillation

When a spatially uniform force $\mathcal{F}(t)$ is applied to the optical lattice Hamiltonian in Eqn. 2.38, we have:

$$H = \frac{p^2}{2m} - V_0 \cos^2(k_L x) - \mathcal{F}(t)x \tag{2.45}$$

which seems to break the discrete spatial translation symmetry for the lattice. However, one can transform the Hamiltonian and the wavefunctions of the system with the gauge transformation U_G [18]:

$$U_G = e^{i\frac{x}{\hbar}\int_0^t \mathcal{F}(t')dt'} \tag{2.46}$$

The general unitary transformation to a Hamiltonian H and its wavefunction ψ is given by:

$$H \rightarrow UHU^{\dagger} + i\hbar \left(\frac{\partial U}{\partial t}\right) U^{\dagger} \tag{2.47}$$

$$\psi \rightarrow U\psi \tag{2.48}$$

The transformed Hamiltonian becomes:

$$H = \frac{\left[p + \int_0^t \mathcal{F}(t')dt'\right]^2}{2m} - V_0 \cos^2(k_L x) \tag{2.49}$$

which now proves to preserve the spatial translation symmetry of the system. We can apply Bloch's theorem again to find the solutions to the transformed Hamiltonian in terms of the Bloch functions $u(x,\ t)$. If the initial wavefunction is of the form

$$\psi(x,\ t=0) = e^{i\frac{q_0}{\hbar}x} u(x,\ 0) \tag{2.50}$$

after an evolution time t, the wavefunction maintains the same Bloch form with:

$$\psi(x,\ t) = e^{i\frac{q(t)}{\hbar}x} u(x,\ t) \tag{2.51}$$

where

$$q(t) = q_0 + \int_0^t \mathcal{F}(t')dt' \tag{2.52}$$

When the force is time independent, the quasimomentum simply evolves linearly with time:

$$q(t) = q_0 + \mathcal{F}t \tag{2.53}$$

More specifically, if the initial wavefunction is a Bloch state of the optical lattice Hamiltonian in Eqn. 2.38,

$$\psi(x,\ t=0) = \psi_{nq_0}(x) = e^{i\frac{q_0}{\hbar}x} u_{nq_0}(x) \tag{2.54}$$

and assuming the applied force is weak, the wavefunction at time t coincides with a new Bloch state at the final quasimomentum $q(t)$ with the same band index n:

$$\psi(x,\ t) = \psi_{nq(t)}(x) = e^{i\frac{q(t)}{\hbar}x} u_{nq(t)}(x) \tag{2.55}$$

up to a overall phase factor. The Bloch function $u_{nq(t)}(x)$ is an instantaneous eigenstate that satisfies the instantaneous eigenvalue equation

$$\left[\frac{(p+q_0+\mathcal{F}t)^2}{2m} - \frac{V_0}{2}\cos(2k_L x) - \frac{V_0}{2}\right] u_{nq(t)} = E_{nq(t)} u_{nq(t)} \tag{2.56}$$

This follows from the adiabatic approximation. Physically, it represents that the quasimomentum of the particle increases linearly with time under the influence of a perturbative force. Once it reaches the edge of the *Brillouin* zone ($q = \hbar k_L$), it "bounces" back to the other edge ($q = -\hbar k_L$) through Bragg scattering. One way to imagine it is that the atom is resonant with a two-photon transition at the zone edge, which transfers the atom momentum from $\hbar k_L$ to $-\hbar k_L$. Then, the atom traverses the *Brillouin* zone again and repeats the entire process. This repeat process is known as the Bloch oscillation, with a period of

$$T_B = \frac{2\hbar k_L}{\mathcal{F}} \tag{2.57}$$

If the initial wavefunction is not a single Bloch state, but a Gaussian wavepacket centered at a specific quasimomentum $q(t)$ with a finite but small width, we can write down the group velocity $v_g(t)$ of the wavepacket as:

$$v_g \equiv \frac{d\langle x\rangle}{dt} = \left.\frac{\partial E_{nq}}{\partial q}\right|_{q(t)} \tag{2.58}$$

where $\langle x\rangle$ denotes the expectation value of the wavepacket position. It means that Bloch oscillation doesn't occur only in momentum space, but also in real space. However, the amplitude of such oscillation is typically very small and hard to be detected in position space. In courtesy of the lithium's light mass, our group has previously observed Bloch oscillation in position space and successfully mapped out the lattice band structure [8].

The way to induce a constant force in our experiment is to use a magnetic field gradient, where $B(x) = Bx$. The weak-field Zeeman shift for ^{7}Li in $^2S_{1/2}$ is [7]:

$$\begin{aligned} E =& \mu_B g_J m_J B(x) \\ =& \mu_B g_J m_J B x \end{aligned} \tag{2.59}$$

where μ_B is the Bohr magneton and m is the magnetic quantum number. Here $J = S$ for ^{7}Li in $^2S_{1/2}$ since $L = 0$. The applied force along x can be found be taking the gradient of the energy:

$$F \equiv -\frac{\partial E}{\partial x} = -\mu_B g_J m_J B. \tag{2.60}$$

2.3 Floquet Theory

Floquet theory is used to describe physical systems that are periodic in time. In the quantum mechanics context, the Hamiltonian becomes temporally periodic for such systems, and there exists a well-established framework known as the Floquet formalism to describe them [19, 20, 21]. Utilization of time-periodic driving opens up an additional dimension of degrees of freedom, which allows us to flexibly engineer quantum systems. This method, Floquet engineering, in cold-atom platforms has given rise to realizations such as artificial gauge fields, topological insulators, and density-dependent tunneling [22, 23].

For a time-dependent Hamiltonian $H(t)$ invariant under the transformation $t \to t+T$, we have the following:

$$i\hbar\frac{\partial\psi(t)}{\partial t} = H(t)\psi(t) \tag{2.61}$$

$$H(t) = H(t+T) \tag{2.62}$$

The Floquet theorem, analogous to Bloch's theorem, states that the set of solutions $\{\psi_n(t)\}$ to Eqn. 2.61 is given by:

$$\psi_n(t) = e^{-i\frac{\epsilon_n}{\hbar}t}u_n(t) \tag{2.63}$$

where $\psi_n(t)$ is the quasi-stationary Floquet states, ϵ_n is the associated quasienergy, and $u_n(t)$ is the corresponding Floquet function where $u_n(t) = u_n(t+T)$. The general solution

is a linear combination of different Floquet states:

$$\begin{aligned}\psi(t) &= \sum_n a_n \psi_n(t) \\ &= \sum_n a_n e^{-i\frac{\epsilon_n}{\hbar}t} u_n(t)\end{aligned} \tag{2.64}$$

where a_n is time independent and can be found from the initial condition $\psi(0) = \sum_n a_n \psi_n(0)$.

An important operator in the Floquet formalism is the one-period, stroboscopic time evolution operator $U(T)$, where

$$U(T) \equiv U(t+T,\ t) \tag{2.65}$$

Setting $t = 0$, we can define a Hermitian operator H_{F}

$$H_{\mathrm{F}} = \frac{1}{T}\int_0^T H(t)dt \tag{2.66}$$

such that

$$\begin{aligned}U(T) &= e^{-i\frac{1}{\hbar}\int_0^T H(t)dt} \\ &= e^{-i\frac{H_{\mathrm{F}}}{\hbar}T}\end{aligned} \tag{2.67}$$

The operator H_F is known as the Floquet Hamiltonian, which is the time-average of the original Hamiltonian $H(t)$. Applying $U(T)$ to the Floquet states $\psi_n(t)$ gives:

$$U(T)\psi_n(t) = \psi_n(t+T) \tag{2.68}$$

$$U(T)e^{-i\frac{\epsilon_n}{\hbar}t}u_n(t) = e^{-i\frac{\epsilon_n}{\hbar}(t+T)}u_n(t+T) \tag{2.69}$$

$$U(T)u_n(t) = e^{-i\frac{\epsilon_n}{\hbar}T}u_n(t) \tag{2.70}$$

It follows that the sets of eigenvalues and eigenvectors of H_{F} are $\{\epsilon_n\}$ and $\{u_n(t)\}$. Because $U(T)$ is stroboscopic, the quasienergy is defined up to $\hbar\omega_D$, where $\omega_D = \frac{2\pi}{T}$ is the drive angular frequency,

$$e^{-i\frac{\epsilon_n + j\hbar\omega_D}{\hbar}T} = e^{-i\frac{\epsilon_n}{\hbar}T},\ j \in \mathbb{Z} \tag{2.71}$$

Then, we can defined the 1st quasienergy *Brillouin* zone to be $\epsilon_n \in [-\frac{\hbar\omega_D}{2},\ -\frac{\hbar\omega_D}{2}]$. The stroboscopic evolution operator $U(T)$ also has the following property:

$$U(nT) = U^n(T) \tag{2.72}$$

$$U(t' + nT,\ t) = U(t',\ t)U^n(T) \tag{2.73}$$

The Floquet theorem and its corresponding formalism will be used later in the thesis to construct Floquet-Bloch bands that are periodic in both momentum and energy.

Chapter 3

Electrical System

Chapter 3 describes most of my main electronic projects that have been integrated into the lithium machine in the Weld lab, including a magnetometer, eight radio-frequency (RF) drivers, magnetic gradient ("xvwings") current stabilization, Feshbach field (PTEN) current stabilization, and AC line trigger.

3.1 Magnetometer

Magnetic field is utilized in our experiment for a variety of purposes, such as BEc production as well as tuning the interaction strength, and force balancing. The complexity and sheer number of electromagnetic coils demand external monitoring, and even precise control, of the field dynamics during the experiment. The existing home-built three-dimensional magnetometer has been designed to have two operational modes: (1) a high bandwidth mode that records the magnetic field dynamics during the experiment at a sampling rate of 5-12 kHz, and (2) a background logging mode that measure the background magnetic field at a sampling rate of 1 Hz when the experiment is not being operated. Below I will provide some description about the setup and how to control the

magnetometer using Python and a LabJack U6 data acquisition system (DAQ).

3.1.1 Setup

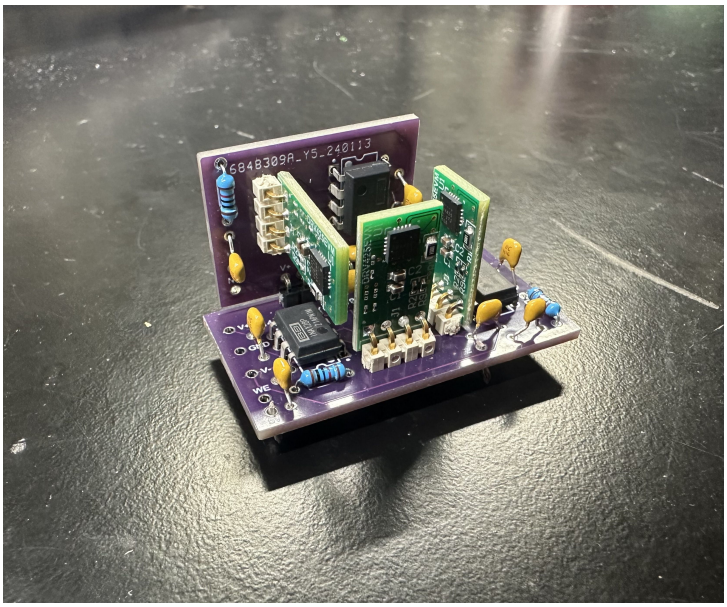

Figure 3.1: A duplicate of the three-dimensional magnetometer that has been installed into the lithium machine.

The three-dimensional magnetometer consists of three fluxgate magnetic sensors (Texas Instruments DRV425EVM) sitting on two orthogonal printed circuit boards (PCBs) connected by right angle header pins, as shown in Fig. 3.1. Each sensor module is responsible for a single axis, so that the we are able to measure the magnetic field along the vertical, Zeeman slower, and lattice directions. The sensor itself is a digital chip whose signals are converted to analog voltages by the evaluation module. The module then sends out an analog output with reference to half of the positive supply voltage, which in this case is 2.5 V (when the supply voltage is 5 V). The output signal and the reference signal are fed into an instrumentation amplifier (Texas Instruments INA128P) in order to produce a single-ended output. A passive RC low-pass filter at a corner frequency of about 5 kHz was added to the output of the instrumentation amplifier to suppress noise above the

Nyquist frequency of the setup. The conversion relationship between magnetic field and output voltage is: Magnetic Field (G) = $\frac{125}{61}\frac{\text{G}}{\text{V}} \times$ Ouput Voltage (V).

A LabJack U6 and a LJTick-DAC accessory component are used to power the magnetometer and save the three output voltages for data analysis. The LJTick-DAC provides a pair of 14-bit analog outputs with a range of $\pm$ 10 V for the instrumentation amplifier power rails. The LabJack U6 itself provides a 5 V power ("VS") for the three sensor evaluation modules. Each of the three output voltages from the modules are measured through the LabJack U6 AIN 0, AIN 1, and AIN 2 channels. All the power and signal connections between the PCBs and the LabJack U6 are done through a double shielded "data communication" cable from McMaster-Carr. The magnetometer and the LabJack U6 are housed in two separate aluminum boxes with extra aluminum foil covering the entirety of the boxes as well as the double shielded cables for preventing RF contamination. It was empirically discovered that any small gap left open from the foil could lead to damage of transmitted data.

The LabJack U6 is connected to the monitoring PC (Joe) via USB connection and can be controlled through Python with the package "LabJackPython". Different Python scripts are written for the high bandwidth mode ("Li_sequence.py" and "Li_sequence _plot.py") and the background logging mode ("Li_background.py" and "Li _background _plot.py"). All the script files are stored in the bananastand (B:_Li\Machine Code\Magnetometer) and can be accessed through PyCharm. In the subsections below, I will detail how to use each of the operation modes.

3.1.2 High Bandwidth Mode

For using the high bandwidth mode to measure the magnetic field throughout the whole sequence, open and run the script ("Li_sequence.py") in PyCharm. As shown

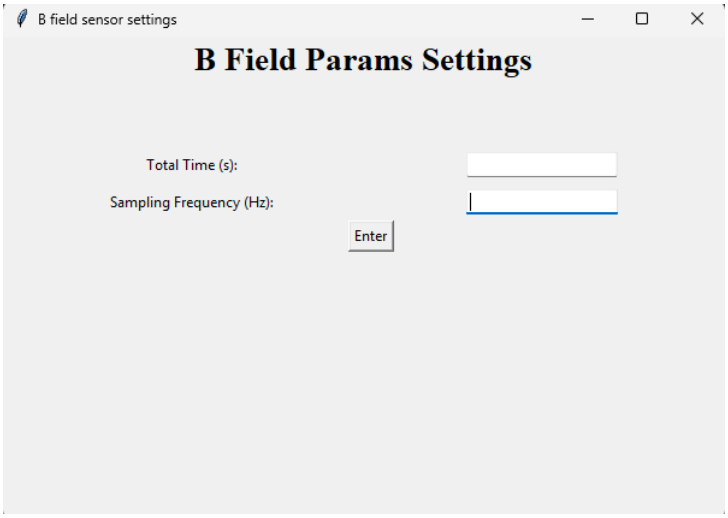

Figure 3.2: The prompt window for user input for the magnetometer in the high bandwidth mode.

in Fig. 3.2, a prompt window would pop up and ask for the total duration of the log and the sample frequency (typically 20+ sec and 10-12 kHz). After hitting "enter" in the prompt window, the script establishes connection to the LabJack U6 and powers on the magnetometer. Once a Cicero digital trigger is received by the LabJack U6, it would start measuring the three-dimensional magnetic field for the total input time at the sampling frequency requested. The data is then stored as a .csv file in the bananastand (B:_Li\Logging \Magnetic_field). The script automatically create a folder for each day (e.g. 2025_05_9) in the directory above if the high bandwidth mode is activated for that given day. Each file in the folder represents one run and is given a timestamp as the filename.

After the folder has been created for the day and at least one run is inside the folder, we can run the script ("Li_sequence _plot.py"). This would generate a graph window that shows the magnetic waveform along all three axes and automatically updates the plots after each run is completed. Fig. 3.3 shows an exampled waveform of the magnetic field during a standard lattice experimental sequence. The typical peak-to-peak noise for

the high bandwidth mode is normally greater than 5 mG.

The initial purpose of a magnetometer located within the enclosure was being able to

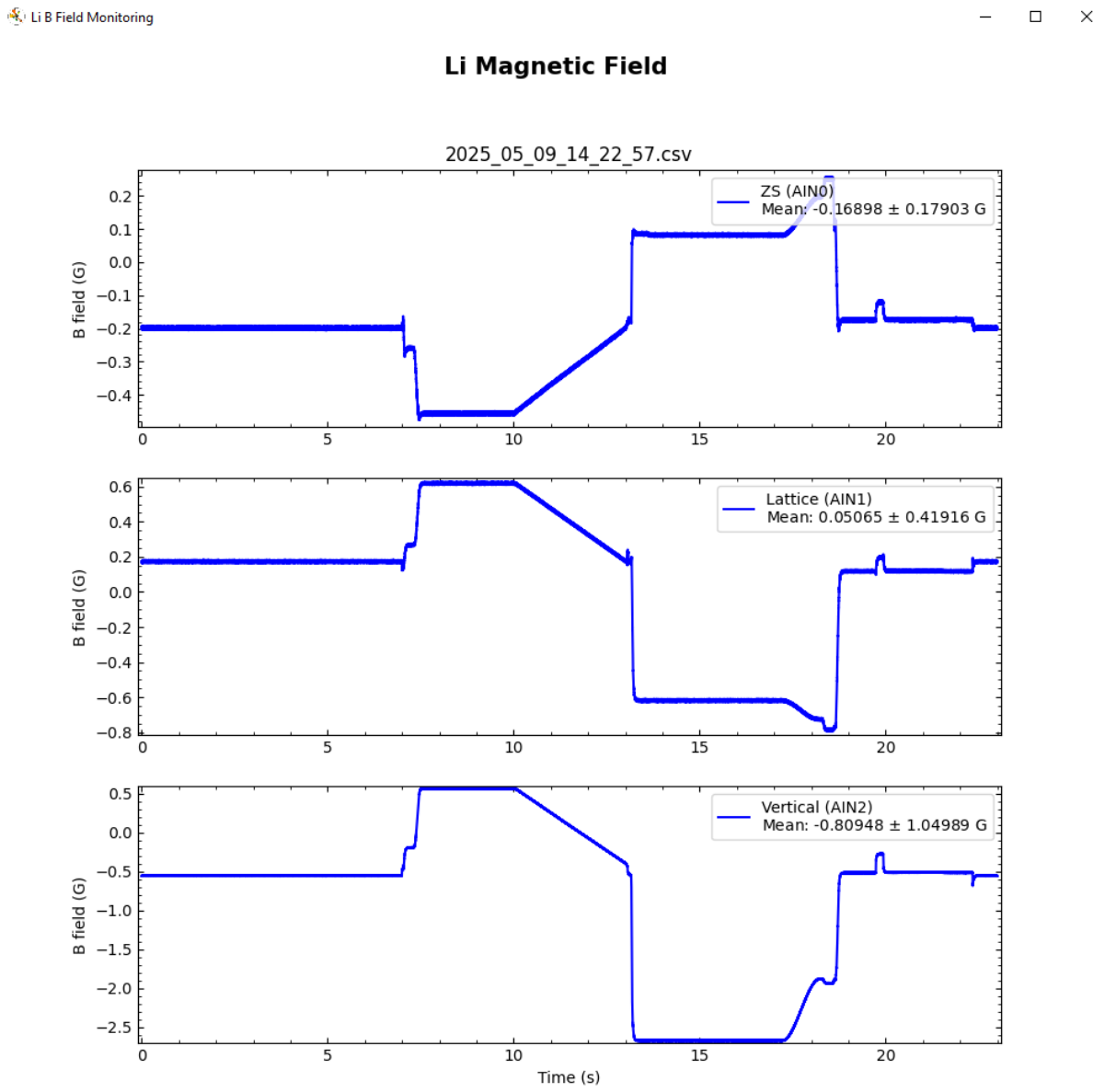

Figure 3.3: An example waveform for the Li sequence, taken on 5/9/2025.

precisely measure the magnetic field dynamics during the experimental sequence, as many stages of the experiment include simultaneous usage of multiple magnetic coils. However,

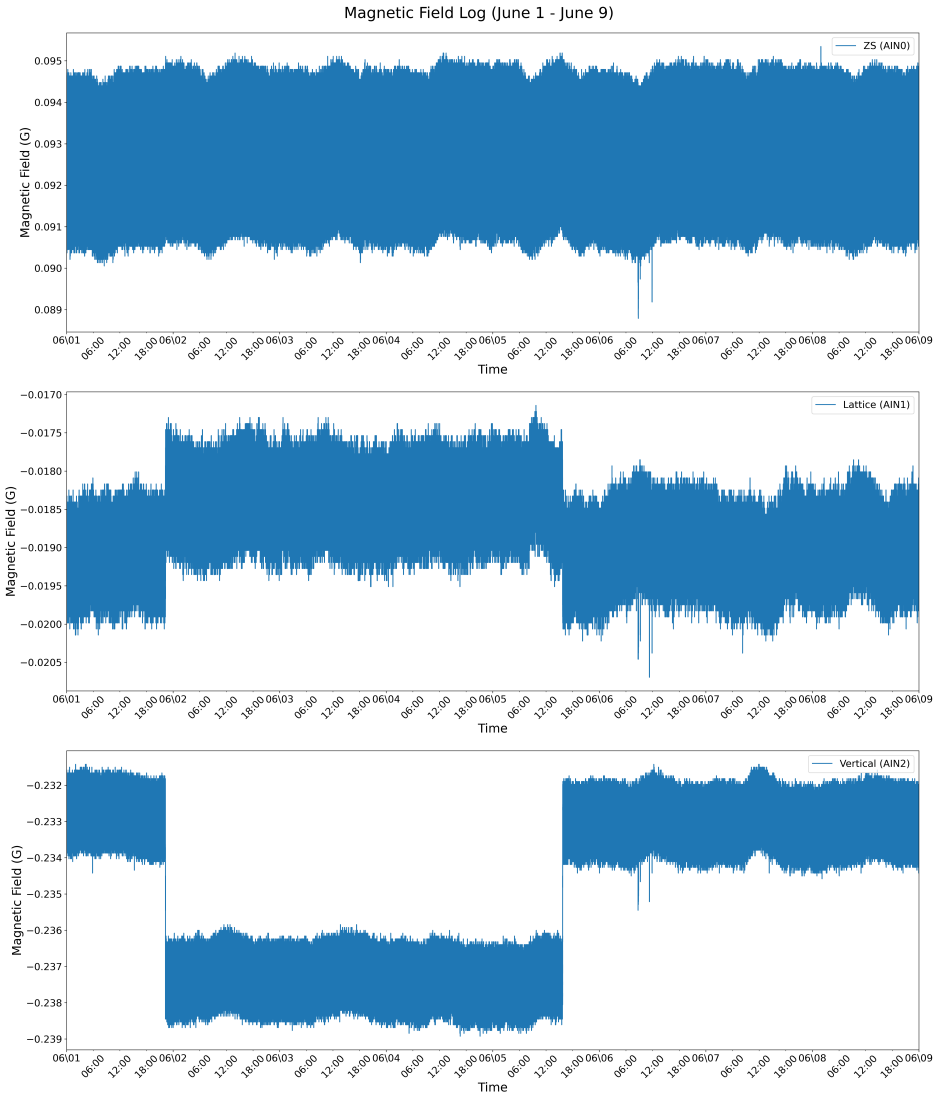

Figure 3.4: An example waveform for the Li background logging, taken from 6/1/2024 to 6/9/2024.

it has proven challenging due to large vacuum chamber, high bandwidth requirement, and constrained space limited by the amount of optics in the surroundings. Despite having a large bias field at the location of the atoms in certain experimental stages (e.g. optical evaporation and non-interacting BEC), a magnetic dipole field's strength decays as $\frac{1}{r^3}$, so the magnetic field is reduced by approximately two orders of magnitude by the time it reaches the magnetometer ($O(G)$). This significantly limits the level of precision

we can achieve as well as faithfully reversely tracking the magnetic field dynamics at the location of the atoms.

3.1.3 Background Logging Mode

The background logging mode is intended to be used when the machine is not running, or when we are interested in variation of background magnetic field caused by anything other than the experiment itself. For using this mode, open and run the script ("Li_background.py") in PyCharm. The script would automatically connect to the LabJack U6 and begin logging the background magnetic field at a rate of 1 Hz. The data for each day is stored as a .csv file in the bananastand (B:_Li\Logging \Magnetic_field _background) with a folder being created for each month. Fig. 3.4 shows a consecutive logging of more than one week from 6/1/24 to 6/9/24, when we observed a significant shift in our background magnetic field ($\sim$ 5 mG) due to large magnetic activity ongoing in a nearby lab. The typical noise in the background logging mode measurement is 5 mG.

3.2 Radio-Frequency Driver

A radio-frequency (RF) driver produces/received an input RF signal and outputs an amplified signal, typically at $O(W)$ level for atomic physics experiment. It normally also contains the capabilities to switch on/off the RF in sub-microsecond scale and change the gain of amplification for the RF signal in an continuous way. The amplified RF signal can be used for controlling an acousto-optic modulator/deflector (AOM/AOD) or for an antenna to perform hyperfine state manipulation. Fig. 3.5 illustrates the schematics of a common one-channel configuration. Most RF driver box/chassis in the lithium experiment contains four such channels for reducing the usage of shared electrical

components and for efficient space utilization. Below I will breakdown the schematics into two separate discussions of RF components and electrical connections.

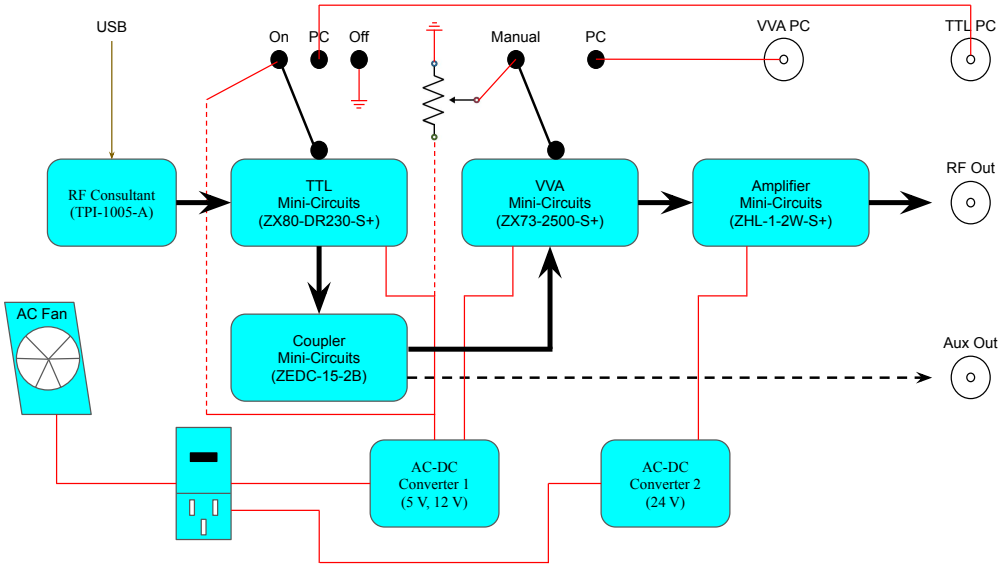

Figure 3.5: The schematics for one channel of RF components and analog voltage connections in a RF driver box.

3.2.1 RF Components

The RF signal is synthesized and generated digitally through a signal generator (RF-Consultant TPI-1005-A). The RF parameters can be remotely varied via USB connection between the RF Consultant and the PC using the TPI-Link software, which could be downloaded in the RF-Consultant website. This has been shown to be an excellent and reliable RF source for a single, constant frequency. However, certain applications with RF-Consultant might not be ideal with regard to a time-varying RF signal, such as RF sweep and RF frequency modulation. It was found that for the RF-Consultant to change its RF frequency (i.e. time-varying the RF frequency), it would turn off the output very briefly and update the frequency before turning the signal back on. This was confirmed

with the company that the new frequency must be locked during the reset process before the output is enabled, which takes about $O(10^{-4})$ to $O(10^{-3})$ s. This is incompatible with certain scenarios in our experiment when we attempted to use it for frequency modulating the saturated-absorption spectroscopy AOM, and for frequency sweeping the MOTC AOM during the compressed magnetio-optical trap stage, where the relevant timescales are comparable to the reset time. In this case, a voltage-controlled oscillator or a function generator could be more advantageous to produce the time-varying RF source.

Once the RF source is generated, we use coaxial cables with SMA or BNC connections to transmit the RF between components. It is important to note that for microwave transmission with frequency > 1 GHz, cable loss from normal SMA cables can become significant, and special cables with appropriate frequency ratings should be used instead. A transistor-transistor logic (TTL) solid state switch (Mini-Circuits ZX80-DR230-S+) is connected to the output of the RF-Consultant to switch on/off the RF in sub-microseconds upon a TTL signal. The TTL passes the RF signal to a coupler (Mini-Circuits ZEDC-15-2B) that splits a very small fraction of the RF signal to the auxiliary output port so that we are able to monitor the RF frequency without disconnecting the main RF output or disturbing any normal RF operation. The majority of the RF power goes into a voltage variable attenuator (VVA) (Mini-Circuits ZX73-2500-S+), where an applied analog voltage can control the amount of output RF power in an non-linear way. Before sending the main RF signal through the BNC output port, we amplify the RF signal with an amplifier (Mini-Circuits ZHL-1-2W-S+), which is able to deliver a maximum of 2 W RF power after the amplification process. The amount of RF power output from the driver box depends on the specific application. For driving AOMs, a 2 W amplifier is often used even if it slightly exceeds the maximum input RF ratings. We can always reduce the output power through the VVA, whereas a 1 W amplifier might not fully saturate the AOM and it could lead to low AOM output efficiency. For driving

antennas, the power requirements tend to be higher, and can go up to 5 W or 10 W.

3.2.2 Electrical Connections

Since the RF driver box controls the RF in various ways including amplification, many components used are active and thus requires certain power being supplied. Most, if not all, RF drivers have a AC power entry module (e.g. TE Corcom PE0S0DSXB) that draws 120 V, 60 Hz AC power from a nearby outlet for most power consumption within the box. The AC ground should always be connected to the box's metallic wall for safety purposes. The AC power is directly supplied to the fans mounted on the sides of the box. The fans are used to perform air cooling and remove residual heat generated by components like the amplifier with a large heat sink on the top. It is intentional to choose AC-powered fans instead of DC-powered fans so that we do not introduce noise from the fans' mechanical motions to any DC voltages related to the RF signals.

The AC power is also supplied to one or two switching/linear AC-DC converters. They convert the AC voltages to specific constant DC voltages that meet the supply voltage requirement of the RF components. Commonly used voltages are: 5 V, 12 V, 18 V, and 24 V. For precise applications, where RF frequency and power noises are important for the experiment, a linear AC-DC converter is preferred over a switching AC-DC converter due to differences in conversion mechanism, and thus noise performance. However, linear AC-DC converters tend to be larger in size and more expensive. It is also often good practices to use voltage regulators for constant DC voltages if the current draw is not too large, as well as to add $\sim$1 μF capacitors between the power rails and ground.

The DC voltages are routed directly to the active components inside the box for supplying the necessary power. In addition, sometimes we want manual controls over the TTL and the VVA, so it is convenient to utilize the DC voltages inside the box for those

purposes as well. The TTL often operates in one of the three modes: manual on, manual off, and PC control, where the desired mode can be chosen through a three-way toggle switch located at the front panel of the box. A constant 5 V DC and a GND signal are connected to the manual on and manual off sides, respectively. In the PC mode, the TTL is directly linked to a TTL PC BNC port that connects to the PC with a BNC cable. Similarly, we want two control modes for the VVA chosen through a two-way toggle switch: manual and PC. In the manual mode, we use a potentiometer with a physical knob at the front panel to control the voltage delivered from the AC-DC Converter to the VVA. In the PC mode, an analog voltage is directly sent from the PC to the front panel VVA PC BNC port that is internally connected to the PC side of the toggle switch. Using the PC mode for TTL and VVA allows us to switch on/off RF and change output power in real-time, which often translates through an AOM/AOD to turning on/off laser beams and changing optical power in real-time during the experiment. LEDs are also installed at the front panel of the driver box to indicate the specific mode of operation. For example, a green LED with the LED on/off could be equivalent to whether the RF output is switched on or off. Using a two-color LED also allows us to assign each color to represent the VVA being in one of the two modes.

3.3 Magnetic Field Stabilization

Magnetic field is an important ingredient for modern atomic physics experiments, ranging from cooling and trapping of atoms (e.g. magneto-optical traps and magnetic quadrupole traps) [7], to controlling the interatomic interactions with Feshbach resonances [13]. The latter application of magnetically-tuned Feshbach resonances requires extra precision in magnetic field control for the studies of, for example, BEC-BCS Crossover, magnetoassociation of ultracold molecules, and interaction effect on quantum

many-body physics [13]. For this reason, many AMO groups have implemented various feedback and feedforward schemes to stabilize their magnetic field. A few of them have been listed here for completeness [24, 25, 26, 27], with more theses stored in the Weld lab wiki page for magnetic field stabilization. Many of them have provided useful information for the design of the magnetic field stabilization scheme in the lithium experiment.

Some common noise sources for electrically-generated magnetic field are:

- Current noise from the power supplies: $O(10^0)$ to $O(10^2)$ mG
- Ambient magnetic field noise:
  - Nearby experiments with Tesla-level magnetic fields: $O(10^0)$ mG
  - Elevators: $O(10^0)$ mG
  - 60 Hz harmonics from mains electricity: $O(10^0)$ to $O(10^1)$ mG
- Thermal fluctuations of the coils: $\leq O(10^0)$ mG (depends on the temperature stability)

The dominant contributions are the current noise from the supplies and the 60 Hz harmonics' fluctuations from the power line, leading to a stability of 10^4 signal-to-noise ratio (SNR). Therefore, the most sought attempts in field noise suppression are implementing current feedback and 60 Hz mains feedforward.

In the following subsections, I will outline the stabilization setup, performance, and future improvements for two sets of coils in our experiment, namely the lattice gradient (xvwings) and the Feshbach field (PTEN).

3.3.1 Lattice Gradient

For the trapped atom interferometry experiment with Floquet-Bloch bands, the interference fringes are obtained by scanning the applied force strength along the lattice

direction. The interferometer hence serves as a precise force sensor, which demands the force to be either inherently natural or precisely controlled if artificial. In order to achieve this, we utilized a set of coils (xvwings) constructed in the early days of the experiment to provide a magnetic gradient along the optical lattice direction. More specifically, it was used to cancel the residual force applied to the atoms from the main Feshbach coils during the high-field (HF) BEC and non-interacting (NI) BEC stages. Once the atoms are loaded into the optical lattice, we ramp down the xvwings gradient to a certain setpoint, such that it is no longer force canceled along the lattice direction and the force is mostly from the main Feshbach coils. However, since the total gradient is a sum of the xvwings and the Feshbach (PTEN and TDK) coils, any large fluctuations in xvwings current can be also translated to instability in force, which may be detrimental to the interferometry read-out signal and its contrast.

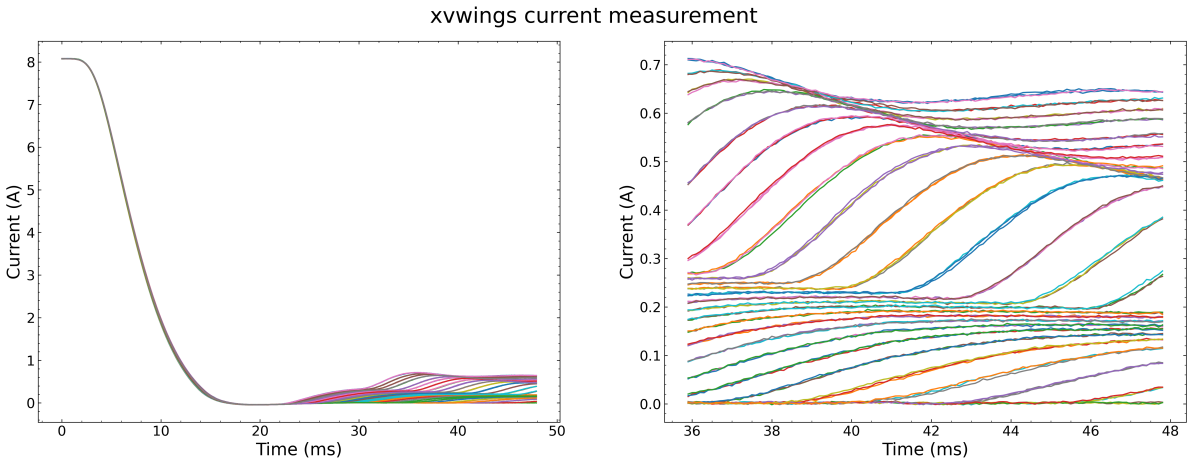

Figure 3.6: The current measurements of the xvwings coils for different final setpoints when ramping down to initialize Bloch oscillations of different periods.

It was experimentally observed through current measurements that the xvwings current contained large oscillations when ramping down during the beginning of the interferometry experiment. As we can see in Fig. 3.6, instead of a smooth ramp from an initial setpoint to a final setpoint, the currents for different final setpoints converge first and

then undergo significant ringings. This partially accounted for the early failed attempts in retrieving an interference signal, and a feedback system would allow the current to properly follow the waveform.

3.3.1.1 Setup

The PID setup is illustrated in Fig. 3.7, and it is designed to be continuously operating for all the experimental stages when the xvwings coils are active, i.e. from HF BEC to NI BEC to lattice experiment.

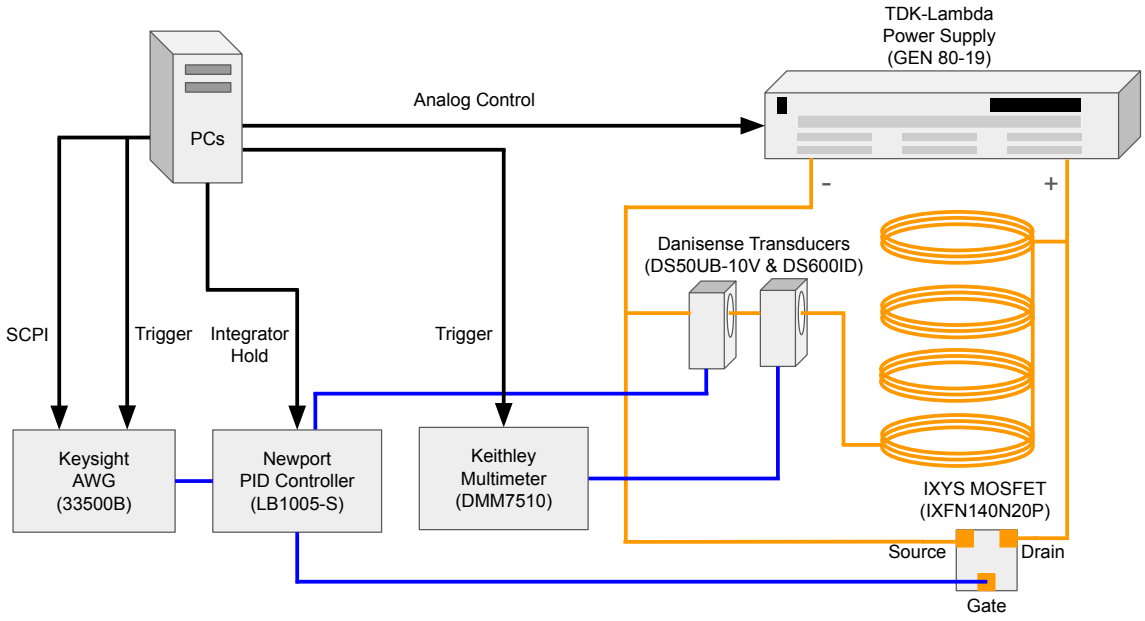

Figure 3.7: The PID schematics for lattice gradient stabilization.

The lithium machine uses the Cicero Word Generator [28] as the experiment's control software. It outputs a sequence of analog voltage ramps to the power supply (TDK-Lambda Gen 80-19) in real time, so that the current output can be remotely controlled through Cicero. The output current is directly proportional to the Cicero voltage. The current flowing through the xvwings coils are measured with two Danisense transducers

(DS50UB-10V and DS600ID), both of which are powered through the Danisense system interface unit (DSSIU-6-1U-V). The coil cables are routed three times through each transducer to enhance sensitivity at the cost of reducing measurement range.

The transducer DS50UB-10V has a < 1.55 ppm rms noise up to 10 kHz. It converts the measured current to an analog voltage that goes to an analog PID controller (Newport LB1005-S), with a voltage to current relationship of $\frac{5}{3}\frac{A}{V}$. The xvwings current setpoint going into the PID controller is produced from a Keysight waveform generator (33500B) that has a output voltage range of 10 V_{pp} and a resolution of 16 bits. In between each experimental run, a new arbitrary waveform is uploaded to the Keysight using SCPI commands. The specific waveform and its parameters are pre-determined using the Hardware Control Panel in Muscle Museum [29]. Each ramp for the xvwings contains an initial setpoint for the previous stage and a final setpoint for the next stage. To initialize a ramp, we send out a digital trigger from Cicero to the Keysight. The Keysight would then output the requested waveform to the PID controller. Once the ramp is completed, the Keysight maintains a constant output at the final value of the ramp, i.e. the xvwings setpoint for the next stage, until it receives the next trigger. Once all the waveforms have been generated, an additional trigger to the Keysight would reset the voltage output to 0 V. Based on the error signal (the difference between the measurement and the setpoint), the PID controller then outputs a voltage signal to the gate of a MOSFET (IXYS IXFN140N20P) in parallel with the xvwings coils. From the optimized gain, corner frequency, and possibly the low-frequency-gain-limit (LFGL) if LFGL is enabled, this PID output controls the amount of current being shunted away through the MOSFET, which would allow the current flowing through the coils to reach the setpoint.

A second transducer DS600ID is used to monitor the current and the PID performance. This helps with preventing ground loops and avoid introducing connections from

extra components to the feedback system. The transducer DS600ID also has a direct, scaled down current output, with a secondary-to-primary (output-to-input) relationship of 1500 $\frac{A}{A}$. Without the extra step in voltage conversion, it has a even better accuracy and noise performance ($<$ 0.1 ppm rms noise up to 10 kHz). This allows for better measurement and noise characterization of the xvwings PID. The output current from the DS600ID is measured by a Keithley 7-1/2 digit digital multimeter (DMM7510). The multimeter is controlled remotely through the Keithley Kickstart software, with the data being automatically saved to a designated directory per measurement. With the external trigger mode selected and the start button clicked, the DMM7510 would start the measurement upon receiving a digital trigger from Cicero.

Like mentioned above, the PID system is intended to be enabled whenever the xvwings is active. As of when this chapter is written, the xvwings is used in the experiment to cancel the main coils' gradient during the HF and NI stages. For any experiments relevant to Bloch oscillations, the xvwings current is ramped down to introduce a force from the main coils. Most of the PID optimization should be centered on this stage, since it is likely the stage at which science happens and ringings in Fig. 3.6 should be avoided. For the remaining stages of the sequence, the integrator hold feature of the PID controller is enabled through a external digital signal from Cicero. The measured current and the Keysight setpoint would also be zero.

Force canceled calibration is usually done first by doing time-of-flight (TOF) measurements with the atoms, meaning to turn off all trapping potentials simultaneously and allow the atoms to experience free expansion. We can record how their position along the lattice axis changes as a function of expansion/TOF time. once an optimal setpoint is chosen, the atoms' position should be mostly unchanged regardless of the expansion time. This method should be applicable to both HF and NI BEC. If there is a finite harmonic confinement present due to experimental perfection, we can utilize

this to detect residual force by scanning the hold time during which the atoms are in the optical trap. If there is a residual force present and if the optical trap is chosen to be weak enough, the atoms would undergo harmonic oscillations around the harmonic trap center. An appropriate chosen xvwings setpoint would largely, if not entirely, suppress such harmonic oscillations.

3.3.1.2 PID Optimization

Here I will discuss the procedure I had followed historically to optimize the PID performance. Since there exist multiple xvwings setpoint values for different stages of the experiment, the PID needs to ensure (i) the ramps connecting different xvwings force setpoints are smooth and properly following the correct ramp shapes, and (ii) the noise (any AC fluctuations) should be largely suppressed once reaching the constant xvwings force setpoints. It has proven to be challenging to optimize for both with an analog PID controller and only one set of PID parameters without gain scheduling. In the case of xvwigns PID, we have been prioritizing the first requirement to avoid large and rapid changes in the force environment for our BEC.

When tuning the PID parameters, one should first decide on the corner frequency, the frequency below which there is a roll off in gain and above which the gain is set by the proportional gain P. Turning up the corner frequency can increase the PID bandwidth while introducing higher frequency noise for the stages with a constant DC force setpoints. Therefore, the chosen corner frequency should be sufficiently high to let current ramps properly follow the desired shapes. The minimum corner frequency at which this occurs should be used to minimize noise contributions from high frequency components;; this was found empirically to be around 100 Hz. Once the corner frequency is determined, one should focus on the DC region in which the xvwings setpoint is a constant offset. The appropriate gain can be found by minimizing the rms noise around that offset. The

step size in scanning the gain knob is about 0.5 dB for each run. The LFGL feature is optional for xvwings PID, but one can always enable it and repeat the above process for each value of LFGL to hunt for the best PID parameters. It is also important that the amount of current shunted away should be roughly constant during the entire sequence, and the PID doesn't need to react to a sudden change in error signal. This is can be adjusted by changing the total current supplied to the system through Cicero xvwings setpoint.

3.3.1.3 Performance

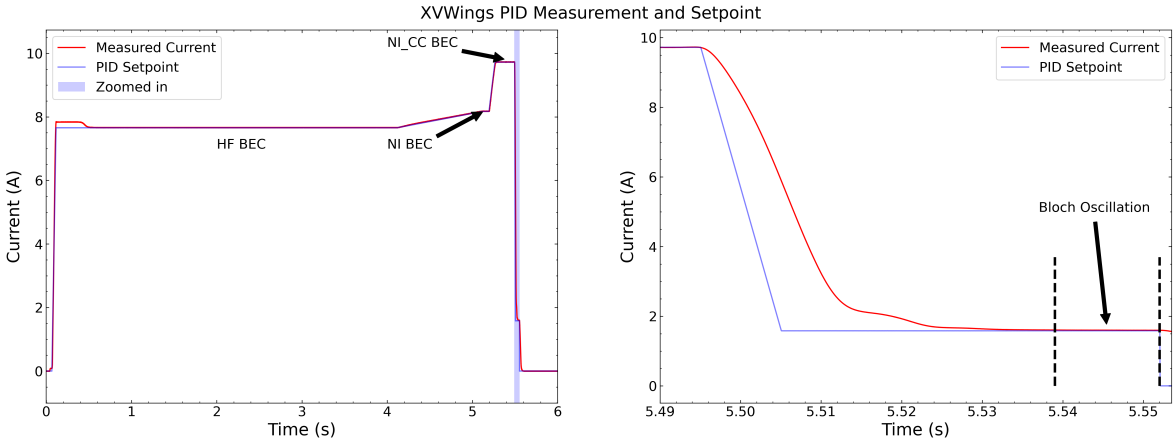

Figure 3.8: XVWings PID waveforms for the measurement and setpoint, recorded on 5/19/25.

Fig. 3.8 shows the full xvwings sequence when the PID is enabled. The measured current mostly follows the setpoint except for the fast rampings of a large amount of current at the beginning and at the end of the sequence. There are four major DC offset values for xvwings: HF BEC, NI BEC, NI_CC BEC, and Bloch oscillations. The first three are for force cancellation along the lattice axis for different bias field strengths (high field, non-interacting, non-interacting curvature cancellation). The last one is used to induce bloch oscillation as discussed earlier in the section. From Fig. 3.8, we can

see that it takes about 30 ms to fully ramp down the current due to the limit in PID bandwidth. This is the major drawback of the existing PID and potential upgrades are discussed in Section. 3.3.1.4.

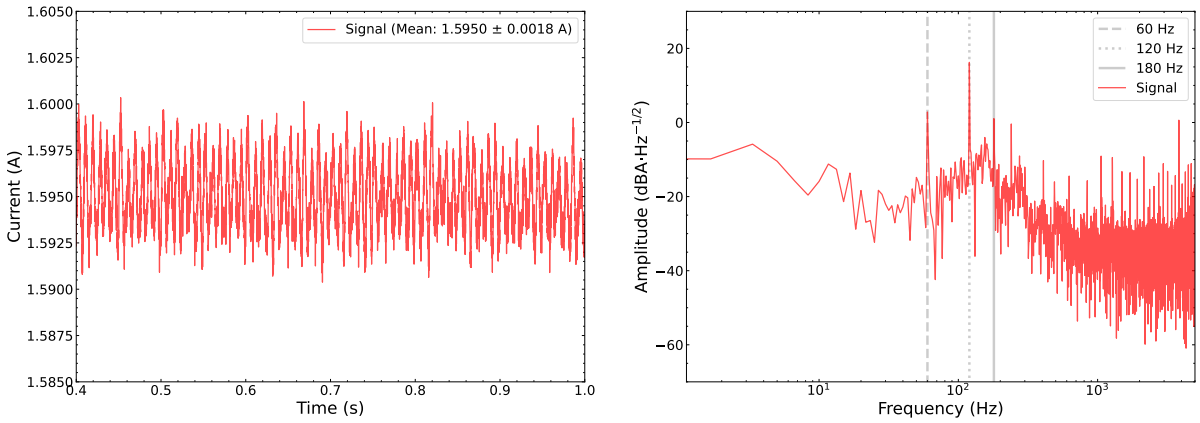

Figure 3.9: XVWings PID waveform for the measurement in the Bloch oscillation setpoint, recorded on 5/19/25. The measurement duration is intentionally increased so that the signal is not Fourier limited.

Fig. 3.9 characterizes the noise performance when the xvwings current is set to the Bloch oscillation stage. It is showing the steady-state behavior after the ramping has occurred. The measurement duration is intentionally increased by a large amount compared to the actual Bloch oscillation time so that the Fourier transform is not Fourier limited due to the small time window for the actual Bloch oscillation. From the Fourier spectrum in Fig. 3.9, we can see that the dominant noise source is the 60 Hz harmonics. These noises from the power line can be suppressed by PID feedback to a certain extent, but it is better to be addressed specifically using feedforward methods.

The noise-to-signal ratio for the xvwings current is about 0.11% from the measured standard deviation and the mean values. However, the actual gradient fluctuations during an experiment should be much smaller for two reasons. (i) The dominant noise frequencies are 60 Hz and 120 Hz, corresponding to a period of 16.7 and 8.3 ms. The Bloch oscillation time for our interferometry experiment is about 13 ms, which means the atoms do not

experience the full peak to peak fluctuations for certain frequencies. (ii) The gradient inducing the Bloch oscillation is mainly provided by the main coils, with xvwings partially counteracting the main coils gradient. Therefore, the noise-to-signal ratio for the xvwings gradient should be the ratio between the steady-state Bloch oscillation noise and the difference between the force canceled setpoint and the Bloch oscillation setpoint, which is 0.04% from the data in Fig. 3.8 and Fig. 3.9.

3.3.1.4 Future Improvements

As mentioned above, one set of PID parameters needs to make a compromise between high bandwidth and low noise. We saw that the dominant noise source once the xvwings reaches the setpoint is the 60 Hz harmonics, mostly 60 Hz and 120 Hz. One can imagine improving the current setup by targeting these harmonics with various feedforward methods or introducing a second PID feedback loop so that one loop is responsible for the smooth ramping behavior while the other is suppressing the noise in the DC offset stages. The idea of having two PIDs is similar to that in laser diode controller with a fast and a slow feedback loops running concurrently. Four possible upgrades to the existing setup are:

1. 60 Hz harmonics feedforward

    (a) Add a MOSFET in parallel with the current configuration, the gate of which is connected to a waveform generator that outputs a superposition of 60 Hz harmonics with the correct phase offsets.

    (b) Add a new set of compensation coils to introduce a small gradient along the lattice direction. These coils are meant to provide an AC force that is a superposition of 60 Hz harmonics with the correct phase offsets to cancel the residual 60 Hz harmonics in the xvwings.

One way to implement this is to:

- receive a 60 Hz trigger signal that is in phase with the 60 Hz signal of an AC outlet adjacent to the one powering the xvwings current supply. The method to do so is also mentioned in Section. 3.4 and has been integrated into Cicero to run our experiments sometimes in sync with the line to check for systematics related to the 60 Hz harmonics.
- determine the number of 60 Hz harmonics components one wishes to include in the feedforward and find the correct phase offset between each of the component and the TTL signal generated from the 60 Hz.
- output the superposition of all the chosen frequency components with the right phases in reference to the 60 Hz trigger signal using the waveform generator.
- scan the output amplitude of each frequency component so that the Fourier transform of the measured signal shows noise suppression of those frequencies.
- output the waveform to the MOSFET or to the analog control for the current supply of the new compensation coils.

The relative phase offsets between different frequencies could be drifting over a certain time scale, so it would be ideal to have an automated calibration script to find the correct phases automatically.

2. improve PID feedback loop

   (a) Replace the analog PID controller with a digital PID controller and find multiple sets of PID parameters responsible for different parts of the xvwings sequence, a.k.a gain scheduling. In particular, one set could be used for the ramps and the other used for the DC offset to suppress noise.

(b) Add a second PID loop to the existing one only enabled during the DC offset stages to suppress any AC noise.

3.3.2 Feshbach Field

The main intention for the Feshbach field (PTEN) stabilization is to suppress fluctuations around a chosen interaction strength during the experiment. This could be particularly important for the non-interacting case when the fluctuations lead to oscillations between slightly attractive and slight repulsive contact interactions. It was also shown that the lattice gradient noise was mainly from PTEN current noise (without PID) and xvwings current noise (with PID). Therefore, in order to reduce the lattice gradient noise, one step is to implement high current stabilization for PTEN.

The challenge of high current stabilization in the existing lithium setup is that the current noise is already relatively small without PID. The signal-to-noise ratio is at low 10^4, which means most of the electronic components in the PID system should ideally have higher SNR than that.

3.3.2.1 Setup

The stabilization scheme is shown in Fig. 3.10. It has similar setup as the xvwings PID with a few modifications.

1. **Solid-state Relay** The MOSFET (IXYS IXFN140N20P) now is in series with a solid-state relay (Crydom D1D40K) that is rated for 40 A. The relay is meant to be turned on whenever the PID is enabled. It is used to compensate for the fact that the Newport PID controller only has an integrator hold and the entire PID system cannot be turn off with an external trigger. One should make sure that the PTEN relay and the PTEN integrator hold should always have the opposite

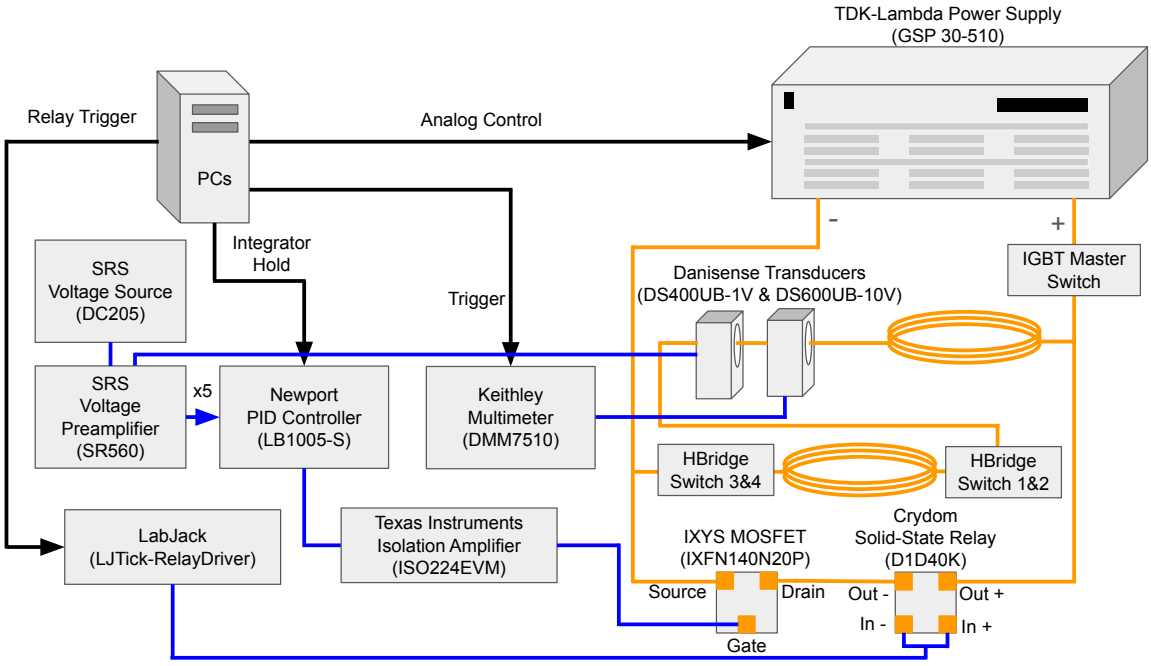

Figure 3.10: The high current stabilization scheme for the Feshbach (PTEN) coils.

logic, such that when the PID is enabled, the PTEN relay is high, and the PTEN integrator hold is low.

Because driving the relay requires 10 mA steady-state current, and Cicero digital trigger is not designed to source such a large amount of current, one needs to use a relay driver to in between to control the relay. The detailed layout for the driver module is shown in Fig. 3.11 (b). Here I used a LabJack driver (LJTick-RelayDriver) with the input side connected to a Cicero digital channel. The output forms a close loop with a floating power supply (Siglent SPD1168X) and the solid-state relay's input. The connection between RA and GNDR can be thought of as a switch that is controlled by the Cicero TTL signal. When the TTL is high, the switch is closed, and the relay input receives a voltage signal from the floating power supply. The Siglent power supply was a convenient choice at the time, and one can always find a more affordable alternative in the future (ideally remains

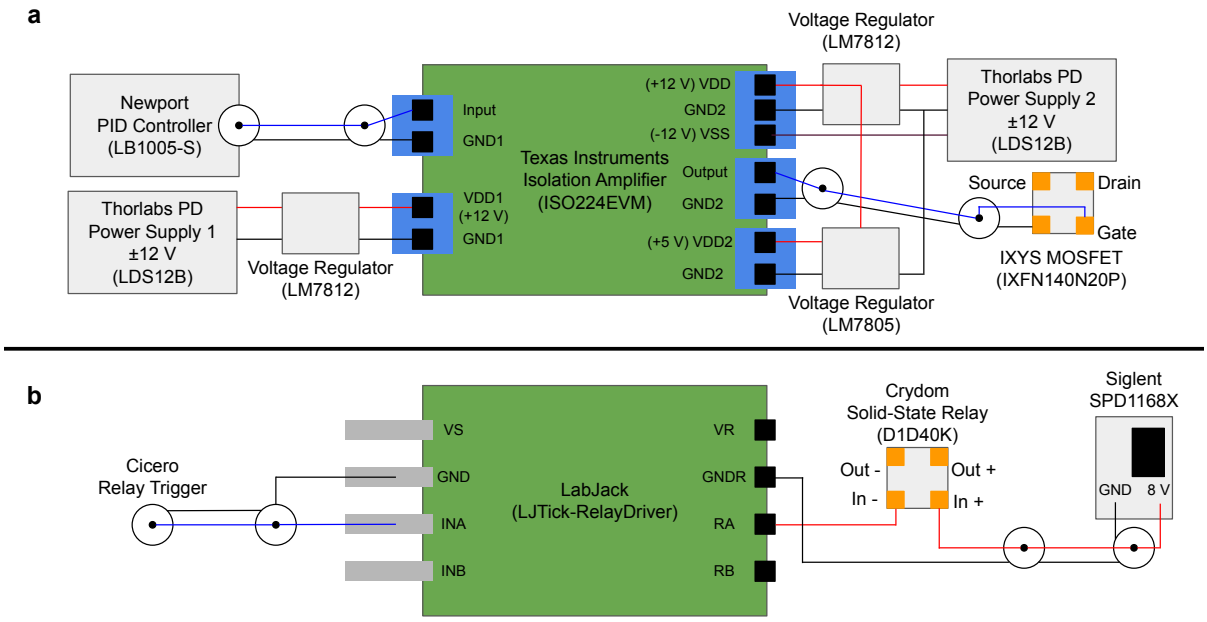

Figure 3.11: Detailed component designs used in the Feshbach (PTEN) current stabilization. (a) The isolation amplifier module layout. (b) The relay driver module layout.

floating).

2. **PID Input**

- **Current Transducers** The measurement current transducer is changed to a Danisense transducer (DS400UB-1V), suitable for the full range of PTEN current (0 - 510 A). It has a < 0.04 ppm rms noise up to 10 kHz. The voltage to current relationship is 400 $\frac{A}{V}$. The monitoring transducer is DS600UB-10V (60 $\frac{A}{V}$). It is important to route them through the coils outside of the HBridges, so that the current going through remains positive the entire time, or at least it should have the same sign as the setpoint when the PID is enabled.

- **Setpoint** The voltage setpoint is provided by a SRS precise voltage source

(DC205). It is able to provide a stable voltage signal of 6-digit resolution and of an accuracy of 7 ppm. The rms noise is less than 1 ppm.

- **Voltage Preamplifier** The voltage preamplifier (SRS SR560) is used to amplify the error signal, the difference of the transducer measurement and the setpoint, by five times, along with a 10 kHz low pass filter. Without using the amplifier, the error signal would mainly consists of a large DC offset compared to the rest of the AC components, which makes it difficult to suppress higher-frequency noise. Imposing a large AC gain to the signal helps the PID cancel both slow DC drifts and fast AC fluctuations simultaneously. Because the input range of the preamplifier is +3 V, we used a measurement transducer (DS400UB-1V) with a output range of 1 V.

3. **PID Controller** The amplifier output error signal from the voltage preamplifier goes to the signal input of the PID controller (Newport LB1005-S). Since the error subtraction has occurred in the preamplifier, the controller setpoint is default to zero.

   The output voltage of the Newport PID controller is capped at about 7 V to prevent damaging the MOSFET. If the PID were railed without the capped protection, it would output the maximum voltage at 10 V, which corresponds to tens of amps going through the MOSFET. The existing system is designed to shunt away less than 10 A for a few seconds. It was empirically tested that the MOSFET would break without active water cooling if the current flowing through is approximately above 15 A for more than ten seconds.

   Because the PID is disabled for most of the sequence, and the trigger timings do not overlap perfectly between the relay and the integrator hold, there could be charges building up across the analog integrator inside the PID controller for a finite

amount of time. This leads to an overshooting behavior the moment when the PID is enabled. To address this, the low-frequency-gain-limit (LFGL) feature of the controller must be in used. This would limit the controller's gain at low-frequency so that the built-up charges (DC level) do not affect the system significantly.

4. **PID Output & Isolation Amplifier** The PID output is connected to an isolation amplifier (Texas Instruments ISO224EVM) before going to the MOSFET. Due to "mysterious" high voltage spikes observed in our high current electronics, the isolation amplifier is meant to protect the PID controller from getting damaged. This incident has happened before, and the installation of the isolation amplifier was shown to mitigate the issue.

   Fig. 3.11 (a) shows the layout for the isolation amplifier circuit. The PID controller output goes into the input side of the isolation amplifier, which is powered by a ±12 V DC power supply (Thorlabs LDS12B) regulated by a voltage regulator (LM7812). Similarly, another ±12 V DC power supply (Thorlabs LDS12B) with the same voltage regulator (Thorlabs LDS12B) is used to power the output side. In addition, the +12 V is also regulated down to 5 V with a voltage regulator (LM7805) to supply an additional 5 V power rail. The output signal is connected to the gate and source of the MOSFET. One way to ensure that the isolation amplifier is properly functioning after inappropriate actions have been taken to the high current electronic system is to check with a multimeter whether the two grounds (GND 1 & GND 2) are connected or open. If they are connected, most likely the isolation amplifier has been damaged and must be replaced.

3.3.2.2 PID Optimization

As mentioned above, it is important to keep the PID in LFGL mode to prevent overshooting. According to the PID user mannual, the integrator is turned off for frequencies lower than than the 3-dB LFGL corner frequency: $f_{\mathrm{LFGL}} = f_{\mathrm{PI}} \times 10^{-g(dB)/20dB}$, where f_{PI} and g are the PI corner frequency in Hz and the low-frequency gain limit in dB, respectively. For example, a PI corner frequency f_{PI} of 100 Hz and a LFGL of 90 dB give a f_{LFGL} of 0.00316 Hz, below which the integrator is turned off. This significantly reduces the large gain introduced from timing mismatches and long-time integration of any finite error signal offset at the moment the PID is turned on, and therefore suppress overshooting behavior.

For optimizing the PID parameters, one should use the rms noise of the steady-state current as a metric. This can be done by triggering the Keithley DMM at the beginning of field ramp from HF to NI and digitally calculate the standard deviations of the signal after the current has reached a steady-state with PID. A full parameter space scan usually proceeds as the following:

1. Choose a PI corner frequency, usually start from the lowest one available (10 Hz).
2. Select a LFGL gain, usually start from the highest available. (90 dB)
3. Scan the proportional gain and measure the steady-state rms noise. Find the proportional gain at which the rms noise is the lowest. It is possible to see that as the proportional gain increases, ringings first occur and disappears with a sufficiently large gain.
4. Repeat steps 2 and 3 to find the parameters where the PID can be smoothly turned on without overshootings/oscillations while having the lowest rms noise possible at this PI corner frequency.

5. Repeat steps 1, 2, and 3 to find the lowest rms noise across different PI corner frequencies.

Sometimes the best PID parameters drift away over the course of days or weeks, and it is usually sufficient to slightly vary the proportional gain for recovering the performance.

3.3.2.3 Performance

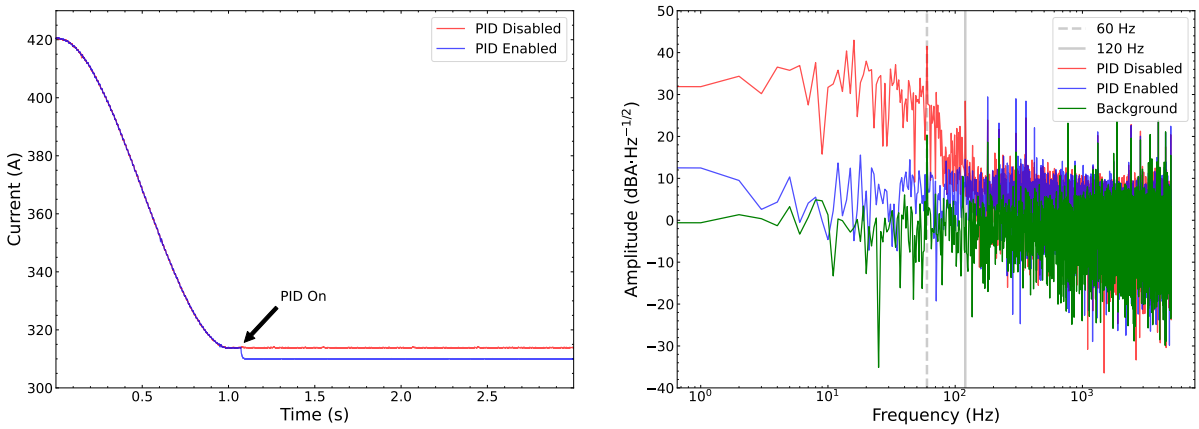

Figure 3.12: (a) Current measurements when the PID is disabled and enabled. (b) FFT of the steady-state current when the PID is disabled, enabled, and when the current supply is turned off. Data was taken on 5/26/25.

The PID turn on is annotated in Fig. 3.12 (a). We first use Cicero analog control to ramp down from HF current to a current slightly above NI, known as *FieldRamp*. Then we turn on the relay and turn off the integrator hold to activate the PID. The setpoint is controlled by the PID voltage setpoint from SRS DC205. The amount of current shunt away through the MOSFET is usually around 1 to 5 A. The PID performance in frequency domain is shown in Fig. 3.12 (b). All measurements were done with the Keithley DMM in digital voltage mode at 10 V full range and a sampling frequency of 10 kHz. We see that the PID lowers all AC components below ∼60 Hz by 20 dB, which corresponds to an order of magnitude reduction. The timescale of our experiment is on the order of millisecond, so ideally the current noise should be suppressed up to a few

kHz. However the measurement is mostly limited by the Keithley DMM noise floor at those frequencies, and one need to improve both the measurement techniques as well as the PID bandwidth.

3.3.2.4 Future Improvements

Possible ways to improve on the existing high current PID setup are to:

1. Replace the isolation amplifier. It is hypothesized that the isolation amplifier is the limitation of the current setup. The choice of the amplifier was purely out of convenience for the attempt in protecting the PID controller. It was measured by the potassium team (Jack) that the SNR of the ISO224EVM is $O(10^3)$, which is strictly lower than the SNR of the NI current without PID. One can attempt the AD210 isolation amplifier from Analog Devices, which has been discontinued but amply stored in our group.

2. Implement two PID loops (slow & fast). This effectively increases the stabilization bandwidth by having independent PIDs focusing on different sections of the spectrum. The fast loop PID can be AC coupled with a even larger amplification, e.g. 20, than the existing setup (G=5) on only the high frequency components.

3. Use a digital PID with high DAC and ADC resolutions. Both groups implementing ppm-level magnetic field stabilization utilize a digital PID with field-programmable-gate-arrays (FPGA) [24, 25]. It is my belief that this is the best approach for current PID, as it provides high flexibility in PID algorithms and gain scheduling, while having low noises in both input and output with suitable choices of digital-to-analog converter (DAC) and analog-to-digital-converted (ADC). Doing so allows for good feedback control on magnetic field over the entire experimental sequence. One could also attempt commercial digital PID, such as the quarto, but most

commercial options do not have sufficiently good DAC and ADC for this purpose. By using a commercial digital PID, one must be careful in circumventing the noise issue with a sufficiently large AC gain to amplify high-frequency noise.

3.4 AC Line Trigger

AC line trigger means that we sync the timing of an experiment or an input/output to the 60 Hz power line. This has the benefit for troubleshooting any 60 Hz harmonics related issues or providing a quick check on whether the experimental results are affected by the 60 Hz harmonics noise. As discussed above, it is also the first step in implementing 60 Hz harmonics feedforward method for magnetic field stabilization.

In order to do this, we utilize a Rigol digital oscilloscope (Rigol DS 1054Z). It is able to internally detect the power line phase and output a 60 Hz TTL signal that is in sync with the power line phase. We integrate this into the experiment by using the existing "hold and retrigger" comparator circuit. This circuit waits for the input voltage to reach a certain threshold before sending a signal to Cicero. The sequence in Cicero would not move on to the next column until it receives such a signal from "hold and retrigger", and thus all the stages after that would be initialized in reference to a constant 60 Hz phase, and it should remain consistent across all the experimental runs.

Chapter 4

Optical System

Chapter 4 describes two upgrades to our 1064 nm optics system, namely, a large aperture photodiode (5 mm diameter) module and a commercial laser pointing stabilization system from MRC Systems GmbH. I will detail the design and calibration of the photodiode as well as the integration of MRC pointing PID into the exisiting 1064 nm optical path, with alignment procedure suggestions based on the lessons the lithium team has learned.

4.1 Large Aperture Photodiode Module

The motivation behind a large aperture InGaAs photodiode module was our observation that the pointing instability of the sampled beam was the dominant noise source for our 1064 nm intensity stabilization, leading to fluctuations in our lattice depth. There exist many commercial large area silicon photodiode modules, but the frequency response of silicon photodiodes tend to be slow at 1064 nm due to its bandgap (1100 nm) being very close to this wavelength. The common material for 1064 nm photodiode is indium gallium arsenide (InGaAs) becuase of its fast response rate, but there do not exist many commercial large area InGaAs photodiode modules, so below I will present a home-made

version using a Hamamatsu InGaAs photodiode and a SRS current preamplifier. The

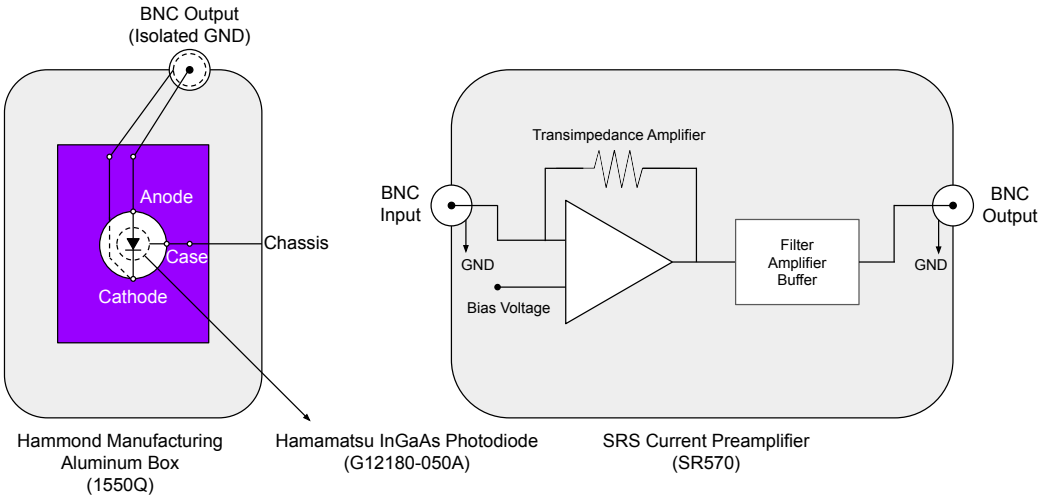

Figure 4.1: The design of a large aperture photodiode module.

design of the photodiode module is relatively simple. As shown in Fig. 4.1, it consists of a Hamamatsu InGaAs PIN photodiode (G12180-050A) with a sensitivity diameter of 5 mm, a customized PCB, a compact aluminum chassis from Hammond Manufacturing (1550Q), and a SRS current preamplifier (SR570) that converts the photodiode current to an output voltage while providing an internal applied biased voltage, various filters and sensitivity options. The biased voltage should be maintained negative in order to keep the photodiode properly reverse biased. When the photodiode is reverse biased, it is in the so-called photoconductive mode, the junction capacitance decreses and the response time of the photodiode becomes lower, i.e. higher bandwidth. The lid of the chassis box is custom machined to be cage-mount compatible for the use of lens and neutral-density filters.

Fig. 4.2 shows the calibrated results for the photodiode module. The testing condi-

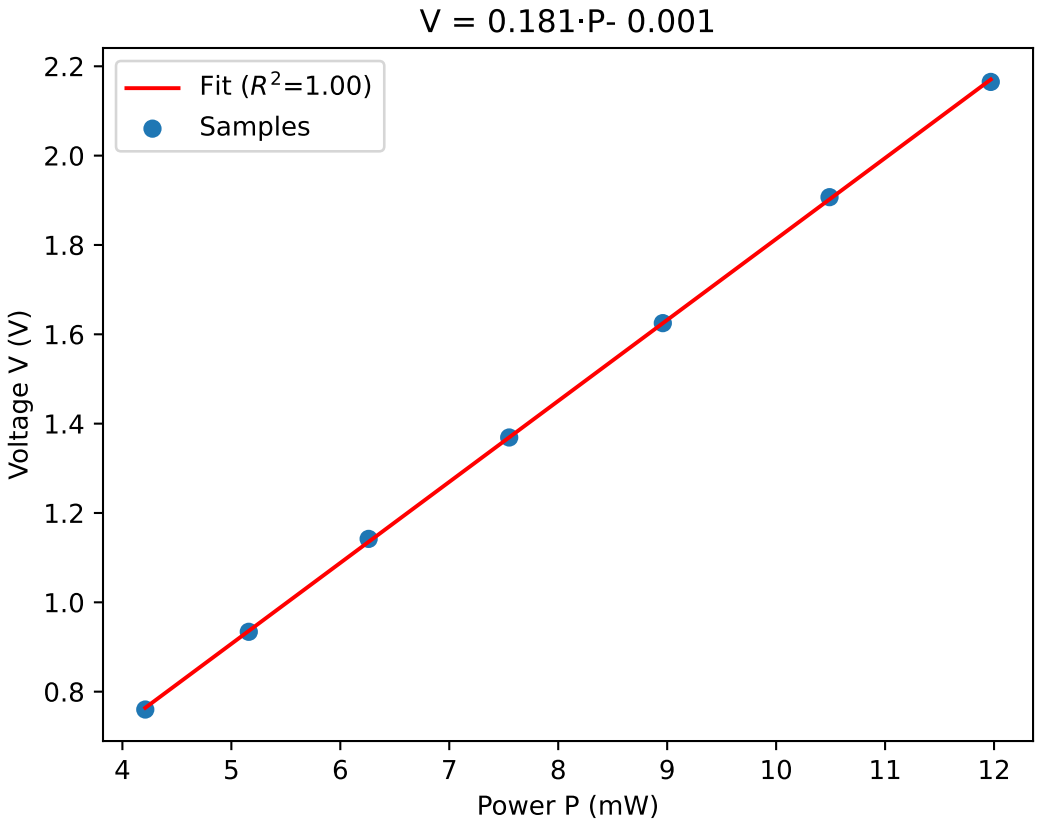

Figure 4.2: Calibration curve for the large aperture photodiode in reverse biased mode with the current preamplifier, taken on 5/21/25. An ND2 filter was placed in front of the photodiode. The current preamplifier sensitivity was set to 100 $\frac{\mu A}{V}$ and the reverse biased voltage was at -1 V.

tions were:

- Photodiode sensitivity: 0.6 $\frac{A}{W}$
- ND 2 filter (NE20A)
- Reverse biased voltage: -1 V
- Current preamplifier sensitivity: 100 $\frac{\mu A}{V}$

Overall, the power to voltage relationship is very linear $R^2 = 1.00$, with a factor of three different from the predicted sensitivity due to the three time higher transmission of the

ND 2 filter at 1064 nm (as opposed to the calibrated 0.01 % transmission at 633 nm). The output voltage range can be expanded by increasing the sensitivity of the current preamplifier so that the full dynamic range can be utilized. In addition, filters should be applied for the intensity stabilization of the lattice beam to suppress high frequency noise. The bandwidth of the photodiode module was measured to be about 100 kHz by pulsing the beam on / off with an AOM, using the low noise mode in the current preamplifier.

4.2 MRC Laser Pointing Stabilization

In addition to addressing power fluctuations of our lattice beam, another major contribution to lattice depth drift is the relative positional stability of the beam. Passive and active stabilization of beam pointing has been demonstrated by many groups in the past, with a couple listed [30, 31]. In our system, we utilize a commercial active laser beam pointing stabilization system from MRC GmbH. Below I will describe the components included in the system and their integration into our existing beam path, along with empirical advice on beam alignment for achieving good positional stability.

4.2.1 Components

A list of components we obtained from MRC GmbH are included below with brief discussion on the functionality for each of them:

- **Controller** The "Brain" of the entire feedback system. Along with the software, it coordinates all the sensing, beam manipulation, and logging tasks, as well as common feedback features.
- **Position Sensitive Detector (PSD)** ($\times 2$) The PSD is responsible for detecting

the beam position. Ideally, the beam "image" at the PSD should be identical to the beam profile viewed by the atoms. It provides a detection area of 9×9 mm^2 with a submircon resolution and a sampling bandwidth greater than 30 kHz.

- **Piezo Steering Mirror Mount (P2S30)** ($\times 2$) It is a fast piezo-driven tilting 1 inch mirror mount used to compensate for beam deviation and direct it back to the correct setpoint. It has a 2 mrad mechanical tilting range and a 4 mrad optical tilting range. The piezo drive signal is provided by the controller.

- **"Sample and Hold" (ADDA)** This feature fixes the beam to its last stabilization positions by maintaining constant piezo voltages. It temporarily pauses the closed-loop feedback while not resetting the beam positions. The external inputs in the controller allows us to independently apply this feature to each of the two feedback loops.

- **"Adjust-in"** This function enables us to finely adjust the beam position setpoints in the software (through *Set&Hold*) over the entire PSD area. It is a very convenient feature when we are in need of fine-tuning the beam position relative to the atoms. (similar to the usage of Picomotor for other beam alignments in our lab). The setpoints can also be adjusted by external applied voltages through the controller.

- **"Drive Actuator"** The piezo actuators, and thus the beam positions, can be controlled open-loop through this feature, either with computer commands, or external voltage signals to the controller.

- **"External Activation"** This allows us to enable/disable the feedback loops independently through two external TTL signals. Note that by disabling the feedback, we also reset the piezo voltages, and the beam would be no longer aligned to the

correct setpoints. Due to the piezo's hysteresis, the beam alignment might need to be finely adjusted once the feedback loop is activated again.

4.2.2 Integration and Usage

Fig. 4.3 shows the existing lattice beam path with MRC pointing stabilization integrated. The pick-up mirror and the retro-reflective mirror mounts are replaced by the P2S30 piezo mirror mounts. Because the incoming beam and the retro-reflective beam contain four degrees of freedom (lateral displacement and incident angle $\times 2$), the set of two PSD and piezo actuators are insufficient to cover the entire parameter space. We decided to stabilize the lateral displacement drift in the atom's plane for both the incoming and retro-reflective beams as we believe that it presents a larger contribution to lattice depth instability. For the incoming beam, we use the small transmission through the polarized beam splitter to measure the beam position on PSD 1. By placing a duplicate lens one focal length (250 mm) away from PSD 1, the beam profile viewed by PSD 1 should be equivalent to that of the atoms. Any angular correction from the piezo mirror mount 1 is Fourier transformed to lateral displacement correction through the lens. Similarly, as the retro-reflective beam makes it round-trip back through the lens, the dichroic mirror after has finite transmission that can be utilized to measure the retro's beam position on PSD 2. The retro-reflective mirror then stabilizes any lateral position instability in the atom's plane.

After approximately directing the beams to the atomic positions, we fine tune the alignment using Kapitza-Dirac and the "Adjust-in" feature mentioned above. The active stabilization is turned on in between experimental runs. During the sequence, we send a TTL signal to both stages for enabling "Sample and Hold" so that the piezo voltages and thus the beam alignment remain unchanged. This decision of not having closed feedback

Figure 4.3: Optical lattice beam path with MRC stabilization integrated (not to scale). Both PSD 1 and PSD 2 and the second P2S30 piezo mirror mount are one focal length (250 mm) away from their respective lenses.

loop during the experiment is largely due to the concern of introducing high frequency noise from the piezo drive to the lattice depth or phase.

Fig. 4.4 are comparisons when the MRC stabilization is disabled or enabled. We see that without active beam pointing stabilization, there are significant beam positional drifts over the course of an hour (Fig. 4.4 (a-b)). It was discovered later that the sampled beam power on PSD 2 is significant lower than that on PSD 1, and that the beam is off-center relative to PSD 2. This leads to the artifact of larger fluctuating behavior with larger error bar compared to PSD 1. When MRC stabilization is enabled (Fig. 4.4 (c-d)), we see a more than ten-fold improvement in lowering the beam positional drifts for both incoming and retro-reflective beams. It shows that the beam positions can be maintained for eight hours without additional alignments. In fact, the lattice depth calibration with

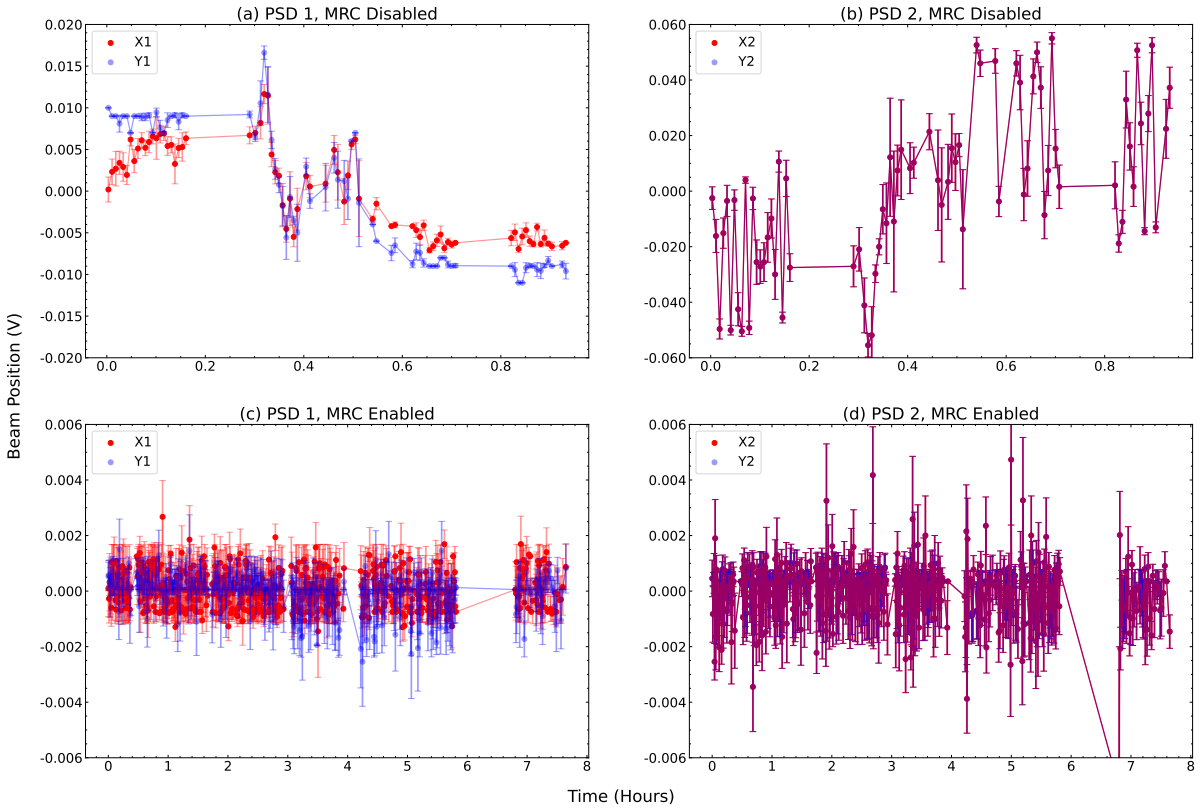

Figure 4.4: (a, b) Incoming and retro-reflective beam fluctuations around the mean position with MRC stabilization disabled, measured by PSD 1 (a) and PSD 2 (b), respectively. (c, d) Incoming and retro-reflective beam fluctuations around the mean position with MRC stabilization enabled, measured by PSD 1 (c) and PSD 2 (d), respectively. Each data point (error bar) represents the average (standard deviation of) beam fluctuation each time it is enabled in between experimental runs. Data taken by Xiao Chai on 4/11/25 and 4/16/25.

atoms seem to suggest that no extra alignment is needed for nearly two months during the time we are collecting the interferometer data.

Here I include some empirical suggestions for using the MRC stabilization system, discovered collectively by the entire Lithium team (in particular by Xiao Chai):

- The sampled beam power on both PSDs should be as high as possible ($\sim$ mW). We have observed that the detected positions are sensitive to the incident power, and this can be mostly mitigated by nearly saturating the PSDs. Specifically for PSD 2, one can control the polarization so that more power can transmit through

the dichroic and reach the PSD.

- Block stray light (e.g. other 1064 nm beams) by placing irises in front of the PSDs.
- Use long pass filters to block unwanted wavelengths, especially the one that transmits through the dichroic.
- Position the beams close to the PSDs' center.
- It is good to monitor the piezo voltages from time to time and make sure that they are not railed from failed feedback response.
- Override "Sample and Hold" enabled (TTL low) in Cicero when the machine or the 1064 nm laser is off. This prevents railing the piezo voltages by accidentally running the feedback loop without beam detection.
- Disabling the stabilization resets the piezo voltages to zero, and one should be cautious doing so. Due to the piezo's hysteresis behavior, alignment could be lost upon re-enabling the stabilization. Setting "Sample and Hold" is sufficient for most scenarios. In the cases of beginning an alignment from scratch or railed piezo voltages, we would need to disable the stabilization.

Chapter 5

Numerical Simulation

Chapter 5 describes some numerical methods to simulate or benchmark with the experimental results. Most of the simulations described below are GPU based to reduce computational time. It will include time-splitter spectral method in real space for time-dependent Schrodinger equation and Fourier space simulation in time-independent and time-dependent cases, specifically for temporal and spatial periodic systems.

5.1 GPU-Based Simulation with Python

Numerical calculation with graphical processing units (GPUs) can significantly increase computational speed for large size datasets because of its architecture suited for parallel processing. The CuPy package in Python allows for extremely convenient utilization of GPU to accelerate array operations and computations, through the incorporation of the existing Compute Unified Device Architecture (CUDA) toolkit. It is highly compatible with NumPy and SciPy, the standards packages for numerical calculations in Python, yet the operation time of large arrays with CuPy can be reduced by one or two orders of magnitude compared to the same tasks in NumPy and SciPy. Once the CuPy

package is installed and imported, most of the syntax and function names are identical to the ones in NumPy and CuPy. One can initialize the arrays in CuPy and implement array operations with the GPU. This means that all the associated arrays are stored in the GPU memory. If the arrays need to be accessed outside of the GPU memory for, for example, plotting in matplotlib or using functions only defined in NumPy/SciPy, one can simply convert it by *cp.asnumpy*(). This function transfer the array from the GPU memory to the random access memory (RAM), where arrays inilized from NumPy/SciPy are stored. It is also simple to transfer a NumPy array to a CuPy array by *cp.array*().

5.2 Time-Dependent Schrodinger Equation in Real-Space

Here I will briefly present the real-space simulation method used for the thesis, known as the time-splitting spectral methods [32, 33]. There are also good references from previous lab memebers of the Weld lab [34]. Consider the one-dimensional, time dependent Schrodinger equation:

$$i\hbar\frac{\partial\psi(x,\ t)}{\partial t} = \left[-\frac{\hbar^2}{2m}\frac{\partial^2}{\partial x^2} + V(x,\ t)\right]\psi(x,\ t) \tag{5.1}$$

with the initial wavefunction at t_0 being $\psi(x,\ t_0)$. The wavefunction at time t can be written as:

$$\begin{aligned}\psi(x,\ t) &= U(t,\ t_0)\psi(t_0) \\ &= \mathcal{T}\left[e^{-\frac{i}{\hbar}\int_{t_0}^{t} H(t')dt'}\right]\psi(x,\ t_0)\end{aligned} \tag{5.2}$$

where $U(t,\ t_0)$ is the unitary evolution operator from t_0 to t, and $\mathcal{T}$ being the time ordering operator. Because of the composition property of the unitary evolution operator $U(t_2,\ t_0) = U(t_2,\ t_1)U(t_1,\ t_0)$ [17], Eqn. 5.2 becomes:

$$\begin{aligned}\psi(x,\ t_N) &= U(t_N,\ t_{N-1})U(t_{N-1},\ t_{N-2})\cdots U(t_2,\ t_1)U(t_1,\ t_0)\psi(t_0) \\ &= \mathcal{T}\left[e^{-\frac{i}{\hbar}\int_{t_{N-1}}^{t_N} H(t')dt'} e^{-\frac{i}{\hbar}\int_{t_{N-2}}^{t_{N-1}} H(t')dt'} \cdots e^{-\frac{i}{\hbar}\int_{t_1}^{t_2} H(t')dt'} e^{-\frac{i}{\hbar}\int_{t_0}^{t_1} H(t')dt'}\right]\psi(x,\ t_0)\end{aligned} \tag{5.3}$$

where the final time t is denoted as t_N. The evolution operator from t_i to t_{i+1} therefore is:

$$\begin{aligned}U(t_{i+1},\ t_i) &= e^{-\frac{i}{\hbar}\int_{t_i}^{t_{i+1}} H(t')dt'} \\ &= e^{-\frac{i}{\hbar}\int_{t_i}^{t_{i+1}}\left[-\frac{\hbar^2}{2m}\frac{\partial^2}{\partial x^2}+V(x,\ t')\right]dt'} \\ &\approx e^{-\frac{i}{\hbar}\cdot-\frac{\hbar^2}{2m}\frac{\partial^2}{\partial x^2}\cdot\Delta t} e^{-\frac{i}{\hbar}\int_{t_i}^{t_{i+1}} V(x,\ t')dt'}\end{aligned} \tag{5.4}$$

where $\Delta t \approx t_{i+1} - t_i$, and in the last step the Baker-Campbell-Hausdorff formula is used to the first order as an approximation. If the time step Δt becomes small enough, the integration over the potential $V(x,\ t')$ in Eqn. 5.4 can be discretized:

$$U(t_{i+1},\ t_i) \approx e^{-\frac{i}{\hbar}\cdot-\frac{\hbar^2}{2m}\frac{\partial^2}{\partial x^2}\cdot\Delta t} e^{-\frac{i}{\hbar}V(x,\ t_i+\frac{\Delta t}{2})\Delta t} \tag{5.5}$$

The key to the time-splitting spectral methods is to notice that the kinetic operator becomes diagonalized in momentum space, where:

$$-\frac{\hbar^2}{2m}\frac{\partial^2}{\partial x^2} \rightarrow \frac{\hbar^2 k^2}{2m} \tag{5.6}$$

and k is the wavevector of the wavefunction. This means that by doing a Fourier transform to the real-space wavefunction $\psi(x,\ t)$, we can express it in the momentum basis

to be $\psi(k,\ t)$, in which now applying the kinetic operator becomes an element-wise multiplication between two one-dimensional arrays, and significantly reduces the complexity of applying the evolution operator. The wavefunction at t_{i+1} evolved from t_i can be expressed as:

$$\psi(x,\ t_{i+1}) \approx \mathcal{F}^{-1}\left\{e^{-\frac{i}{\hbar}\cdot\frac{\hbar^2k^2}{2m}\cdot\Delta t}\mathcal{F}\left\{e^{-\frac{i}{\hbar}V(x,\ t_i+\frac{\Delta t}{2})\Delta t}\psi(x,\ t)\right\}\right\} \tag{5.7}$$

where $\mathcal{F}$ denotes the Fourier transform and $\mathcal{F}^{-1}$ the inverse Fourier transform. Because of the existing numerical techniques on implementing fast Fourier transform (FFT), especially with the usage of GPU, the time-spliting spectral methods can be executed conveniently even in PCs to obtain reliable numerical results to compare with experiments. Using the second-order Strang splitting can improve the first-order scheme on the time-dependent potential in Eqn. 5.6:

$$\psi(x,\ t_{i+1}) \approx e^{-\frac{i}{\hbar}V(x,\ t_i+\frac{3\Delta t}{4})\Delta t}\cdot\mathcal{F}^{-1}\left\{e^{-\frac{i}{\hbar}\cdot\frac{\hbar^2k^2}{2m}\cdot\Delta t}\cdot\mathcal{F}\left\{e^{-\frac{i}{\hbar}V(x,\ t_i+\frac{\Delta t}{4})\Delta t}\psi(x,\ t)\right\}\right\} \tag{5.8}$$

Since the Gross–Pitaevskii equation is considered as a non-linear Schrodinger equation, the time-splitting spectral method also applies. Because the mean-field interaction term ($I(x,\ t) =\ g|\psi(x,\ t)|^2$) in the equation can be fully expressed in the position space, we can simply combine the interaction term with the potential term.

$$\begin{aligned}\psi(x,\ t_{i+1}) \approx\ & e^{-\frac{i}{\hbar}\left[V(x,\ t_i+\frac{3\Delta t}{4})+I(x,\ t_i+\frac{3\Delta t}{4})\right]\Delta t}\cdot \\ & \mathcal{F}^{-1}\left\{e^{-\frac{i}{\hbar}\cdot\frac{\hbar^2k^2}{2m}\cdot\Delta t}\cdot\mathcal{F}\left\{e^{-\frac{i}{\hbar}\left[V(x,\ t_i+\frac{3\Delta t}{4})+I(x,\ t_i+\frac{3\Delta t}{4})\right]\Delta t}\psi(x,\ t)\right\}\right\}\end{aligned} \tag{5.9}$$

The time-splitting spectral methods are time reversible, mass conserved, energy conserved, as well as being unconditionally stable [32]. It is second-order accurate in time and spectrally accurate in the spatial dimension, meaning that the spatial accuracy de-

pends on the spatial step size rather than a fixed order. Other methods include the Crank-Nicolson finite difference method, semi-implicit finite difference method, etc.

Below I show a breakdown of my code implementation of the time-splitting spectral methods specifically for an optical lattice potential.

1. Input the experimental parameters

    - Input lattice depth and quasimomentum width. Typically we place a gaussian envelop over the initial wavefunction because of the finite quasimomentum width of the BEC.
    - Input Atom mass, atom number, beam waist, scattering length to calculate the g factor in the interaction term.
    - Input the potential or force parameters, usually related to the modulation waveforms or the force configuration.

2. Initialize a spatial grid from x_0 to x_N with periodic boundary conditions ($x_0 = x_{N+1}$). The momentum grid can be found by using $2\pi \cdot \mathit{fftfreq}(N,\ \Delta x)$, where the first input takes in the total number of points in the spatial grid and the second input takes the spatial step size. The range and step size of the spatial grid depends on the specific conditions of the experiment.

3. Initialize a time array from initial to final time with a relatively small time step.

4. Calculate/create the initial state, which often is the product of a gaussian and a Bloch state or an interacting ground state obtained from imaginary time evolution.

5. Time evolve the initial wavefunction using Eqn. 5.9. Calculate and save the appropriate observables or wavefunctions for the experiment.

6. Save the relevant data and plot them.

Most of the above, especially with the FFT and the time evolution, are done with CuPy and GPU. The simulation is object-oriented based, and many of the parameters above are declared as class attributes. For example, there is a class "Atom_Laser_Properties" associated with all the atom and trapping laser parameters, whereas a class "Spatial_Grid" to automatically generate all the spatial and momentum arrays. The simulation class uses inheritance to obtain all the class attribes from those two classes. In addition, a for loop is used for the time evolution of the wavefunction to repeat through each time step. Inside the loop, the potential is updated as a class attribute each time for possible new parameters, and the wavefunction propagation is fully completed with variables declared within the class.

5.2.1 Imaginary Time Propagation

The imaginary time propagation method allows us to find the real ground state of a mean-field interacting Hamiltonian by making the following substitution:

$$t \to -i\tau \tag{5.10}$$

I will show a simple case to illustrate how the substituion would lead to a ground state. Consider a time-independent Hamiltonian, Eqn. 5.2 in the basis of energy eigenstates becomes

$$\psi(x,\ t) = \sum_n e^{-i\frac{E_n}{\hbar}t}\psi_n(x) \tag{5.11}$$

Using the substitution in Eqn. 5.10, it shows:

$$\psi(x) = \sum_i e^{-\frac{E_n}{\hbar}\tau}\psi_n(x) \tag{5.12}$$

Since all excited states have a faster decay rate during the imaginary time propagation due to their higher energies, a sufficiently long propogation time will only leave the interacting ground state component non-zero. Normalizing the final wavefunction would yield the true ground state of the system.

For imaginary time propagation of the Gross-Pitaevskii equation, one considers the time-independent version:

$$\mu\psi(x,\ t) = \left[-\frac{\hbar^2}{2m}\frac{\partial^2}{\partial x^2} + V(x,\ t) + g|\psi(x,\ t)|^2\right]\psi(x,\ t) \tag{5.13}$$

where μ is the chemical potential of the system. The imaginary time propagation takes the form of Eqn. 5.9 with time being imaginary. At each time step, one can obtains the chemical potential of the system by integrating Eqn. 5.13 with the complex conjugate of the wavefunction ψ^*:

$$\mu N = \int \psi^* \left[-\frac{\hbar^2}{2m}\frac{\partial^2}{\partial x^2} + V(x,\ t) + g|\psi|^2\right]\psi \tag{5.14}$$

where N is the total particle number, with the normalization condition of $\int |\psi|^2 dx = N$. To start the imaginary time evolution, one typically uses the Thomas-Fermi approximation as the initial wavefunction. The imaginary time propagation can be paused once the chemical potential reaches the set threshold, and the wavefunction would become the true interacting ground state. If the potential used in the imaginary time propogation is the same as that at the initial time of the real time propagation $V(x,\ t = 0)$, we would have an initial state that is the true ground state of the mean-field interacting Hamiltonian.

5.3 Temporal-Spatial Periodic Potential in Fourier Space

When the potential is spatially periodic, one also has the option to perform the simulation in Fourier space with the Bloch Hamiltonian matrix and the Bloch functions u_{nk}. In this case, all the operations become effectively finite-dimensional matrix-vector multiplications, which can sometimes reduce computational time, especially if it is with CPU. Below I will give an example of spatial periodicity using the one-dimensional optical lattice potential, and later combines amplitude modulation (temporally periodic) to construct Floquet-Bloch bands.

5.3.1 Time-Independent Case

The one-dimensional time-independent optical lattice Hamiltonian is:

$$H = \frac{p^2}{2m} - V_0 \cos^2(k_L x) \tag{5.15}$$

Solving the time-independent Schrodinger equation with this Hamiltonian is equivalent to solving the eigenvalue equation written in Eqn. 2.44. In there, the equation is written

in index notation, expanding it gives:

$$\begin{pmatrix} \frac{\hbar^2 k_L^2}{2m}(2\cdot -l+\frac{q}{\hbar k_L})^2 & -\frac{V_0}{4} & 0 & \cdots & 0 \\ -\frac{V_0}{4} & \frac{\hbar^2 k_L^2}{2m}(2\cdot(-l+1)+\frac{q}{\hbar k_L})^2 & -\frac{V_0}{4} & \cdots & 0 \\ 0 & -\frac{V_0}{4} & \ddots & \ddots & \vdots \\ \vdots & \vdots & \ddots & \ddots & -\frac{V_0}{4} \\ 0 & 0 & \cdots & -\frac{V_0}{4} & \frac{\hbar^2 k_L^2}{2m}(2l+\frac{q}{\hbar k_L})^2 \end{pmatrix} \begin{pmatrix} c_{-l}^{nq} \\ c_{-l+1}^{nq} \\ \vdots \\ c_{l-1}^{nq} \\ c_{l}^{nq} \end{pmatrix}$$

$$= \frac{\hbar^2 k_L^2}{2m} E_{nq} \begin{pmatrix} c_{-l}^{nq} \\ c_{-l+1}^{nq} \\ \vdots \\ c_{l-1}^{nq} \\ c_{l}^{nq} \end{pmatrix} \tag{5.16}$$

An constant offset from the potential in the diagonal terms are neglected here. We can readily use an eigenequation solver to numerically obtain the set of eigenvectors and eigenvalues for a particular quasimomenum q. The n-th eigenvector and eigenvalue in the solution correspond to the Bloch state and energy of the n-th band. As we see, the Bloch Hamiltonian is a sum of the kinetic energy P (diagonal) matrix and the potential

energy V (off-diagonal) matrix:

$$\hat{P} \equiv \frac{\hbar^2 k_L^2}{2m} \begin{pmatrix} (2\cdot -l + \frac{q}{\hbar k_L})^2 & 0 & 0 & \cdots & 0 \\ 0 & (2\cdot(-l+1) + \frac{q}{\hbar k_L})^2 & 0 & \cdots & 0 \\ 0 & 0 & \ddots & \ddots & \vdots \\ \vdots & \vdots & \ddots & \ddots & 0 \\ 0 & 0 & \cdots & 0 & (2l + \frac{q}{\hbar k_L})^2 \end{pmatrix} \tag{5.17}$$

$$\hat{V} \equiv -\frac{V_0}{4} \begin{pmatrix} 0 & 1 & 0 & \cdots & 0 \\ 1 & 0 & 1 & \cdots & 0 \\ 0 & 1 & 0 & \ddots & \vdots \\ \vdots & \vdots & \ddots & \ddots & 1 \\ 0 & 0 & \cdots & 1 & 0 \end{pmatrix} \tag{5.18}$$

5.3.2 Time-Dependent Case

The time evolution of the system in Fourier space is similar to that in position space using the spectral method, except that now it is a matrix-vector multiplication with a much smaller matrix dimension. The advantages of Fourier space simulation are that it is faster to perform array operations of smaller size arrays, and that we don't need to worry about boundary effects from the finite extend of the spatial grid. However, it only works for Hamiltonians that can be written as a matrix in Fourier space, i.e. spatially periodic Hamiltonians, or under special scenario such as Bloch oscillation.

The time evolution operator $U(t,\ t_0)$ is:

$$U(t,\ t_0) = \mathcal{T}\left[e^{-\frac{i}{\hbar}\int_{t_0}^{t} H(t')dt'}\right] \tag{5.19}$$

From the composition property, again, this can be written as:

$$U(t,\ t_0) = \mathcal{T}\left\{\prod_{i=0}^{N-1} e^{-\frac{i}{\hbar}\int_{t_i}^{t_{i+1}} H(t')dt'}\right\} \tag{5.20}$$

Discretizations of the Hamiltonian integral over time yields:

$$U(t,\ t_0) = \mathcal{T}\left\{\prod_{i=0}^{N-1} e^{-\frac{i}{\hbar}H(t_i+\frac{\Delta t}{2})\Delta t}\right\} \tag{5.21}$$

assuming Δt is sufficiently small. Eqn. 5.21 constructs a evolution matrix at each time step, i.e. $U(t_{i+1},\ t_i) = e^{-\frac{i}{\hbar}H(t_i+\frac{\Delta t}{2})\Delta t}$, and then multiple it by the wavefunction from the previous step.

$$\begin{aligned}\psi(t_N) &= U(t_N,\ t_{N-1})U(t_{N-1},\ t_{N-2})\cdots U(t_2,\ t_1)\psi(t_0) \\ &= e^{-\frac{i}{\hbar}H(t_{N-1}+\frac{\Delta t}{2})\Delta t}e^{-\frac{i}{\hbar}H(t_{N-2}+\frac{\Delta t}{2})\Delta t}\cdots e^{-\frac{i}{\hbar}H(t_0+\frac{\Delta t}{2})\Delta t}\psi(t_0)\end{aligned} \tag{5.22}$$

Since we know how to write the Hamiltonian in matrix form, we can construct the evolution operator by taking the matrix exponential of the Hamiltonian (for example, the function is *expm()* in Python) along with other factors. With an initial wavefunction written as an one-dimensional array, Eqn. 5.22 is simply a series of matrix exponential operation and matrix-vector multiplication repeated through each time step.

5.3.2.1 Floquet-Bloch Bands

Here I will show an example of an one-dimensional amplitude modulated optical lattice potential with the form of:

$$H = \frac{p^2}{2m} - V_0\left[1 + \alpha\sin(\omega_D t)\right]\cos^2(k_L x) \tag{5.23}$$

where α and ω_D are the modulation amplitude and modulation angular frequency, respectively. The Bloch Hamiltonian is similar to that of the static case, except now that the potential (off-diagonal) matrix is time-dependent. The kinetic energy term remains the same as before.

$$\hat{P} \equiv \frac{\hbar^2 k_L^2}{2m} \begin{pmatrix} (2 \cdot -l + \frac{q}{\hbar k_L})^2 & 0 & 0 & \cdots & 0 \\ 0 & (2 \cdot (-l+1) + \frac{q}{\hbar k_L})^2 & 0 & \cdots & 0 \\ 0 & 0 & \ddots & \ddots & \vdots \\ \vdots & \vdots & \ddots & \ddots & 0 \\ 0 & 0 & \cdots & 0 & (2l + \frac{q}{\hbar k_L})^2 \end{pmatrix} \tag{5.24}$$

$$\hat{V}(t) \equiv -\frac{V_0}{4}\left[1 + \alpha \sin(\omega_D t)\right] \begin{pmatrix} 0 & 1 & 0 & \cdots & 0 \\ 1 & 0 & 1 & \cdots & 0 \\ 0 & 1 & 0 & \ddots & \vdots \\ \vdots & \vdots & \ddots & \ddots & 1 \\ 0 & 0 & \cdots & 1 & 0 \end{pmatrix} \tag{5.25}$$

Eqn. 5.22 becomes:

$$\psi(t_N) = e^{-\frac{i}{\hbar}\left[\hat{P} + \hat{V}(t_{N-1} + \frac{\Delta t}{2})\right]\Delta t} e^{-\frac{i}{\hbar}\left[\hat{P} + \hat{V}(t_{N-2} + \frac{\Delta t}{2})\right]\Delta t} \cdots e^{-\frac{i}{\hbar}\left[\hat{P} + \hat{V}(t_0 + \frac{\Delta t}{2})\right]\Delta t} \psi(t_0) \tag{5.26}$$

which gives the state ψ at any time in terms of the matrix exponential of $\hat{P}$ and $\hat{V}(t)$.

Because the Hamiltonian in Eqn. 5.23 is spatial and temporal periodic, it is invariant under:

$$x \to x + a = x + \frac{\pi}{k_L} \tag{5.27}$$

$$t \to t + T = t + \frac{2\pi}{w_D} \tag{5.28}$$

We can apply both Bloch's theorem and Floquet theorem, and the ansatz is the Floquet-Bloch state $\psi_{nq}(x,\ t)$:

$$\tilde{\psi}_{nq}(x,\ t) = e^{\frac{i}{\hbar}(qx-\epsilon_{nq}t)}\tilde{u}_{nq}(x,\ t) \tag{5.29}$$

where ϵ_{nq} is the quasienergy, and $\tilde{u}_{nq}(x,\ t)$ is the Floquet-Bloch function with the same spatial and time translation invariances as the Hamiltonian:

$$\tilde{u}_{nq}(x,\ t) = \tilde{u}_{nq}(x + \frac{\pi}{k_L},\ t) = \tilde{u}(x,\ t + \frac{2\pi}{w_D}) \tag{5.30}$$

The set of quasienergies ϵ_{nq} and the Floquet-Bloch functions $u_{nq}(x,\ t)$ at each quasi-momentum q can be found by numerically diagonalizing the Floquet Hamiltonian H_{F} [10, 12]. This can be done through the following procedure:

1. Construct the Hamiltonian $H(t_i)$ in Fourier space with $\hat{P}$ and $\hat{V}(t_i)$, and its corresponding evolution operator $U(t_{i+1}, t_i)$ through matrix exponential.

2. Obtain the one period, stroboscopic time evolution operator $U(T)$ through numerical time propagation:

$$\begin{aligned} U(T = t_N) =& U(t_N,\ 0) \\ =& U(t_N = T,\ t_{N-1})U(t_{N-1},\ t_{N-2}) \cdots U(t_2,\ t_{11})U(t_1,\ t_0 = 0) \end{aligned} \tag{5.31}$$

3. Obtain the Floquet Hamiltonian H_{F} by taking matrix logarithmic of $U(T)$:

$$H_{\mathrm{F}} = i\frac{\hbar}{T}\ln U(T) \tag{5.32}$$

4. Compute the transition probability, or the overlap absolute squared, etween the i-th Bloch functions of the static lattice and the j-th Floquet-Bloch functions of the driven lattice $P_{ij} = |\ \langle u_{iq}|\tilde{u}_{jq}\rangle\ |^2$.

5. Order the set of quasienergies $\{\epsilon_{nq}\}$ and the Floquet functions $\{\tilde{u}_{nq}\}$ by descending order of the transition probability P_{ij}. The first ordered element corresponds to the lowest-quasienergy state at this specific quasimomentum.

By repeating the process above for half of the quasimomenta in the 1st *Brillouin* zone (because the bands are symmetric around $q = 0$), one can find the so-called Floquet-Bloch band structures. It is the spectrum of the system within the 1st *Brillouin* zone of both quasimomentum and quasienergy due to its spatial-temporal periodic nature. Fig. 5.1 shows an example of the Floquet-Bloch band structure at a lattice depth V_0 of 8 E_R. The first seven static band components are included in the band structure. The modulation frequency $f_D = \frac{\omega_D}{2\pi}$ and amplitude α are 210 kHz and 0.2, respectively.

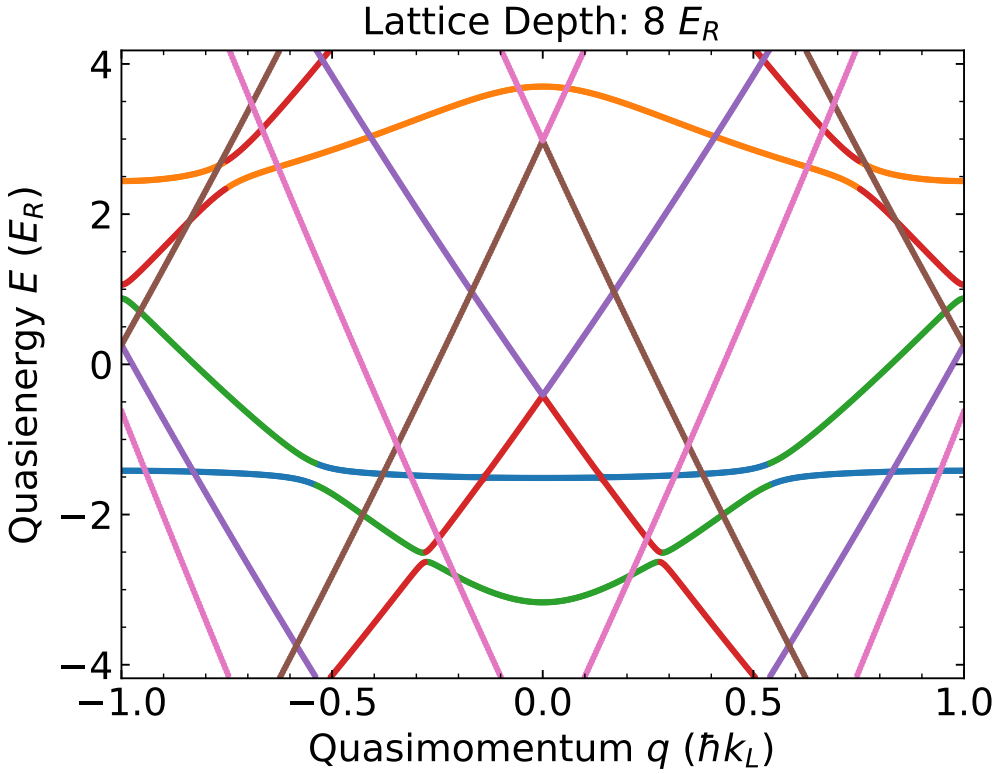

Figure 5.1: Floquet-Bloch band structure considering the first seven static Bloch bands. The lattice depth V_0 is 8 E_R, and the modulation frequency f_D and modulation amplitude α are 210 kHz and 0.2, respectively.

Chapter 6

Trapped Matter-Wave Floquet-Bloch Interferometry

In **Chapter 6**, I will discuss the experimental realization of a novel trapped matter-wave interferometer using Floquet-Bloch band structures.

Interferometry utilizes interference of waves to extract signals, often precise, from the fringe measurements. From the original Michelson interferometer in 1887 [35] to the modern Laser Interferometer Gravitational-Wave Observatory (LIGO) [36], optical interference has always been at the frontier of contemporary physics. The wave nature of massive matter extends such notion and allows one to develop atom-based interferometry [37, 38]. Since its first demonstrations [39, 40] and measurements of gravity [41], free fall interferometry has reached record-high sensitivity using large-scale apparatus to increase the free fall time, like that of the 100-meter drop towers [42] and of low Earth orbit [43]. Complementary approaches with continuously-trapped atoms offer an alternative route to achieve long coherence time at the presence of an external trap [44]. However, the systematic effects introduced from the trapping potential remain a key challenge for further improvements. Below I will present a new type of atom interferometer, where

atoms are undergoing position-space Bloch oscillations and being trapped in a Floquet engineered optical lattice that is first order insensitive to lattice intensity fluctuation.

6.1 Theory

The important ingredients for our interferometer experiments are an non-interacting ^{7}Li BEC, an amplitude-modulated optical lattice, and an applied, co-linear magnetic gradient. The Hamiltonian of the system can be written as:

$$H(t) = \frac{p^2}{2m} - V_0 \left[1 + \alpha \sin(\omega_D t)\right] \cos^2(k_L x) - \mathcal{F}x \tag{6.1}$$

where the concepts of Bloch oscillations and the amplitude modulated lattice have been discussed separately in Section 2.2.3 and Section 5.3.2.1, respectively. Similar to the case of a static lattice, the force term can be absorbed into the atom's momentum with the gauge $U_G = e^{i\frac{x}{\hbar}\mathcal{F}t}$:

$$H(t) = \frac{(p + \mathcal{F}t)^2}{2m} - V_0 \left[1 + \alpha \sin(\omega_D t)\right] \cos^2(k_L x) \tag{6.2}$$

Instead of the "broken" spatial translation symmetry, the system now no longer possesses discrete time translation symmetry. However, under the adiabatic approximation at the weak force limit, the system's wavefunction can still be represented by the instantaneous Floquet states. This is known as the instantaneous Floquet-state (ISF) formalism [45, 46, 47]. If the initial wavefunction is a Floquet-Bloch state at a quasimomentum q_0 with a band index n,

$$\psi(x,\ 0) = \tilde{\psi}_{nq_0}(x,\ 0) \tag{6.3}$$

the evolution of this wavefunction under Eqn. 6.2 is given by:

$$\psi(x,\ t) = e^{-i\phi_{\mathrm{Dyn},n}(t)}\tilde{\psi}_{nq(t)}(x,\ t) \tag{6.4}$$

where $q(t)$ is the new quasimomentum at time t:

$$q(t) = q_0 + \mathcal{F}t \tag{6.5}$$

and $\phi_{\mathrm{Dyn},n}(t)$ is the dynamical phase for band n, defined as:

$$\phi_{\mathrm{Dyn},n}(t) = \frac{1}{\hbar\mathcal{F}}\int_{q_0}^{q(t)} \tilde{\epsilon}_{nq}dq \tag{6.6}$$

This shows that the idea of Bloch oscillations is still applicable in Floquet-Bloch bands.

As we can see in Eqn. 6.6, the wavefunctions at different bands accumulate different amount of dynamical phase during Bloch oscillations, due to variations in band dispersion. This leads to a relative phase difference that is physically meaningful and experimentally measurable. In order to generate matter-wave splitting at two bands, we engineer a Landau-Zener tunneling [48, 49, 50] at a chosen avoided crossing. For a Landau-Zener transition occurring at the quasimomentum q_r between two Floquet-Bloch bands, one lower (L) band and one upper (U) band, the transition probability is:

$$p = e^{-2\pi\delta} \tag{6.7}$$

with the adiabaticity parameter δ:

$$\delta = \frac{\Delta_{q_r}^2}{4\hbar v} \tag{6.8}$$

where Δ_{q_r} is the gap size of the avoided crossing at quasimomentum q_r, and v is the Landau-Zener sweep velocity:

$$v = \mathcal{F}\sqrt{2\Delta_{q_r}\left|\left(\frac{\partial^2\epsilon_{\mathrm{L},q}}{\partial q^2}\right)\Big|_{q=q_r}\right|} \tag{6.9}$$

For atoms initially in only one of the two lower or upper bands, we can enforce a 50-50 splitting into both bands ($p = e^{-2\pi\delta} = 0.5$), by tuning the modulation amplitude α in Eqn. 6.2, and therefore the gap size Δ_{q_r}.

Implementing two consecutive 50-50 splitters through the Landau-Zener transitions at two different quasimomenta q_r and $q_{r'}$, during which the atoms in the lower and upper bands accumulate different dynamical phases, one forms the so-called Landau-Zener-Stückelberg-Majorana interferometer. Assuming the atoms are initially at the upper band, the final population imbalance at the output is given by:

$$\mathcal{I} \equiv P_{\mathrm{L}} - P_{\mathrm{U}} \approx 4p(1-p)(1+\cos(\phi_{\mathrm{Int}})) \tag{6.10}$$

where P_{L} (P_{U}) denotes the final population fraction at the lower (upper) band. The interferometry phase ϕ_{Int} is:

$$\phi_{\mathrm{Int}} = \phi_{\mathrm{Dyn,\ diff}} + 2\phi_{\mathrm{Sto}} \tag{6.11}$$

where the differential dynamical phase $\phi_{\mathrm{Dyn,\ diff}}$ is:

$$\phi_{\mathrm{Dyn,\ diff}} = \frac{1}{\hbar\mathcal{F}}\int_{q_r}^{q_{r'}} (\epsilon_{\mathrm{U},q} - \epsilon_{\mathrm{L},q})\, dq \tag{6.12}$$

and the Stokes phase ϕ_{Sto} is:

$$\phi_{\text{Sto}} = -\frac{\pi}{4} + \delta\left[\ln(\delta) - 1\right] + \arg\Gamma(1 - i\delta) \tag{6.13}$$

The differential dynamical phase is inversely proportional to the applied force, which means that the Landau-Zener-Stückelberg-Majorana interferometer nature exhibits larger sensitivity when the force is small. The two Stokes phase accumulations in Eqn. 6.11 originates from the two Landau-Zener transitions, and they are only weakly dependent of the force. With the force strength in our experimental setup, the interferometry phase ϕ_{Int} is dominated by the differential dynamical phase $\phi_{\text{Dyn, diff}}$ that scales with the area enclosed by the quasienergy-momentum loop in momentum space, or equivalently, the area enclosed by the space-time loop in position space. Because the wavefunction trajectories are adiabatically connected for both bands, one might imagine that there is a non-trivial differential Berry phase developed through the interferometry loop. However, it can be shown that such a differential phase can be removed through gauge transformation.

6.2 Floquet-Bloch Atom Interferometer

Fig. 6.1 (a) shows the experimental sequence for an interferometry loop of size 0.6 $\hbar k_L$. We prepare an non-interacting ^{7}Li BEC of 10^5 atoms in a horizontal crossed optical dipole trap (ODT) with trapping frequencies $(\nu_x,\ \nu_y,\ \nu_z) = (151.9,\ 185.0,\ 239.4)$ Hz. The atoms are initially prepared in the magnetically sensitive $|f = 1,\ m_f = 1\rangle$ ground state. The s-wave scattering length is tuned to zero by applying a magnetic field of 543.6 G. We transfer the atoms from the ODT to an one-dimensional horizontal optical lattice (V_0 = 8.45 E_R) adiabatically in 200 ms. A uniform force is used to induce Bloch oscillations

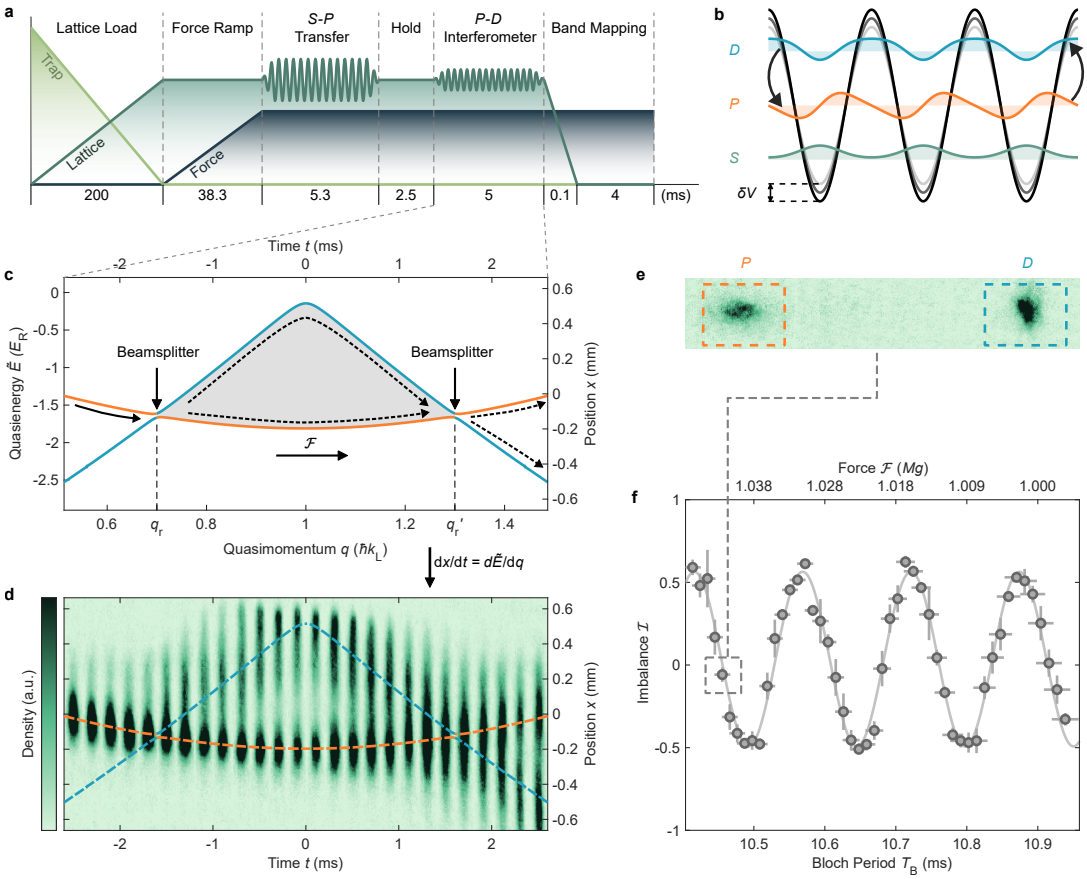

Figure 6.1: Experimental demonstration of Floquet-Bloch matter-wave interferometry. **(a)** The experimental sequence for an interferometry loop of size 0.6 $\hbar k_L$, centered at 1 $\hbar k_L$. **(b)** The schematic of an amplitude modulated optical lattice coupling the P and D static Bloch bands. The modulation strength is set as $\alpha = \delta V$. **(c)** The Floquet-Bloch band structure from hybridization of the P and D static Bloch bands in the extended zone scheme. The modulation is resonant at the quasimomenta $q_r = 0.7\ \hbar k_L$ and $q_{r'} = 1.3\ \hbar k_L$, and opens up an energy gap. Color represent the static Bloch band that is maximally overlapped with the Floquet-Bloch band. The solid arrow indicates the direction of the applied force $\mathcal{F}$. **(d)** Position-space Bloch oscillations mapping out the Floquet-Bloch band structure shown in (c), based on the equivalence of group velocity and energy dispersion relation. This forms an interferometry loop from the dynamical phase difference of the two hybridized bands. **(e)** Projection of Bloch states into free momentum states ("Band Mapping") after a time-of-flight to measure the final atom population in each band. **(f)** Interference fringes with respect to the applied force. Each force corresponds to a Bloch oscillation period. g is the local gravatational acceleration. The vertical error bars indicate the standard error after 3 repeats and the horizontal error bars are estimated error from the force calibration fit.

along the lattice direction through a set of magnetic field gradient with the effective strength $\mathcal{F}$. A strong pulse of 120 kHz amplitude modulation is applied resonantly to transfer all the atoms from the S band to the P band through a Landau-Zener transition at an avoided crossing. After a 2.5 ms hold time, we begin the interferometer experiment using a $P - D$ interferometric loop shown in Fig. 6.1 (c). The static P band and D band are hybridized using a second, 5 ms amplitude modulation pulse to form a Floquet-Bloch band structure. The modulation frequency was set to 127.438 kHz to create 50-50 Landau-Zener splittings between the two Floquet-Bloch bands at the quasimomenta $q_r = 0.7$ and $q_{r'} = 1.3$. Because of the concept of group velocity being equivalent to the band dispersion mentioned in Eqn. 2.58, as well as the light mass of lithium, the atoms' Bloch oscillation can also be observed in position space. Fig. 6.1 (d) shows the $P - D$ loop in position space through Bloch oscillations with a time sequence of in-situ images. As shown in Fig. 6.1 (f), by varying the applied force strength, the final atom population at each band oscillates due to the change in the differential dynamical phase defined in Eqn. 6.12. The final atom populations at the output were measured using standard Band Mapping techniques [51], where the lattice is ramped in 100 μs, followed by a TOF of 4 ms. This forms a compact matter-wave interferometer that can be used for precision force sensing.

6.3 Magic Lattice Depth

As mentioned above, trapped matter-wave interferometers often suffer from systematics introduced by the external trapping potential. In analogous to the magic wavelengths employed in optical lattice clocks [52], there exists a magic lattice depth in trapped matter-wave interferometry that has been demonstrated in static Bloch bands [53]. In this work, we extend this concept to Floquet-Bloch bands and experimentally verify that

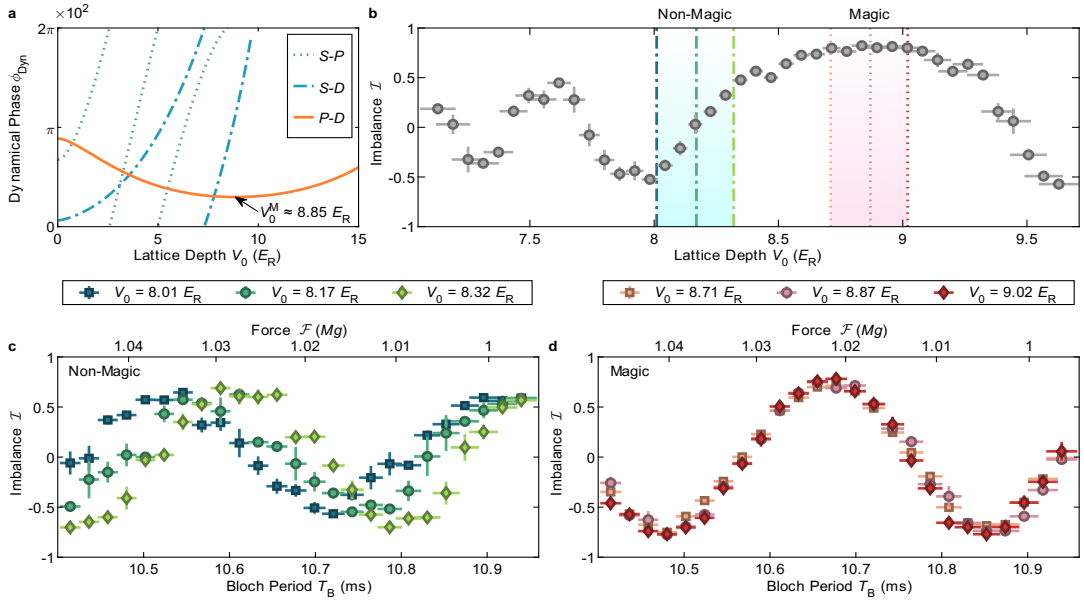

Figure 6.2: Magic Floquet-Bloch band structure. **(a)** Differential dynamical phase modulo $2\pi \times 10^2$ with respect to the lattice depth, for $S-P$, $S-D$, and $P-D$ interferometry loops. This is numerically calculated with a Bloch period $T_B = 10.7$ ms. Only the $P-D$ loop exhibits a sign of magicness, i.e. there exists a local minimum, at $V_0 \approx 8.85\ E_R$. **(b)** Experimental measured output imbalance $\mathcal{I}$ with respect to lattice depth. The imbalance is largely insensitive to lattice depth in between 8.6 E_R and 9.1 E_R. The non-magic and magic dashed lines represent the lattice depths at which we perform fringe scans with varying force, as shown in (c) and (d). **(c)** Imbalance measurement with varying force when the lattice depth is non-magic. The overall interferometry phase is offset from fluctuations in lattice depth. **(d)** Imbalance measurement with varying force when the lattice depth is magic. The overall interferometry phase is independent of the change in lattice depth, indicating its robustness against lattice intensity noise.

it offers first-order insensitivity to lattice intensity noise.

In order to characterize the magic condition for the Floquet-Bloch bands, we numerically calculate the lattice depth at which

$$\frac{\partial \phi_{\text{Int}}}{\partial V_0} \approx \frac{\partial \phi_{\text{Dyn, diff}}}{\partial V_0} = 0 \tag{6.14}$$

The differential dynamical phases as a function of lattice depth are shown in Fig. 6.2 (a) for $S-P$, $S-D$, and $P-D$ interferometry loop. As we can see, only the $P-D$ loop

satisfies that magic condition where there is a local minimum in the lattice depth scan. Fig. 6.2 (b) shows the imbalance measurements with respect to the lattice depth at a fixed force. The fringes are insensitive to lattice depth fluctuations in the region labeled "magic", confirming the presence of magic lattice depth in Floquet-Bloch interferometry. In addition, Fig. 6.2 (c) and (d) are non-magic and magic comparisons for interferometer measurements of different applied force strength. The absolute interferometric phase is independent of variations in lattice depth only in the magic region.

6.4 Interferometer Sensitivity

To demonstrate the potential of precision quantum sensing with magic Floquet-Bloch interferometer, we perform force measurements with varying loop sizes at their magic conditions (Fig. 6.3 (a)). The interference frequency increases at the cost of decreasing contrast as the interrogation loop size grows. The magic lattice depth for different loop size is analytically calculated and shown in Fig. 6.3 (b), where the tolerance in depth fluctuation becomes stricter for a larger loop. The interferometer sensitivity, as defined by the interference frequency and/or the first order derivative of interferometry phase with respect to force $\partial\phi_{\mathrm{Int}}/\partial\mathcal{F}$, grows super-linearly, as it scales with the enclosed loop area. A larger loop size not only indicates a longer quasimomentum range, but also a higher mean quasienergy within the loop. It is to say that the increasing loop size represents the simultaneous growth in both temporal and spatial dimensions of the space-time diagram, resulting in a area-scaling sensitivity. One can imagine a significant extension of this work is to push much beyond the current sensitivity through multiple cycles of Bloch oscillations.

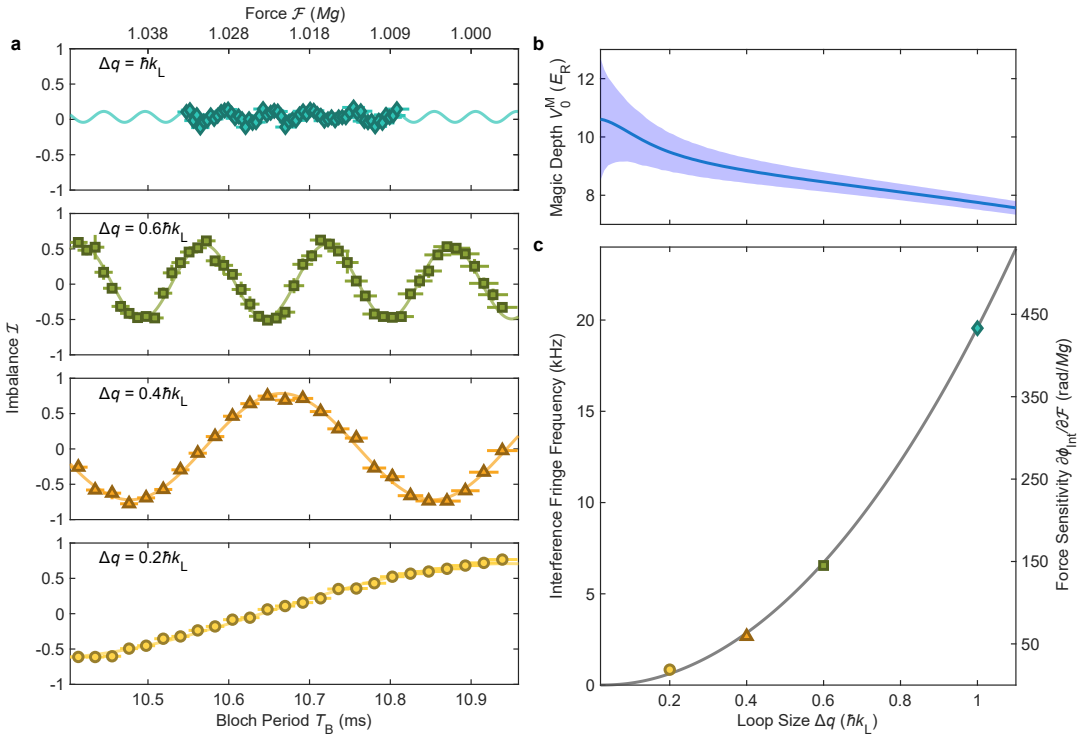

Figure 6.3: Interferometer sensitivity. **(a)** Interferometry force measurements with different loop sizes. From top to bottom are 1 $\hbar k_L$, 0.6 $\hbar k_L$, 0.4 $\hbar k_L$, and 0.2 $\hbar k_L$, respectively. The solid lines are sinusoidal fits on the experimental data. **(b)** Theoretical magic depth with respect to the loop size. The shaded area indicates the tolerance of lattice depth fluctuation at the magic condition. The maximum tolerance is defined as a $\pi/4$ shift in the interferometry phase. **(c)** The interferometer sensitivity as a function of loop size. The solid line is the analytical prediction and the scatter points represent fit results obtained from experimental data in (a).

6.5 Programmable Floquet Control

The flexibility of Floquet engineering allows us to design and characterize new Floquet-Bloch interferometry loops that provides higher sensitivity or new features.

In the previous sections, we have mostly implemented continuous modulation when the atoms are traversing the interferometer loop. However, as the loop size grows, the decrease of magic depth means that it is easier to excite atoms to higher bands through static Landau-Zener avoided crossings at the zone edge. There could also be unwanted one-photon or two-photon couplings to higher bands within the loop. To address this, we

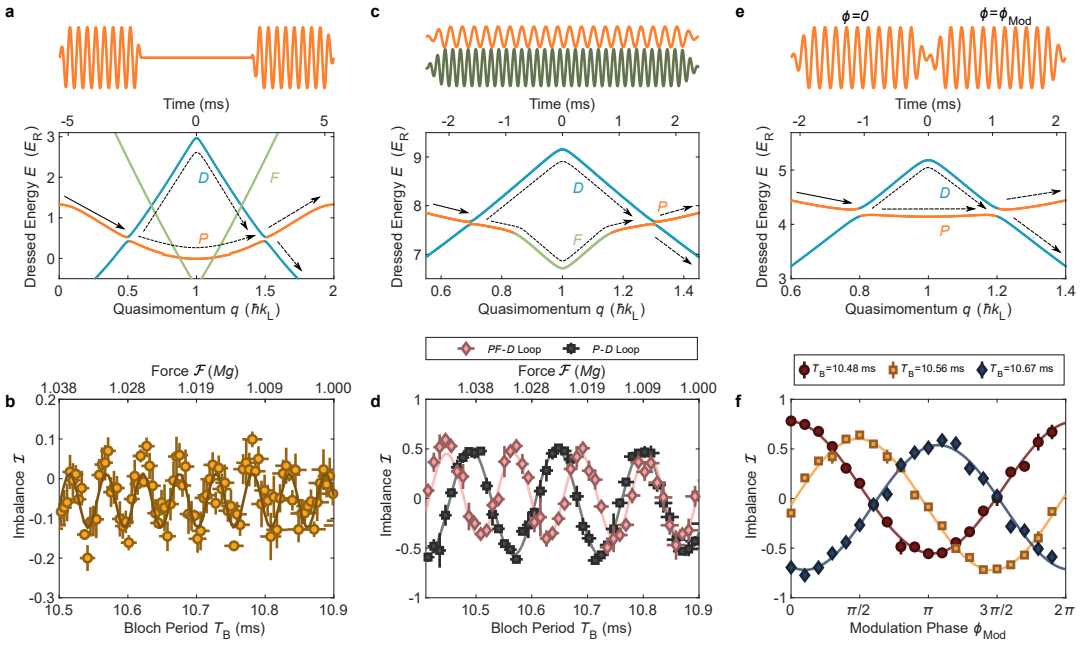

Figure 6.4: Programmable Floquet-Bloch Band Synthesis. **(a)** Pulsed scheme interferometry loop for avoiding unwanted F band coupling. **(b)** Force measurements from the temporally separated pulses. **(c)** Multi-band hybridized interferometry loop. Two continuous modulations hybridizes P and D bands as well as P and F bands within the $P-D$ loop. **(d)** Comparison of force measurements for the $PF-D$ and $P-D$ loops. **(e)** Modulation phase varying interferometry loop. Modulation for the two beamsplitters are separated with the phase ϕ_{Mod} of the second pulse being arbitrarily tuned relative to the first pulse. **(f)** Interferometry measurements of the modulation phase at three different forces.

employ a pulsed scheme where the modulation is only turned on for the Landua-Zener splittings to avoid, for example, undesired excitation to the F band (6.4 (a)). This preserves the interference fringes, as shown by force measurements in Fig. 6.4 (b).

In addition, we can apply more than one resonant modulation to hybridize multiple static Bloch bands. In Fig. 6.4 (c), a second drive is added to the original $\Delta q = 0.6\ \hbar k_L$ loop that hybridizes the P band with the F band. The resulting larger enclosed area enhances the interferometer sensitivity, as seen from the increase in interference frequency in Fig. 6.4 (d).

For the application of sensing a single, constant force, such as gravity, one can em-

ploy the pulsed scheme and scan the modulation phase of the second pulse relative to the first (Fig. 6.4 (e)). This results in a one-period fringe that depends on the relative modulation phase (Fig. 6.4 (f)). The overall interference phase offset depends on the absolute force strength, which can be tuned in an accelerated lattice scheme to reach maximal sensitivity.

6.6 Calibration

6.6.1 Lattice Depth

When the BEC is adiabatically transferred from the ODT to the optical lattice, it always remains in the ground state, resulting in a wavepacket in the S band centered at $q = 0$. Since each lattice depth corresponds to a different resonant coupling frequency between bands, we can utilize these transitions and their resonant frequencies to calibrate the lattice depth.

In this experiment, we choose the S and D bands because transitions are forbidden between bands of different parities, e.g., $S - P$ and $P - D$ at the zone center. In order to do this, a frequency sweep of fixed frequency range is applied to resonantly transfer the atoms from S band to D band (Fig. 6.5 (a)). The atom populations in each band are measured using band mapping. As shown in Fig. 6.5 (b), by varying the center sweep frequency, the population fraction in the D band changes. A gaussian fit is used to retrieve the center resonant frequency that corresponds to a fixed lattice depth. By performing frequency sweep measurements at different lattice power setpoints, and thus, lattice depths, we can construct a calibration curve that maps the power setpoint to the respective lattice depth (Fig. 6.5 (c)).

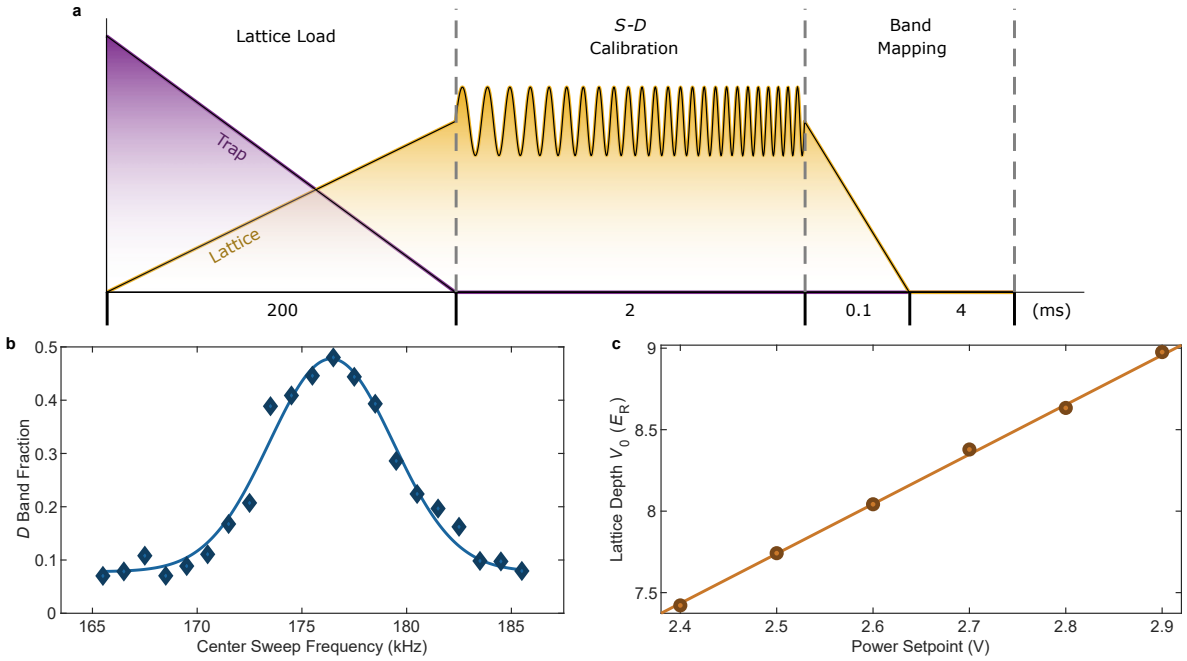

Figure 6.5: Lattice Depth Calibration. **(a)** Experimental sequence for the $S - D$ transfer lattice depth calibration. **(b)** The D band fraction as a function of the center sweep frequency used in $S - D$ calibration. The scattered points represent experimental fitted atom population fraction in D band after band mapping. The solid line is a Gaussian fit to locate the center resonant frequency. **(c)** Lattice depth with respect to the lattice laser power setpoint. Each experimental calibrated lattice depth (scatter point) corresponds to a center resonant frequency from the Gaussian fit in (b). The solid line is a linear fit for lattice depth calibration. Vertical error bars are uncertainties from the Gaussian fits.

6.6.2 Force

The Bloch frequency, and thus the force strength (Eqn. 2.57), can be experimentally measured by having the atoms undergoing multiple cycles of Bloch oscillation in the S band. For atoms in a deep lattice, $V_0 = 12.3\ E_R$ in our case, the momentum-trajectory is sawtooth like due to the nearly flat S band dispersion. By fitting a sawtooth wave to the atomic populations after band mapping, we can find the measured Bloch frequency for a specific force setpoint (Fig. 6.6 (a)). A calibration curve can be constructed through measurements of Bloch frequencies at different force setpoints, as shown in Fig. 6.6 (b).

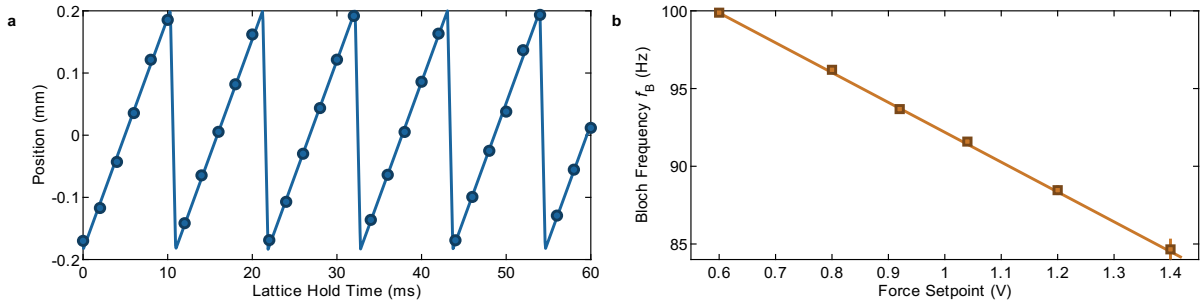

Figure 6.6: Force Calibration. **(a)** Fitted atomic positions after band mapping showing multiple periods of Bloch oscillations (scatter points). The solid curve is a sawtooth-wave fit to retrieve the Bloch frequency. **(b)** Bloch frequency with respect to the force setpoint. Each experimental calibrated Bloch frequency (scatter point) corresponds to a force setpoint used in the Bloch oscillations. The solid line is a linear fit for force calibration. Vertical error bars are uncertainties from the sawtooth fits.

6.6.3 Modulation Depth

In order to maximize the contrast for interferometry fringes, we experimentally optimize the beamsplitter's modulation strength to ensure that the Landau-Zener transition probability is 50%. By turning off the second beamsplitter pulse, we can measure the output port populations under the sole effect of the first beamsplitter. A scan of the modulation amplitude can reveal the amount drive strengh we need to achieve even splitting of two bands (Fig. 6.7)

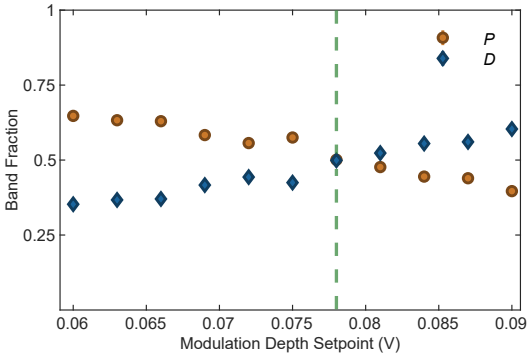

Figure 6.7: $P - D$ Modulation Depth Calibration. Fitted atomic population fraction in each band as a function of modulation depth for the first 50-50 Landau-Zener beamsplitter.

6.7 Active Stabilization

We implement several active stabilization systems for the interferometer measurements presented above.

- **Lattice Laser Power** We utilize an acousto-optic modulator (AOM) with a digital PID feedback loop to actively stabilize the laser power. A small fraction of the beam is screened by a beam sampler and sent to an InGaAs photodiode that converts optical power to a voltage. The photodiode voltage is first low-passed at a corner frequency of 10 kHz before being sent to the PID. The amplitude modulation waveform is generated by a function generator and combined with the PID output using a RF splitter. The combined signal goes to a RF synthesizer that provides RF signal to the AOM. The presence of the 10 kHz low-passed filter means that we correct only slow drift in lattice power but not the fast amplitude modulation (>100 kHz).

- **Lattice Laser Pointing** The optical lattice's position in the atom's plane for both incoming and retro reflected direction is actively stabilized with a commercial pointing stabilization system from MRC GmbH. The details are described in Section 4.2.

- **Push Coil Current** The current of the electromagnetic gradient responsible for Bloch oscillations are actively stabilized with an analog PID feedback loop. The details are discussed in Section 3.3.1.

6.8 Conclusion

In conclusion, we have described and experimentally demonstrated a simple, versatile, and extensible class of trapped matter-wave interferometers constructed from magic

Floquet-Bloch band structures in a modulated optical lattice. Key virtues of this approach include compactness, versatility, high ultimate sensitivity unlimited by device size, and intrinsic robustness against trap-induced dephasing and pulse errors. The $1/\mathcal{F}$ dependence of the interferometer phase offers enhanced force sensitivity in the weak-force regime, a feature that can be exploited in more generality by introducing an accelerated lattice to realize a frame transformation. The ultimate limits on the sensitivity of this technique remain to be explored. While in the experiments we present the coherence was limited by technical imperfections like residual magnetic field curvature and lattice beam mode quality, this can be straightforwardly improved in a variety of ways. Possible avenues for such improvements include using magnetically insensitive states or isotopes with intrinsically weak interactions [54], designing improved field control, and adding a resonant low-finesse cavity as a mode cleaner. While the use of a low-mass isotope like ^{7}Li is helpful for enabling large spatial separation, the technique could be expanded to heavier atoms by using higher-band transitions to generate higher momentum transfer. The flexibility, power, and large design parameter space offered by the Floquet engineering framework, along with the good match between interferometer performance and both numerical and analytical theory, should allow the use of optimal control and machine learning techniques to design more complex interferometer sequences for enhanced robustness and sensitivity.

Chapter 7

Quantum Many-Body Kapitza Pendulum

The Kapitza Pendulum is a well-known example in classical mechanics for exhibiting an unusual feature of dynamical stabilization under periodic driving. High-frequency modulation of the pendulum's pivot could lead to stable oscillatory behavior when the pendulum is inverted, avoiding the fate of chaos [55, 56]. Similar non-equilibrium phenomena have been investigated in the context of ultracold atoms, such as the kicked rotor model [57, 58], to explore their quantum nature and study new phases of quantum matter. Below is one potential realization of the quantum many-body Kapitza pendulum, using Bose-condensed lithium in dual strongly driven optical lattices. Past discussions about this idea can be found in Zachary, Kevin, and Cora's theses [8, 59, 10].

7.1 Dynamical Stabilization in Classical Kapitza Pendulum

Fig. 7.1 shows the setup of a classical Kapitza pendulum. Its pivot is modulated at an angular frequency ω and an amplitude A. When the modulation angular frequency is high compared to the natural angular frequency of the system, $\omega_0 = \sqrt{\frac{g}{l}}$, the pendulum can be stabilized around the inverted position $\theta = \pi$.

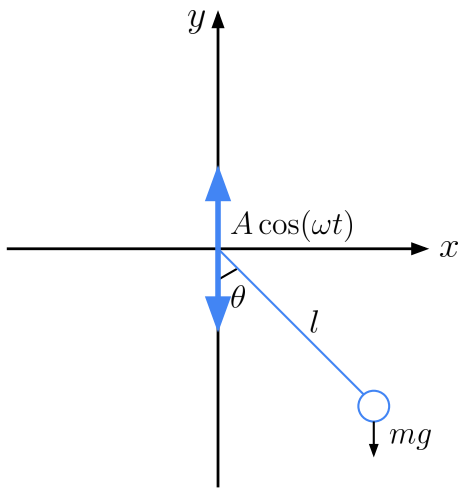

Figure 7.1: The classical Kapitza pendulum, with its pivot being modulated.

The positions of the pendulum are:

$$x = l\sin(\theta),\ \ y = -l\cos(\theta) + A\cos(\omega t) \tag{7.1}$$

Through this, we can construct a Lagrangian $\mathcal{L}$ for the system:

$$\begin{aligned}\mathcal{L} =& T - U \\ =& \frac{1}{2}m(\dot{x}^2 + \dot{y}^2) + mg\left[l\cos(\theta) - A\cos(\omega t)\right] \\ =& \frac{m}{2}\left[l^2\dot{\theta}^2 - 2l\dot{\theta}A\omega\sin(\theta)sin(\omega t) + A^2\omega^2\sin^2(\omega t)\right] + mg\left[l\cos(\theta) - A\cos(\omega t)\right]\end{aligned} \tag{7.2}$$

Subsituting this into the Euler-Lagrangian equation, we obtain the equation of motion:

$$\ddot{\theta} + \sin(\theta)\left[\frac{g}{l} - \frac{A}{l}\omega^2\cos(\omega t)\right] = 0 \tag{7.3}$$

We can see that at the absence of modulation, Eqn. 7.3 becomes the simple pendulum's equation of motion whose two equilibrium positions are $\theta_0 = 0$ (stable) and $\theta_0 = \pi$ (unstable). Eqn. 7.3 also has the form of Mathieu's equation under small angle approximation. To show that, we can write it in terms of the following dimensionless parameters:

$$\tau \equiv \omega t \tag{7.4}$$

$$\Omega \equiv \frac{\omega}{\omega_0},\ \omega_0 = \sqrt{\frac{g}{l}} \tag{7.5}$$

$$\alpha \equiv \frac{A}{l} \tag{7.6}$$

the equation of motion becomes:

$$\frac{d^2\theta}{d\tau^2} + \left[\frac{1}{\Omega^2} - \alpha\cos(\tau)\right]\sin(\theta) = 0 \tag{7.7}$$

Taylor expanding the equation around the equilibria $\theta_0 = 0$ and $\theta_0 = \pi$, we obtain:

$$\theta = \theta_0 + \tilde{\theta} \tag{7.8}$$

$$\frac{d^2\tilde{\theta}}{d\tau^2} \pm \left[\frac{1}{\Omega^2} - \alpha\cos(\tau)\right]\tilde{\theta} = 0 \tag{7.9}$$

with the "+" case and "-" cases corresponding to small fluctuations $\tilde{\theta}$ around $\theta_0 = 0$ and $\theta_0 = \pi$, respectively. The Mathieu's equation is given by:

$$\frac{d^2x}{d\tau^2} + [\delta + \epsilon\cos(\tau)]\, x = 0 \tag{7.10}$$

Comparing Eqn. 7.9 and Eqn. 7.10, we can see that $\delta > 0$ represents the "+" case for the non-inverted position $\theta_0 = 0$, and $\delta < 0$ represents the "-" case for the inverted position $\theta_0 = \pi$. Fig. 7.2 shows the stability of the solutions to Mathieu's equation, in which "S" means stable and "U" unstable. As we can see, when $\delta < 0$ and $\epsilon > 0$, there is a region where the solutions are stable. Physically, it means that under periodic driving ($\alpha > 0$), the pendulum can oscillate around the inverted position $\theta_0 = \pi$, a demonstration of the dynamical stabilization when the pivot is being modulated.

The physical intuition behind such a stability under periodic driving is provided by Kapitza and covered by Landau in his book [55]. The motions of the system are separated into two parts, slow and fast, with the equation of motion being:

$$m\ddot{x} = -\frac{dV_0(x)}{dx} + f(x,\ t),\ \ f(x,\ t) = f(x,\ t + \frac{2\pi}{\omega}) \tag{7.11}$$

where the total force consists of the gradient of a time-independent potential $V_0(x)$ and a time-periodic force $f(x,\ t)$ with an angular frequency ω. The ansatz $x(t)$ is then written

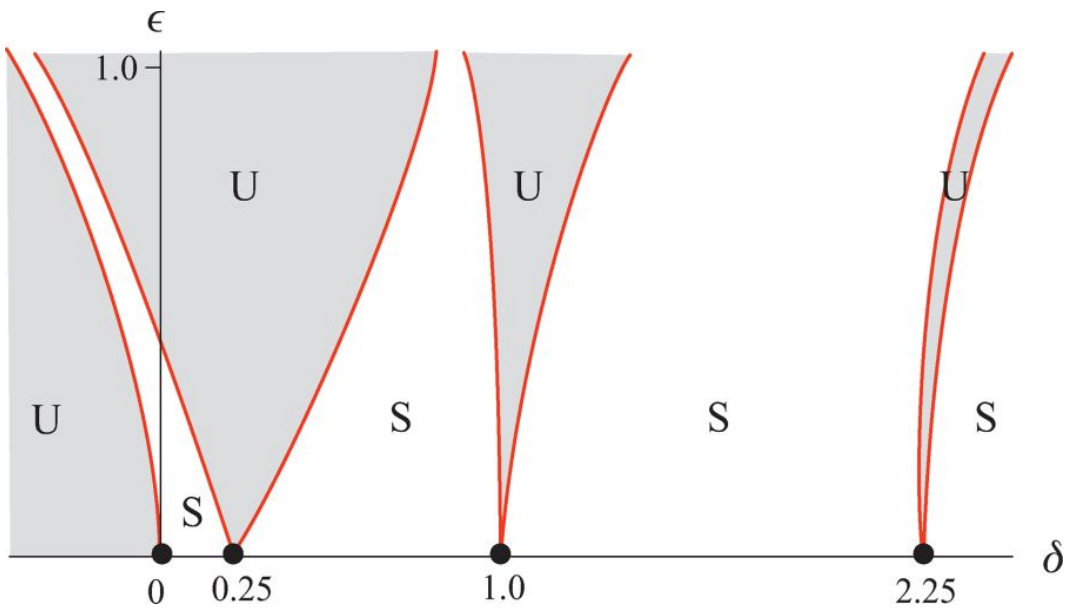

Figure 7.2: The stability of the solutions to Mathieu's equation, retrieved from [60]. The shaded regions with "U" are the unstable cases, whereas the regions labeled with "S" are the stable cases.

as the sum of a slow variation term $X(t)$ and a fast fluctuation term $\xi(t)$.

$$x(t) = X(t) + \xi(t) \tag{7.12}$$

To zero-th order, we have:

$$m\ddot{\xi} = f(x,\ t) \tag{7.13}$$

$$\rightarrow \xi = -\frac{f}{m\omega^2} \tag{7.14}$$

since both ξ and f have the same angular drive frequency ω. To first order in ξ, one obtains:

$$m(\ddot{X} + \ddot{\xi}) = -\frac{dV_0(X)}{dX} - \xi\frac{d^2V_0(X)}{dX} + f(X,\ t) + \xi\frac{\partial f(X,\ t)}{\partial X} \tag{7.15}$$

Because both ξ and f are fast fluctuation in time with zero mean ($\overline{\xi} = 0$, $\overline{f} = 0$), the time average of Eqn. 7.15 gives:

$$m(\overline{\ddot{X} + \ddot{\xi}}) = -\frac{dV_0(X)}{dX} - \overline{\xi}\frac{d^2V_0(X)}{dX} + \overline{f(X,\ t)} + \overline{\xi\frac{\partial f(X,\ t)}{\partial X}} \tag{7.16}$$

$$m\overline{\ddot{X}} = -\frac{dV_0(X)}{dX} + \overline{\xi\frac{\partial f(X,\ t)}{\partial X}} \tag{7.17}$$

Using Eqn. 7.14, it yields:

$$\begin{aligned} m\overline{\ddot{X}} &= -\frac{dV_0(X)}{dX} - \frac{1}{m\omega^2}\overline{f\frac{\partial f(X,\ t)}{\partial X}} \\ &= -\frac{dV_{\text{eff}}}{dX},\ V_{\text{eff}} = V_0 + \frac{\overline{f^2}}{2m\omega^2} = V_0 + \frac{1}{2}m\omega^2\overline{\xi^2} \end{aligned} \tag{7.18}$$

Therefore, to first order, the motion of the system can be captured by the time-averaged, effective potential V_{eff}. For the Kapitza pendulum, the effective potential leads to bifurcation of the original potential maximum $V(\theta = \pi)$, and turns it into a small harmonic confinement around $\theta = \pi$. Therefore, the system can undergo stable oscillations around such a time-averaged harmonic potential.

7.2 Classical Equivalence of Strongly Driven Optical Lattices

The Hamiltonian for an amplitude modulated optical lattice is given by:

$$H = \frac{p^2}{2m} - V_0\left[1 + \alpha\sin(\omega_D t)\right]\cos^2(k_L x) \tag{7.19}$$

Substituting it into the Hamilton's equation, we can obtain the classical equation of motion:

$$m\ddot{x} = -V_0 k_L \left[1 + \alpha \sin(\omega t)\right] \sin(2k_L x) \tag{7.20}$$

When there is no modulation ($\alpha = 0$), we can solve for the natural angular frequency ω_0 of the system under the small angle approximation:

$$w_0 = \sqrt{\frac{2V_0 k_L^2}{m}} \tag{7.21}$$

Expressing Eqn. 7.20 under the small angle approximation and using dimensionless variables:

$$\tau \equiv \omega_D t \tag{7.22}$$

$$\Omega \equiv \frac{\omega_D}{\omega_0} \tag{7.23}$$

$$\phi = k_L x \tag{7.24}$$

we have:

$$\frac{d^2\phi}{d\tau^2} + \frac{1}{\Omega^2}\left[1 + \alpha \sin(\tau)\right]\phi = 0 \tag{7.25}$$

which is also equivalent to the Mathieu's equation as Eqn. 7.9 does. This establishes the correspondence between the Kapitza pendulum and the classical optical lattice. However, the amplitude α in Eqn. 7.25 is scaled down by a factor of Ω^2, so now we need a much stronger drive strength (above unity) to achieve similar dynamical stabilization.

Fig. 7.3 shows the phase diagram of the classical amplitude modulated optical lattice with the initial position $\phi_0 = \pi$. The escape velocity is the critical initial velocity above which the system can escape from the original lattice site. A positive escape velocity means that the system is stable around $\phi = \pi$, since it requires a finite amount of

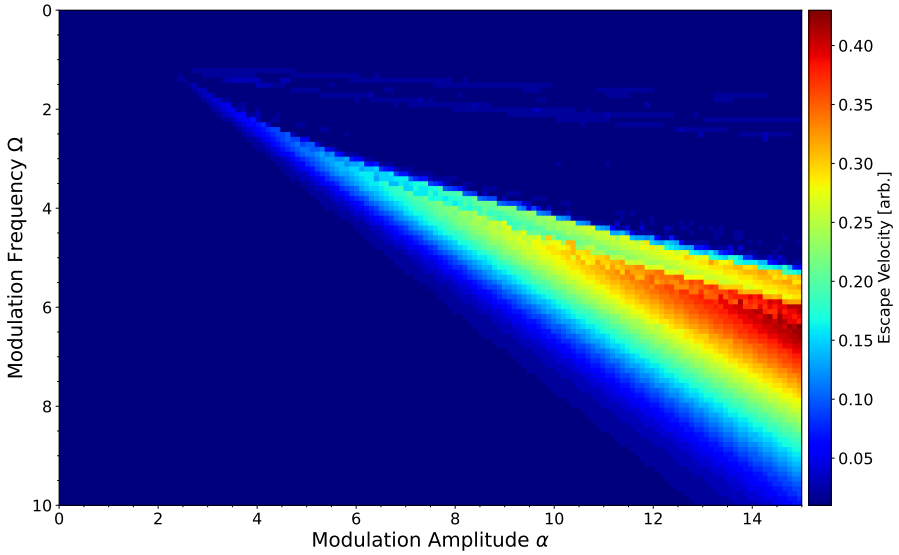

Figure 7.3: Phase diagram of the classical amplitude modulated optical lattice at $\phi = \pi$, obtained through numerical solutions to Eqn. 7.20. The color bar represents the escape velocity, the initial velocity above which the particle escapes from the original lattice site. A positive escape velocity indicates a positive binding energy and that the system is in a stable equilibrium. Results are independently replicated from [10]

kinetic energy to escape. Therefore, under strong, high-frequency driving, the amplitude modulated lattice also exhibits dynamical stabilization at the inverted position, like that of the Kapitza pendulum. In the region above the dynamical stabilized regime in the phase diagram, the particle goes through chaotic motion and the system is non-integrable.

7.2.1 Double Optical Lattices

One way to achieve amplitude modulation greater than 100% is to use two co-linear lattices with orthogonal linear polarizations, as illustrated in [59]. The two lattices have

the potential form of:

$$
\begin{aligned}
V_1(x,\ t) &= -\frac{\alpha}{2}V_0\left[1+\cos(\omega_D t)\right]\cos^2(k_L x) && (7.26)\\
&= -\alpha V_0 \sin^2(\frac{\omega_D t}{2}+\frac{\pi}{2})\cos^2(k_L x) && (7.27)\\
V_2(x,\ t) &= -\frac{2+\alpha}{2}V_0\left[1-\frac{\alpha}{2+\alpha}\cos(\omega_D t)\right]\cos^2(k_L x+2\frac{\pi}{4}) && (7.28)\\
&= -V_0\left[1+\alpha\sin^2(\frac{\omega_D t}{2})\right]\cos^2(k_L x+2\frac{\pi}{4}) && (7.29)
\end{aligned}
$$

The total potential is:

$$
\begin{aligned}
V_{\text{total}}(x,\ t) &= V_1(x,\ t)+V_2(x,\ t)\\
&= -\frac{1+\alpha}{2}V_0-\frac{V_0}{2}\left[1+\alpha\cos(\omega_D t)\right]\cos(2k_L x)
\end{aligned}
\qquad (7.30)
$$

The time-averaged effective potential in Eqn. 7.18 in this case is:

$$
V_{\text{eff}}(x) = -\frac{1+\alpha}{2}V_0-\frac{1}{2}V_0\cos(2k_L x)+\frac{1}{8}\left(\frac{\alpha}{\Omega}\right)^2 V_0\sin^2(2k_L x) \qquad (7.31)
$$

Fig. 7.18 shows the waveform of the effective potential, neglecting the modulation amplitude dependent offset. The lattice depth is $V_0 = 10\ E_R$ and the modulation angular frequency is $\Omega = 6$. It is important to note that here the dimensionless angular frequency is defined as the ratio of the drive angular frequency ω_D and the natural angular frequency ω_0, not the recoil angular frequency ω_R. As we can see, as the modulation amplitude increases, the local harmonic trap depth around the static potential maximum becomes larger. The particle would execute periodic oscillations and be dynamically stabilized at the static potential maximum.

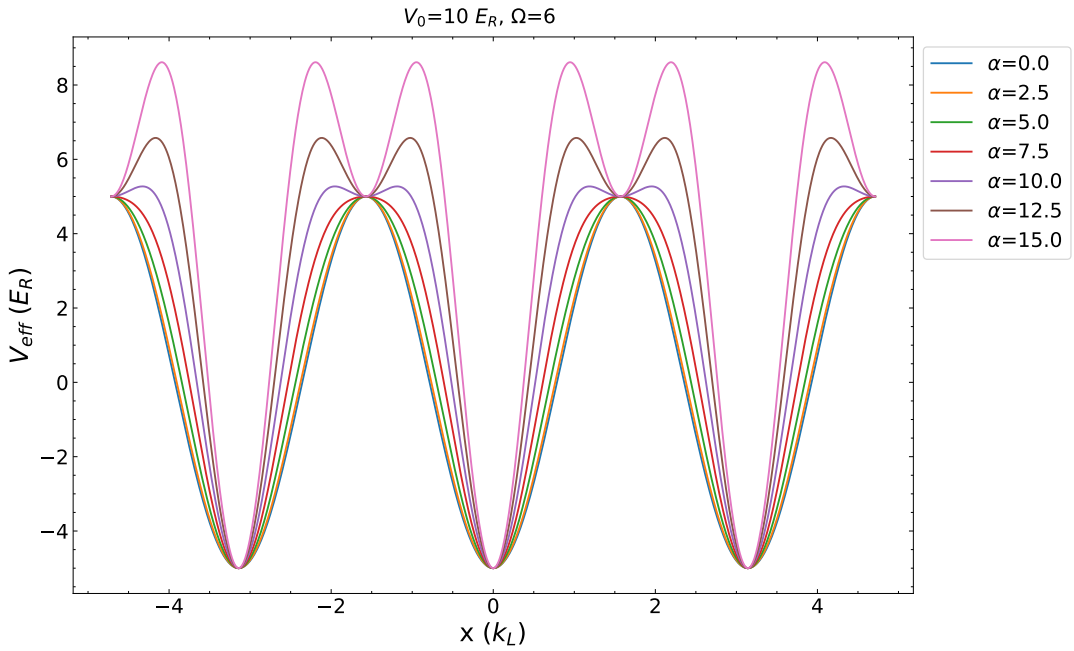

Figure 7.4: The time-averaged effective potential for the dual optical lattices, with a total lattice depth $V_0 = 10\ E_R$ and a normalized modulation angular frequency $\Omega \equiv \frac{\omega_D}{\omega_0} = 6$. Different modulation amplitudes α are shown. The local harmonic confinement around the static potential maximum becomes stronger as the modulation amplitude increases.

7.3 Quantum Simulation of Interacting Kapitza Pendulum

The main focus of using a quantum simulator to study the optical lattice equivalence of the Kapitza pendulum concerns the transition from a classical model to a quantum mechanical system. How do the dynamics change when the object of interest is no longer a classical particle with definite position and momentum, but rather a quantum state? In addition, the long coherence time of cold atom experiments allows the system to undergo a long-time evolution, giving us the opportunity to detect ergodicity-breaking phenomena like pre-thermal plateau for ultrastrong and ultrafast driven quantum matter.

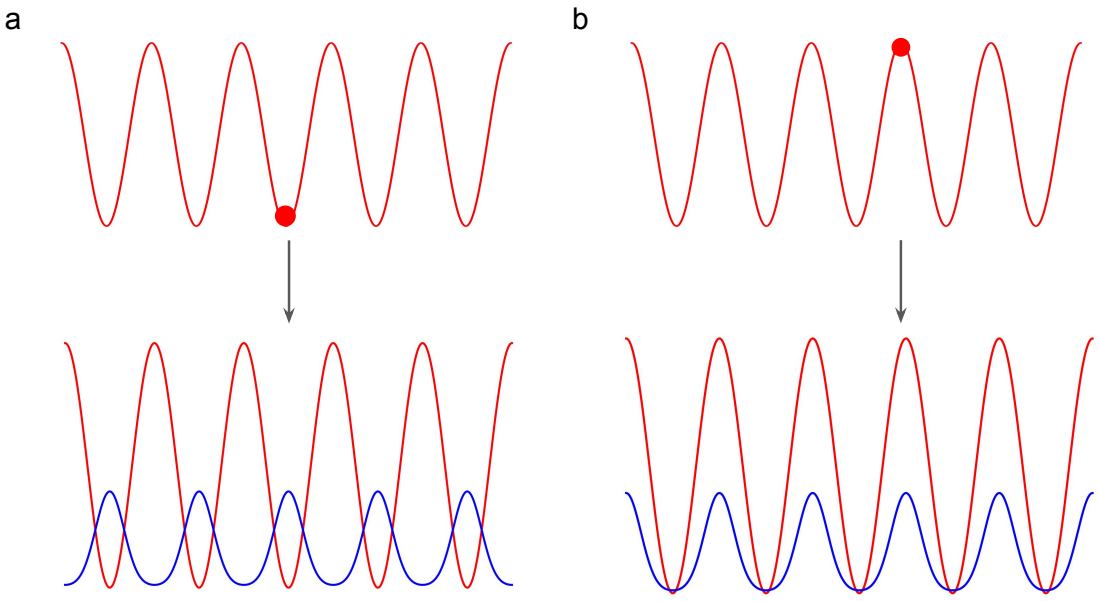

Figure 7.5: The change in the initial state from classical lattice to quantum mechanical counterpart. (a) When classically the particle sits at the static potential minimum, the initial wavefunction in quantum mechanics has the largest probability density at the static potential minima across all lattice sites, specifically the Bloch state $\psi_{00}(x)$ is used here for visualization. (b) When classically the particle is placed inverted in the static potential maximum, the initial wavefunction in quantum mechanics has the largest probability density at the static potential maxima across all lattice sites, specifically the Bloch state $\psi_{00}(x)$ shifted by one half of the lattice spacing is used here for visualization. The blue curves represent the probability density of the wavefunction $|\psi(x)|^2$.

The Hamiltonian for the dual amplitude modulated optical lattices is given by:

$$H = \frac{p^2}{2m} - \frac{1}{2}V_0\left[1 + \alpha\cos(\omega_D t)\right]\cos(2k_L x) \tag{7.32}$$

where the modulation amplitude dependent offset can be neglected. In the single-particle case, the dynamics is governed by the time-dependent Schrodinger equation. As shown in Fig. 7.5, the well-defined initial position of a classical particle is replaced by the probability density of the initial wavefunction of the quantum particle. The initial quantum state can be localized at the static potential minima or maxima. This can be achieved

by loading the BEC into one of the two undriven lattices, and then quenching the system through simultaneously turning on the second lattice as well as the amplitude modulation for both lattices. We can define the density correlation $C(t)$ at time t as:

$$C(t) = \int_{-\infty}^{\infty} |\psi(x,\ t)|^2 |\psi(x,\ 0)|^2 dx \tag{7.33}$$

This is a way to quantify the likelihood of the quantum particle having the largest probability density at the static potential maxima, in analogue to the likelihood the classical particle staying at one of the static potential maxima. The time-averaged temporal density correlation $\overline{C(T)C(0)}$ is defined as:

$$\overline{C(T)C(0)} = \lim_{\tau\to\infty} \frac{1}{\tau} \int_0^{\tau} C(t+T)C(t)dt \tag{7.34}$$

It represents the time-averaged likelihood of the quantum particle staying at the static potential maxima after a modulation cycle T.

Fig. 7.6 shows the phase diagram of the quantum Kapitza pendulum initialized by the Bloch state $\psi_{00}(x)$ shifted to localize at the static potential maxima. The results are obtained through numerical propagation of the time-dependent Schrodinger equation. As we can see from the time-averaged temporal density correlation after 900 cycles of modulation, the diagram can be roughly divided into three regions: a, b, and c.

Region b demonstrates nearly perfect temporal density correlation, supporting the feature of dynamical stabilization for the quantum counterpart of the classical Kapitza pendulum. If the particle is initially prepared to localize simultaneously in the lattice minima and maxima, this dynamically stabilized phase effectively reduces the lattice constant by half. A continuous sweep of the modulation parameters could lead to zero, one, or two stable dynamical equilibrium positions in a single lattice site.

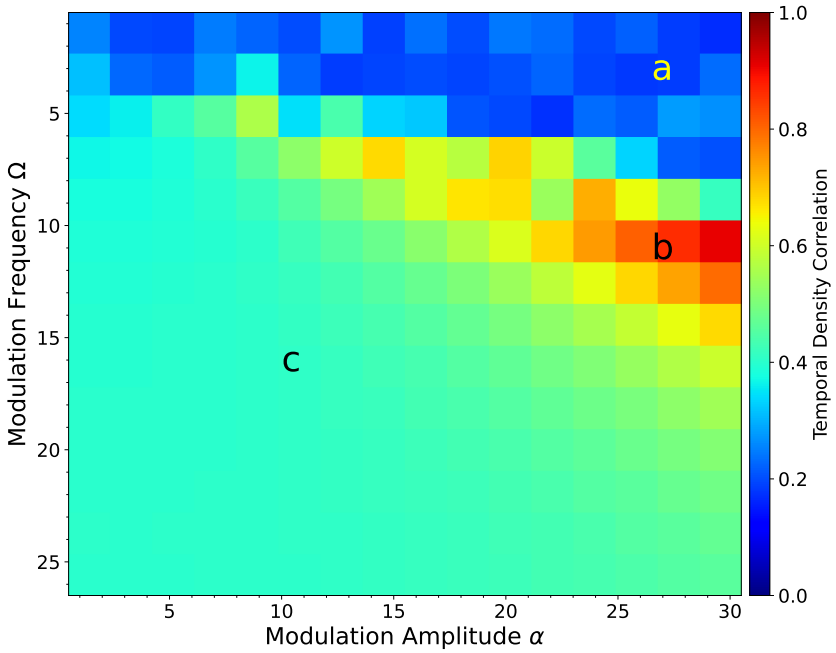

Figure 7.6: Phase diagram of the quantum Kapitza pendulum, obtained through numerical prorogation of the time-dependent Schrodinger equation. The initial state is the Bloch state $\psi_{00}(x)$ at the static potential maxima (inverted case). The colorbar indicates the time average of the temporal density correlation, as defined in Eqn. 7.34. The lattice depth is 16 E_R and the total propagation time is 900 modulation cycles. Letters a, b, and c are used to represent different regions of the phase diagram.

Region a represents the chaotic regime in the classical phase diagram. Based on the correspondence principle, quantum systems should recover the same classical dynamics as they approach the classical limit, even for chaotic systems. However, the emerging chaotic motion of a quantum system has been surprising to many, as it is prohibited by the linearity of the Schrodinger equation. To-date, the definition of quantum chaos remains controversial. Past studies even revealed that the chaotic nature of a quantum system is embedded in the spectrum of its Hamiltonian, where the initial conditions play a very small role, as opposed to its emphasis in classical configurations [61]. Quantum chaos is also deeply related to thermalization of non-integrable systems and the eigenstate thermalization hypothesis [62, 63]. Given the low temporal density correlation in region a of the phase diagram in Fig. 1, and the chaotic nature of the classical Kapitza pendulum,

certain driving parameters could lead to a new way to generate quantum chaos despite the absence of interaction. More discussion on quantum chaos can be found in Appendix A.

Region c shows partial temporal density correlation, but insufficient for dynamical stabilization. It is at an area in between region a and region b, which worth further examinations both numerically and experimentally to better understand this phase.

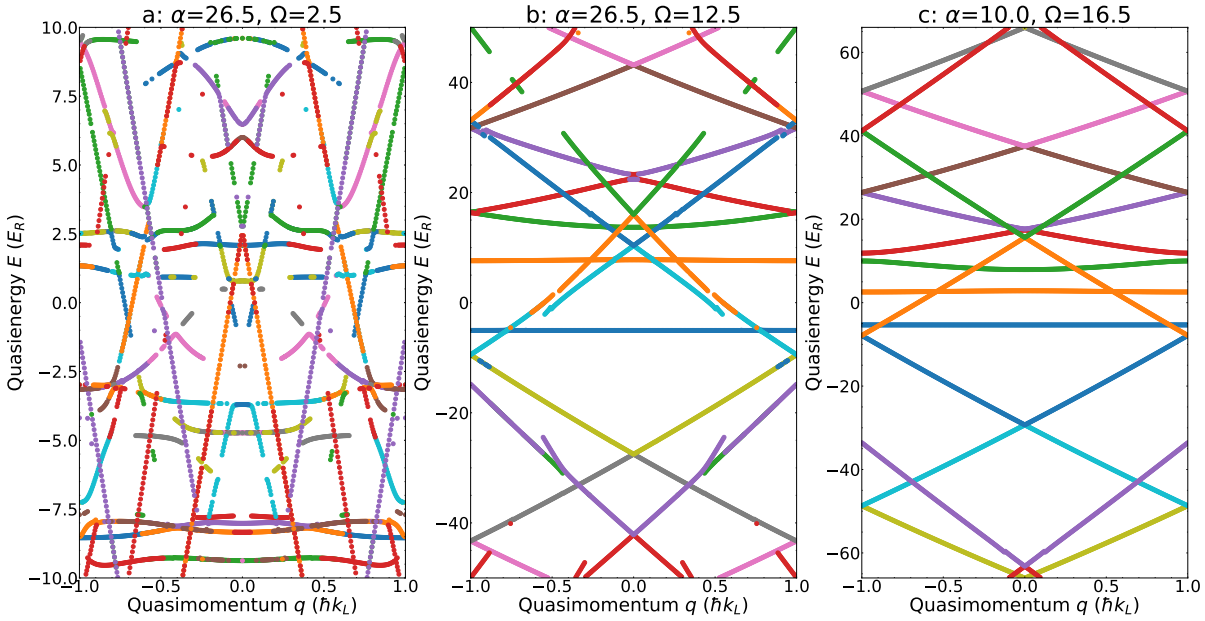

Figure 7.7: Floquet-Bloch band structures for one point in each of the regions labeled in Fig. 7.6. 301 static bands were used to calculate the band structures, with 15 static band components displayed.

Fig. 7.7 demonstrates the Floquet-Bloch band structure for one set of drive parameters in each region of the phase diagram. It is clear that region a contains a much more unusual spectrum than region b and region c, which yields an extra potential evidence for quantum chaos. Since only 15 static band components are displayed, the large amount of discontinuities usually indicates that more higher bands need to be accounted for in the spectrum for hybridization. It means that this single-particle system can be easily driven into very highly excited states. Further quantification methods should be carried

out to understand the spectral statistic, such as the spectral form factor and the nearest neighbor level spacing [61, 64, 65]. Out-of-time-correlator (OTOC) can also be evaluated in position space to as a potential way to characterize quantum chaos [66].

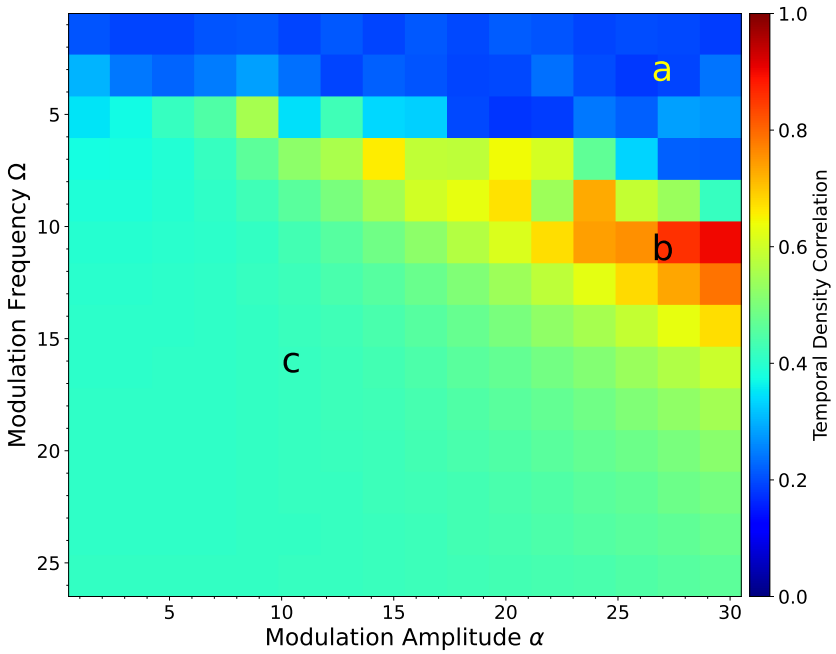

Figure 7.8: Phase diagram of the interacting quantum Kapitza pendulum, obtained through numerical prorogation of the time-dependent Gross-Pitaevskii equation. The initial state is the ground state retrieved from imaginary time prorogation, and shifted by half lattice spacing to localize at the static potential maxima (inverted case). The colorbar indicates the time average of the temporal density correlation. The lattice depth is 16 E_R, the scattering length is 240 a_0, and the lattice beam waist is assumed to be 80 μm. Total propagation time is 900 modulation cycles. Letters a, b, and c are used to represent different regions of the phase diagram.

Fig. 7.8 shows the phase diagram of the interacting Kapitza pendulum with a scattering length of 240 a_0. The initial states were the ground state of the system, found through imaginary time propagating the Thomas-Fermi approximation. The results are highly similar to the non-interacting case in Fig. 7.6. The temporal density correlation remains highly consistent throughout the phase diagram. Here I will summarize a few numerical observations or comments that are not included in the discussions above, and worth future explorations:

- If the initial wavefunction is the ground state multiplied by a Gaussian envelope, one would see decay of the density correlation in time for both TDSE and GPE results. This is physically reasonable, as it accounts for finite quasimomentum width, and the excitation channels increases through quenching. For the non-interacting case, dynamical stabilization still exists with the presence of the gaussian envelope. However, the interacting case at 240 a_0 has a much larger decay rate, with the time-averaged temporal density correlation being much smaller at the end of the 900 modulation cycles. The dynamical stabilization seems to break down at this interaction strength. The similarity between the TDSE and GPE results is that the time-averaged temporal density correlation remains the lowest in the entire phase diagram. It is not impossible that the single-particle system driven with parameters in region a already exhibits thermalization (and quantum chaos) without the necessity of introducing interaction.

- Fourier space time propagation was also carried out to benchmark the TDSE phase diagram, without concerning boundary effect in real-space simulation. The results are mostly consistent with the real-space time-splitting spectral methods.

- In the simuation above, I have been using the observable, time-averaged temporal density correlation, defined in Eqn. 7.34. However, it would be difficult in experiment to measure such quantity, as it requires a large datacube nearly impossible to obtain with our experimental sequence duration. Possible experimental detection techniques include

  - Inverse Participation Ratio (IPR): it is a quantitative measure for localization and for the absence of heating.

  - Band Mapping: one can perform a quench off at the end of the evolution,

projecting the final state into the static Bloch state basis. Then, band mapping can be used to readout the measurement in the static Bloch band space.

– Quantum Gas Magnifier [67, 68]: this technique allows us to have single-site resolution readout using standard absorption imaging. The working principle is to turn on a harmonic trap at the end of the experimental sequence for a quarter of the total harmonic trap period. It converts all the spatial information of the system into its momenta, which can be easily revealed by a time of flight free expansion. Single-site images can directly demonstrate dynamical stabilization as we would see the probability density localized at the static potential maxima.

The realization of a quantum Kapitza pendulum will bring new understanding of highly controllable Floquet phases of matter. This could serve as one of the simplest models that exhibit quantum chaos, providing an experimental testbed for various theoretical predictions. It also opens a new frontier for studying thermalization of an isolated quantum many-body system under strong, non-perturbative driving.

Appendix A

Quantum Chaos and Thermalization

In classical mechanics, the concept of thermalization is deeply related to ergodicity and therefore to dynamical chaos. A classical system is said to be thermalized if the long-time average of a measurement is equal to the ensemble average described by equilibrium statistical mechanics [62]. This can be explained by the ergodic hypothesis. It states that an ergodic system would explore every region of the phase space over sufficiently long time, and that the time spent in each region is proportional to its volume [69]. Therefore, each microstate is equally probable, and the system can be described using the microcanonical ensemble.

Since the hypothesis is conditioned upon the fact that the system reaches the entire phase space, integrability plays a crucial role. Only systems that are non-integrable, when the number of independent conserved quantities is less than the number of degrees of freedom, have a uniform probability to cover the phase space. An integrable system has periodic/quasi-periodic phase space trajectories and thus fails to meet such an requirement. Non-integrability is a necessary, and often sufficient, condition for a system to manifest dynamically chaotic behavior [62]. Broadly speaking, a classical integrable system with no chaotic behavior would not thermalize, with certain exceptions, notably

the Fermi-Pasta-Ulam-Tsingou problem [70].

Quantum mechanics provides an alternative language for many-body physics at the microscopic level, where the individual constituents do not have a well-defined position and momentum. Instead, the description of a quantum system is built upon its quantized energies and wavefunctions. In particular, the notion of phase space is no longer applicable and so are many ideas used to characterize dynamical chaos in classical phase space. Therefore, one might naively ask how these changes in fundamental framework from particle-nature to wave-nature of a system would lead to surprising phenomena in chaos and thermalization.

In this appendix, we will discuss chaos and thermalization in the context of quantum many-body physics, with a heavy emphasis on random matrix theory (RMT). More specifically, we will (i) review basic notions of RMT, such as Wigner-Dyson statistics and universality; (ii) introduce quantum chaos and analyze a measure known as the spectral form factor with its relevant time scales, namely the Thouless time and the Heisenberg time; and (iii) review quantum thermalization with concepts of the Eigenstate Thermalization Hypothesis (ETH) and entanglement entropy.

A.1 Random Matrix Theory

Random matrix theory (RMT) concerns the study of statistical properties of random matrices, whose entries are independently and randomly sampled from a probability distribution [61, 71]. As we will see later, this theory is particularly important for our understandings of quantum chaos and thermalization [62, 72]. In this section, we will mainly focus on basic notions of RMT with minimal connections to physics.

A.1.1 Gaussian Ensembles

Consider a $N \times N$ Hermitian matrix H, we can define a probability density $P(H)$ with the following normalization condition of $\int dH P(H) = 1$. It represents the product of individual probability density for every real parameter needed to specify this random matrix H. The probability density $P(H)$ can be obtained by demanding (1) invariance of $P(H)$ under a certain group of canonical transformations and (2) complete statistical independence of all matrix elements. In Wigner-Dyson statistics, three groups of canonical transformations are considered: orthogonal, unitary, and symplectic transformations. It can be shown that under the above transformations, $P(H)$ takes the form of [61]:

$$P(H) = Ce^{-A\mathrm{Tr}(H^2)} \tag{A.1}$$

with an arbitrary dimensions of N. Because of the Gaussian form of $P(H)$, each ensemble of random matrices associated with their corresponding canonical transformation is known as: Gaussian orthogonal ensemble (GOE), Gaussian unitary ensemble (GUE), and Gaussian symplectic ensemble (GSE), respectively. A derivation of the form of $P(H)$ for a GOE of 2×2 real, symmetric matrices is included in below.

In the eigen-basis of these Wigner-Dyson ensembles, where the matrices are diagonal, it can be shown that the probability density of the eigenvalues is [61]:

$$P(E_1, ..., E_N) \propto \left(\prod_{\mu<\nu}^{1...N} |E_\mu - E\nu|^\beta \right) \exp\left(-A \sum_{\mu=1}^{N} E_{mu}^2 \right) \tag{A.2}$$

$$\beta = \begin{cases} 1, & \text{GOE} \\ 2, & \text{GUE} \\ 4, & \text{GSE} \end{cases}$$

Suppose we have a random Hermitian matrix O, admitting the following spectral decomposition:

$$O = \sum_i O_i \left|i\right\rangle \left\langle i\right| \tag{A.3}$$

where $|i\rangle$ is the i-th eigenvector with the respective eigenvalue O_i. For another given random Hermitian matrix H, for which the eigenvectors are denoted by $|m\rangle$ and $|n\rangle$, the matrix element of O in the eigen-basis of H can be expressed as:

$$\begin{aligned} O_{mn} \equiv & \quad \left\langle m\right| O \left|n\right\rangle & \text{(A.4)} \\ = & \quad \sum_i O_i \left\langle m|i\right\rangle \left\langle i|n\right\rangle & \text{(A.5)} \\ = & \quad \sum_i O_i (\psi_i^m)^* \psi_i^n & \text{(A.6)} \end{aligned}$$

where $\psi_i^m \equiv \langle i|m\rangle$. Because the eigenvector of random matrices are random orthogonal unit vectors, to leading order in $\frac{1}{N}$, we have

$$\overline{(\psi_n^m)^*(\psi_j^n)} = \frac{1}{N}\delta_{mn}\delta_{ij} \tag{A.7}$$

with N being the dimension of the vector space. The matrix element of O can then be approximated, to leading order in $\frac{1}{N}$, as

$$O_{mn} \approx \overline{O}\delta_{mn} + \sqrt{\frac{\overline{O^2}}{N}} R_{mn} \tag{A.8}$$

where $\overline{O} \equiv \frac{1}{N}\sum_i O_i$ and R_{mn} is a random variable with zero mean and unit variance.

A.1.1.1 Probability Density of the GOE of 2×2 random Hermitian matrices

For a Gaussian orthogonal ensemble, we consider real, symmetric matrices with the orthogonal group for the canonical transformations [61]. Here, we take the dimension

of the matrices to be 2×2. Since H is real and symmetric, only three real parameters are needed to specify the matrix, H_{11}, H_{22}, and H_{12}. The probability density $P(H)$ is normalized as:

$$\int dH P(H) = \int dH_{11} dH_{22} dH_{12} P(H) = 1 \tag{A.9}$$

Two requirements to determine $P(H)$ are (1) it must be invariant under the orthogonal transformation,

$$dH P(H) = dH' P(H'),\ H' = OHO^{-1} \tag{A.10}$$

and (2) the three real parameters must be uncorrelated, so

$$P(H) = P_{11}(H_{11}) P_{22}(H_{22}) P_{12}(H_{12}) \tag{A.11}$$

If we consider a change of basis matrix with an infinitesimal change:

$$O = \begin{pmatrix} 1 & -\Theta \\ \Theta & 1 \end{pmatrix} \tag{A.12}$$

Requiring the invariance of $P(H)$ would yield:

$$\begin{aligned} P(H) = P(H) \Bigg\{ 1 - \Theta \Bigg[& 2H_{12} \frac{d \ln P_{11}}{dH_{11}} - 2H_{12} \frac{d \ln P_{22}}{dH_{22}} \\ & - (H_{11} - H_{22}) \frac{d \ln P_{12}}{dH_{12}} \Bigg] \Bigg\} \end{aligned} \tag{A.13}$$

The terms inside the square bracket must vanish, solving for the solution would give us:

$$\begin{aligned} P(H) &= C \exp\Big[- A\left(H_{11}^2 + H_{22}^2 + 2H_{12}^2\right) \\ &\quad - B\left(H_{11} + H_{22}\right)\Big] \\ &\cong C e^{-A\mathrm{Tr}(H^2)} \end{aligned} \tag{A.14}$$

The second equality is held true after choosing an appropriate offset.

A.1.2 Universality

Universality classes emerge in RMT, and specifically, Wigner-Dyson statistics because of the different types of canonical transformations mentioned above [61]. This becomes clear when one looks at the distribution of the nearest-neighbor level spacings of the eigenvalues $P(S)$, where S is defined as the difference between two neighboring eigenvalues normalized by the mean level spacing. The analytical form of $P(S)$ for the Gaussian ensembles is:

$$P(S) = \begin{cases} \frac{S\pi}{2} e^{-\frac{S^2\pi}{4}}, & \text{GOE} \\ \frac{S^2 32}{\pi^2} e^{-\frac{S^2 4}{\pi}}, & \text{GUE} \\ \frac{S^4 2^{18}}{3^6 \pi^3} e^{-\frac{S^2 64}{9\pi}}, & \text{GSE} \end{cases} \tag{A.15}$$

As we can see from Fig. (A.1), when $S \to 0$, the level spacing shows universal behavior of S^β scaling, resulting in different degrees of level repulsion [61, 73]. Moreover, the level spacings of the Gaussian ensembles are contrasted with the Poisson distribution ($P(S) = e^{-S}$) where the eigenvalues are statistically independent and no level repulsions exist.

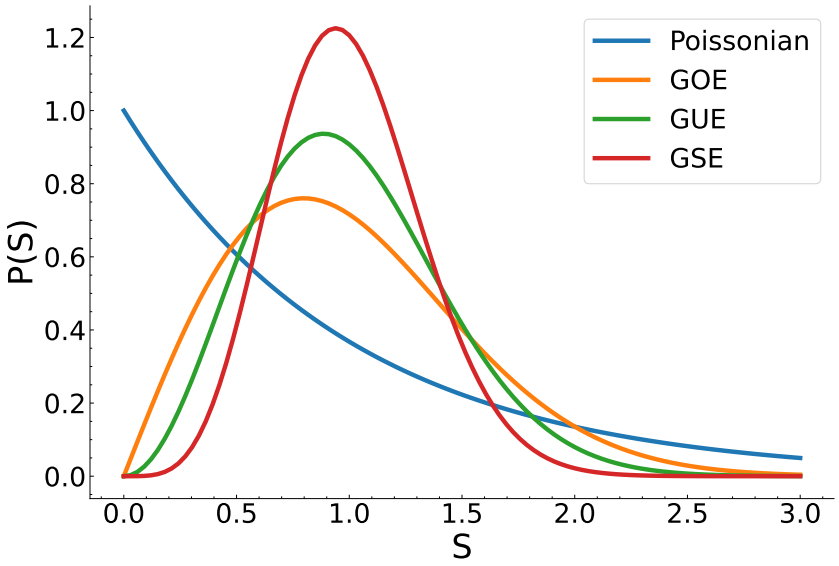

Figure A.1: The distribution for the nearest neighbor spacing of the eigenvalues, shown for the Poissonian, Gaussian orthogonal, Gaussian unitary, and Gaussian symplectic ensembles.

A.2 Quantum Chaos

A.2.1 Connections to Random Matrix Theory

As mentioned above, it is difficult to characterize dynamical chaos in quantum mechanics due to the Heisenberg uncertainty principle. Non-linearity as an important ingredient of chaos in classical physics is also not clearly presented in dynamics governed by the Schrodinger equation, a linear partial differential equation. Instead, chaos emerge in quantum mechanics from the discrete energy spectrum as if all the energies were randomly sampled from a probability distribution. This is known as spectral chaos [61, 73]. Therefore, we can apply RMT to observe universal behaviors of the spectra according to the symmetry of the Hamiltonian. The first experimental evidence comes from the complex spectra of heavy atomic nuclei, where the energy level spacings followed the GOE distribution as shown by Wigner. Surprisingly, quantum chaos also emerges from

condensed matter systems and the quantum nature of black hole physics, such as the Sachedev-Ye-Kitaev (SYK) model [74, 75].

In recent years, there have been large improvements in our understandings of quantum chaos. Berry-Tabor conjecture states that for a quantum system whose classical counterpart is integrable, the eigenenergies exhibit Poisson statistics [62]. It also means that there is no level repulsion in the system, and massive degeneracies are present. In contrast, quantum analogues of classically chaotic systems can be described by random matrices. The Bohigas, Giannoni and Schmidt conjecture states that chaos manifests itself in the spectral properties of the Hamiltonian of a quantum system by exhibiting universal features which are the same as those of the spectrum of a random Hamiltonian matrix in the same symmetry class [61]. The three ensembles, GOE, GUE, and GSE are used for Hamiltonians with time reversal symmetry, without time reversal symmetry, and symplectic invariance, respectively.

A.2.2 Level Repulsion

The spectra of the Hamiltonians demonstrate energy level repulsions. As $S \to 0$, we have S^β scaling for the distribution of level spacings, so it is progressively less likely to have a level crossing with increasing β. Generically, when no level crossings occur due to the lack of symmetry, no degeneracy can be introduced. This gives rise to Landau-Zener avoided crossings as if the energy levels are repulsive to each other. When the Hamiltonians are driven periodically in time, we can apply Floquet theory and use the Floquet operators to describe the dynamics stroboscopically. In this case, one should use Dyson's circular ensembles of random unitary matrices instead of Gaussian ensembles of random Hermitian matrices [61].

A.2.3 Spectral Form Factors

Spectral chaotic behavior of the Hamiltonian of a quantum system can be translated to universal features of Gaussian ensembles of random Hermitian matrices with the same symmetry, such as level repulsion. One even more universal feature is the correlation function of two energy levels [76]. An integrable system follows Poissonian statistics and there is no correlation between the energies. From RMT, the n-point correlation function between energy levels is [61]:

$$\rho^{(n)}(E_1, ..., E_n) = \frac{N!}{(N-n)!} \int P(E_1, ..., E_N) dE_{n+1} ... dE_N \tag{A.16}$$

For the correlation function of two energy levels, we simply take $n = 2$. The spectral form factor is defined as the Fourier transform of the two-point correlation function [64]:

$$R_2(t) = \sum_{i,j} \int dE_i dE_j \rho^2(E_i, E_j) e^{i(E_i - E_j)t} \tag{A.17}$$

It is a measure of long-range correlations between eigenenergies of the Hamiltonian. Equivalently, it can be written as [65, 77]:

$$R_2(t) = \langle | \sum_n e^{-iE_n t} |^2 \rangle \tag{A.18}$$

When the system is chaotic, the spectral form factor displays a dip-ramp-plateau structure, which has been proposed to be one of the experimental measure for many-body quantum chaos [65].

The spectral form factor $R_2(t)$ can be decomposed to the sum of a disconnected part $R_2^{\text{disc}}(t)$ and a connected part $R_2^{\text{conn}}(t)$. For GUE, which describes the simplest Hamilto-

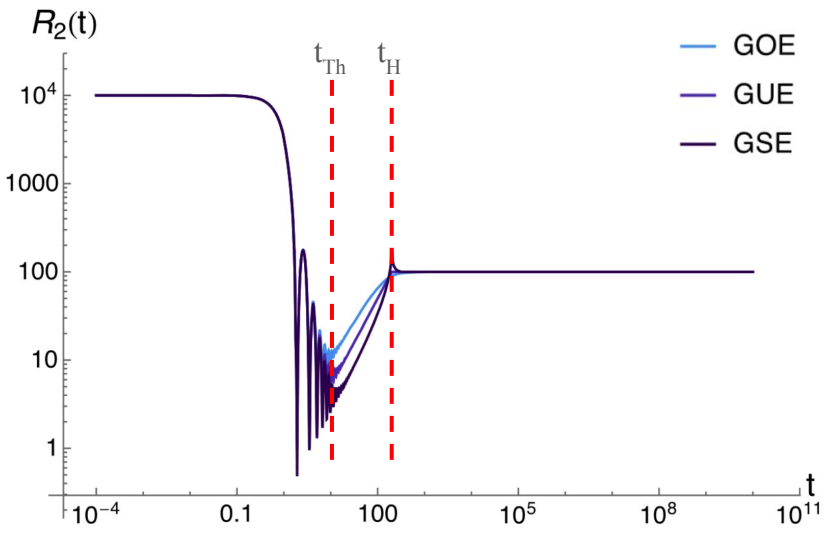

Figure A.2: The dip-ramp-plateau structure of the spectral form factor for the Gaussian orthogonal, Gaussian unitary, and Gaussian symplectic ensembles. The Thouless time t_{Th} corresponds to the end of the dip, and the Heisenberg time t_{H} represents the time at which the ramp stops. This figure is adapted from [64].

nian with no time reversal symmetry, they are [64, 77]:

$$R_2^{\mathrm{disc}}(t) = \left(\frac{J_1(2t)}{t}\right)^2 \sim \frac{1}{t^3} \tag{A.19}$$

$$R_2^{\mathrm{conn}}(t) = \begin{cases} \frac{t}{2N^2}, & t \leq 2N \\ \frac{1}{N}, & t > 2N \end{cases} \tag{A.20}$$

with J_1 being the 1$^{\mathrm{st}}$ Bessel function of the first kind. From Fig. A.2, we can see that the spectral form factor $R_2(t)$ is first dominated by the disconnected part $R_2^{\mathrm{disc}}(t)$ and decreases (dip) with a scaling of $\frac{1}{t^3}$ until the Thouless time t_{Th}. During this stage, the quantum correlations spread dynamically before reaching the boundary of the system, and hence the name Thouless time in analogous to the Thouless energy, the characteristic energy scale for the diffusive behavior in the Anderson model [78, 76]. At $t > t_{\mathrm{Th}}$, quantum correlations have been scrambled to a large extent across all length scales, and the system can be described by predictions from Gaussian ensembles in RMT. For

example, when compared to Eqn. (A.20), we can see that $R_2(t)$ for GUE in Fig. (A.2) increases linearly when $t_{\rm Th} < t < t_{\rm H}$. After the dip, the contribution from the connected part $R_2^{\rm conn}(t)$ becomes dominant, and it grows (ramp) before saturating (plateau) at the Heisenberg time $t_{\rm H} \equiv \frac{2\pi}{\langle E_i \rangle} = 2N$. The averaged energy spacing, $\langle E_i \rangle$, is the smallest energy scale, and consequently, the Heisenberg time t_H is the largest meaningful time scale.

A.3 Quantum Thermalization

In classical mechanics, we know that when a system thermalizes, it no longer contains its initial memory so that the long-time average of a measurement can be compared with the average obtained from the microcanonical ensemble. However, in quantum mechanics, if we consider a globally pure state $|\psi(t)\rangle = \sum_m C_m e^{-iE_m t} |m\rangle$, the time evolution of some local operator $\hat{O}$ can be written as:

$$\langle O(t) \rangle \equiv \langle \psi(t) | \hat{O} | \psi(t) \rangle \tag{A.21}$$

$$= \sum_{m,n} C_m^* C_n e^{i(E_m - E_n)t} O_{mn} \tag{A.22}$$

$$= \sum_m |C_m|^2 O_{mn} \tag{A.23}$$

$$+ \sum_{m,n \neq m} C_m^* C_n e^{i(E_m - E_n)t} O_{mn} \tag{A.24}$$

In the exponentially long time average, the second term vanishes. However, it seems that the measurements of $\langle O(t) \rangle$ would always store the initial conditions of $|C_m|^2$, which at first sight violates the condition that thermalization implies lost of initial information. One might conclude that thermalization cannot occur in a quantum system. However, if the Hamiltonian can be described using RMT, that is when the system is non-integrable, we know from Eqn. (A.8) how to express the matrix elements of this operator $\hat{O}$. Specif-

ically, if we consider a large system size:

$$\langle O \rangle = \sum_m |C_m|^2 O_{mm} \approx \overline{O} \sum_m |C_m|^2 = \overline{O} \tag{A.25}$$

which is the results from the microcanonical description and no longer requires initial conditions of the quantum system. We then have:

$$\lim_{t_\mathrm{f} \to \infty} \frac{1}{t_\mathrm{f}} \int_0^{t_\mathrm{f}} dt \, \langle O(t) \rangle = \overline{O} \tag{A.26}$$

In real physical systems, however, that the expectations values of observables depend on the temperature of the system. In addition, all the information in the off-diagonal matrix elements of $\hat{O}$ is lost from the RMT prediction.

A.3.1 Eigenstate Thermalization Hypothesis

In 1999, Srednicki provided a new ansatz for O_{mn} expressed in the eigen-basis of the Hamiltonian [79, 80]:

$$O_{mn} = \overline{O}(\overline{E})\delta_{mn} + e^{-\frac{S(\overline{E})}{2}} f_O(\overline{E}, w) R_{mn} \tag{A.27}$$

where $\overline{E}$ is the mean energy spacings, $w \equiv E_n - E_m$, and $S(\overline{E})$ is the thermodynamic entropy at energy E. $\overline{O}(\overline{E})$ and $f_O(\overline{E}, w)$ are smooth functions of their arguments. This is known as the Eigenstate Thermalization Hypothesis (ETH). This is different from the RMT prediction in Eqn. (A.8) in two ways: (i) $\overline{O}(\overline{E})$ is now a function of the mean energy spacings, rather than a constant for all the eigenstates. (ii) The off-diagonal elements also have dependence on $\overline{E}$, as well as the energy differences between eigenstates, introduced through the envelope function $f_O(\overline{E}, w)$.

Here, $\overline{O}(\overline{E})$ represents the microcanonical average at energy $\overline{E}$. The matrix element O_{mn} is always equal to the microcanonical average $\overline{O}(\overline{E})$ when we consider only diagonal elements (diagonal ensemble assumption) [62]. Note that we did not specific any requirement for the pure state nor make any assumptions on C_m, so we can take it to be simply a eigenstate of the Hamiltonian, and the long-time average of the observable $\hat{O}$ would still be equal to the microcanonical average. This is vastly different from classical mechanics, where we usually think the system reaches thermalization dynamically due to collision/interaction between particles. Quantum thermalization can occur at a single eigenstate level like each eigenstate contains a thermal state. Since Eqn. (A.27) doesn't involve any time dependence or require any time averaging, it means that the information of the thermal state already exits from the initial time. Time evolution of the system simply reveals, not creates, thermalization, through dephasing with vanishing off-diagonal elements [81]. The ETH is believed to hold true in a generic non-integrable many-body system, and otherwise, break down for a integrable system [63].

A.3.2 Entanglement Entropy

We considered above the operator $\hat{O}$ being local, and from ETH we learned that the stationary state of the measurement of $\hat{O}$ is equal to that described by a equilibrium thermal ensemble. In the thermodynamic limit, the microcanonical ensemble average can be replaced by the canonical ensemble average (the equivalence of ensemble) [62]. The subsystem upon which the local operator $\hat{O}$ acts can be thought of being in contact with a heat bath, namely the rest of the total system [82]. Therefore, measurements of $\hat{O}$ would indicate thermalization of the subsystem, despite globally the state being pure, because in general the subsystem would be a mixed state entangled with the rest of the system. The amount of entanglement could be quantified with the concept of

entanglement entropy. If we call the subsystem on which the operator $\hat{O}$ is defined A, and the rest of the system B, the entanglement entropy between A and B is defined as:

$$S_{AB} \equiv S_{\mathrm{VN}}(\hat{\rho}_A) = -\mathrm{Tr}_A[\hat{\rho}_A \ln \hat{\rho}_A] \tag{A.28}$$

where $\hat{\rho}_A$ is the reduced density matrix of A by taking partial trace over the subsystem B, $\hat{\rho}_A = \mathrm{Tr}_B[\hat{\rho}]$. Both theoretical and numerical work have indicated that the entanglement entropy is related to the thermodynamic entropy [81, 83, 84]. For homogeneous systems in the thermodynamic limit, finite energy eigenstates have an entanglement entropy equal to the thermodynamic entropy of the subsystem A (assuming A has a smaller system size than B) [85].

Bibliography

[1] I. Bloch, J. Dalibard, and W. Zwerger, *Many-body physics with ultracold gases*, *Reviews of Modern Physics* **80** (7, 2008) 885–964.

[2] A. Einstein, *Sitzungsberichte der Preussischen Akademie der Wissenschaften, Physikalisch-mathematische Klasse* (1924) 261.

[3] C. J. Pethick and H. Smith, *Bose–Einstein Condensation in dilute gases*. 9, 2008.

[4] W. Ketterle, D. S. Durfee, and D. M. Stamper-Kurn, *Making, probing and understanding Bose-Einstein condensates*, *arXiv (Cornell University)* (1, 1999).

[5] M. H. Anderson, J. R. Ensher, M. R. Matthews, C. E. Wieman, and E. A. Cornell, *Observation of Bose-Einstein condensation in a dilute atomic vapor*, *Science* **269** (7, 1995) 198–201.

[6] K. B. Davis, M. o. Mewes, M. R. Andrews, N. J. Van Druten, D. S. Durfee, D. M. Kurn, and W. Ketterle, *Bose-Einstein condensation in a gas of sodium atoms*, *Physical Review Letters* **75** (11, 1995) 3969–3973.

[7] C. Foot, *Atomic Physics*. Oxford University Press, USA, 1, 2005.

[8] Z. Geiger, *An Apparatus for Dynamical Quantum Emulation Using Ultracold Lithium*. Ph.D. Dissertation, UC Santa Barbara, 2017.

[9] K. Singh, *Floquet Engineering with Ultracold Lithium in Optical Lattices*. Ph.D. Dissertation, UC Santa Barbara, 2019.

[10] C. Fujiwara, *Dynamics of Ultracold Lithium in Modulated Optical Lattices*. Ph.D. Dissertation, UC Santa Barbara, 2019.

[11] R. Sajjad, *Driving Fast and Slow: Dynamics of Periodically Modulated Quantum Gases*. Ph.D. Dissertation, UC Santa Barbara, 2019.

[12] E. Q. Simmons, *(Thermo)Dynamics of Ultracold Quantum Degenerate Gases*. Ph.D. Dissertation, UC Santa Barbara, 2024.

[13] C. Chin, R. Grimm, P. Julienne, and E. Tiesinga, *Feshbach resonances in ultracold gases*, *Reviews of Modern Physics* **82** (4, 2010) 1225–1286.

[14] L. Salasnich, A. Parola, and L. Reatto, *Effective wave equations for the dynamics of cigar-shaped and disk-shaped Bose condensates*, *Physical Review A* **65** (4, 2002).

[15] O. Morsch and M. Oberthaler, *Dynamics of Bose-Einstein condensates in optical lattices*, *Reviews of Modern Physics* **78** (2, 2006) 179–215.

[16] R. Grimm, M. Weidemüller, and Y. B. Ovchinnikov, *Optical dipole traps for neutral atoms*. 1, 2000.

[17] J. J. Sakurai and J. Napolitano, *Modern Quantum Mechanics*. Cambridge University Press, 9, 2020.

[18] J. Dalibad, "Optical lattices." `https://pro.college-de-france.fr/jean.dalibard/CdF/2013/total_en_2013.pdf`, 2012. [Online Lecture Notes].

[19] M. S. Rudner and N. H. Lindner, *The Floquet Engineer's handbook*, 3, 2020.

[20] G. E. Santoro, "Introduction to Floquet." `https://www.ggi.infn.it/sft/SFT_2019/LectureNotes/Santoro.pdf`. [Online Lecture Notes].

[21] "Floquet Formalism." `https://qutip.org/docs/4.0.2/guide/dynamics/dynamics-floquet.html`. [QuTiP (Quantum Toolbox in Python) User's Guide].

[22] M. Holthaus, *Floquet engineering with quasienergy bands of periodically driven optical lattices*, *Journal of Physics B Atomic Molecular and Optical Physics* **49** (11, 2015) 013001.

[23] C. Weitenberg and J. Simonet, *Tailoring quantum gases by Floquet engineering*, *Nature Physics* **17** (8, 2021) 1342–1348.

[24] R. Thomas and N. Kjærgaard, *A digital feedback controller for stabilizing large electric currents to the ppm level for Feshbach resonance studies*, *Review of Scientific Instruments* **91** (3, 2020).

[25] M. Borkowski, L. Reichsöllner, P. Thekkeppatt, V. Barbé, T. Van Roon, K. Van Druten, and F. Schreck, *Active stabilization of kilogauss magnetic fields to the ppm level for magnetoassociation on ultranarrow Feshbach resonances*, *Review of Scientific Instruments* **94** (7, 2023).

[26] B. Merkel, K. Thirumalai, J. E. Tarlton, V. M. Schäfer, C. J. Ballance, T. P. Harty, and D. M. Lucas, *Magnetic field stabilization system for atomic physics experiments*, *Review of Scientific Instruments* **90** (4, 2019).

[27] H. Liu, S. Peng, B. Jiao, J. Li, and L. Luo, *Ultra-low noise bipolar current source for ultracold atom magnetic system*, *Review of Scientific Instruments* **94** (5, 2023).

[28] A. Keshet and W. Ketterle, *A distributed, graphical user interface based, computer control system for atomic physics experiments*, *Review of Scientific Instruments* **84** (1, 2013).

[29] X. Chai, "MuscleMuseum." `https://github.com/weldlabucsb/MuscleMuseum.git`, 2023.

[30] A. Mazurenko, S. Blatt, F. Huber, M. F. Parsons, C. S. Chiu, G. Ji, D. Greif, and M. Greiner, *Implementation of a stable, high-power optical lattice for quantum gas microscopy*, *Review of Scientific Instruments* **90** (3, 2019).

[31] M. Jaffe, P. Haslinger, V. Xu, P. Hamilton, A. Upadhye, B. Elder, J. Khoury, and H. Müller, *Testing sub-gravitational forces on atoms from a miniature in-vacuum source mass*, *Nature Physics* **13** (7, 2017) 938–942.

[32] X. Antoine, W. Bao, and C. Besse, *Computational methods for the dynamics of the nonlinear Schrödinger/Gross–Pitaevskii equations*, *Computer Physics Communications* **184** (8, 2013) 2621–2633.

[33] M. Thalhammer, "Lecture on time-splitting spectral methods for nonlinear schrödinger equations." `https://techmath.uibk.ac.at/mecht/MyHomepage/Research/SpringSchool_2009_Berlin.pdf`, 2009. [Online Lecture Notes].

[34] A. Cao, *Studying quantum dynamics in driven degenerate gases*. Undergraduate Dissertation, UC Santa Barbara, 2021.

[35] A. A. Michelson and E. W. Morley, *On the relative motion of the Earth and the luminiferous ether*, *American Journal of Science* **s3-34** (11, 1887) 333–345.

[36] LIGO Scientific Collaboration and Virgo Collaboration, *Observation of Gravitational Waves from a Binary Black Hole Merger*, *Physical Review Letters* **116** (Feb., 2016) 061102.

[37] J. Baudon, R. Mathevet, and J. Robert, *Atomic interferometry*, *Journal of Physics B Atomic Molecular and Optical Physics* **32** (8, 1999) R173–R195.

[38] A. D. Cronin, J. Schmiedmayer, and D. E. Pritchard, *Optics and interferometry with atoms and molecules*, *Reviews of Modern Physics* **81** (7, 2009) 1051–1129.

[39] D. W. Keith, C. R. Ekstrom, Q. A. Turchette, and D. E. Pritchard, *An interferometer for atoms*, *Physical Review Letters* **66** (5, 1991) 2693–2696.

[40] M. Kasevich and S. Chu, *Atomic interferometry using stimulated Raman transitions*, *Physical Review Letters* **67** (7, 1991) 181–184.

[41] A. Peters, K. Y. Chung, and S. Chu, *Measurement of gravitational acceleration by dropping atoms*, *Nature* **400** (8, 1999) 849–852.

[42] M. Abe, P. Adamson, M. Borcean, D. Bortoletto, K. Bridges, S. P. Carman, S. Chattopadhyay, J. Coleman, N. M. Curfman, K. DeRose, T. Deshpande, S. Dimopoulos, C. J. Foot, J. C. Frisch, B. E. Garber, S. Geer, V. Gibson, J. Glick, P. W. Graham, S. R. Hahn, R. Harnik, L. Hawkins, S. Hindley, J. M. Hogan, Y. Jiang, M. A. Kasevich, R. J. Kellett, M. Kiburg, T. Kovachy, J. D. Lykken, J. March-Russell, J. Mitchell, M. Murphy, M. Nantel, L. E. Nobrega, R. K. Plunkett, S. Rajendran, J. Rudolph, N. Sachdeva, M. Safdari, J. K. Santucci, A. G. Schwartzman, I. Shipsey, H. Swan, L. R. Valerio, A. Vasonis, Y. Wang, and T. Wilkason, *Matter-wave Atomic Gradiometer Interferometric Sensor (MAGIS-100)*, *Quantum Science and Technology* **6** (4, 2021) 044003.

[43] J. R. Williams, C. A. Sackett, H. Ahlers, D. C. Aveline, P. Boegel, S. Botsi, E. Charron, E. R. Elliott, N. Gaaloul, E. Giese, W. Herr, J. R. Kellogg, J. M. Kohel, N. E. Lay, M. Meister, G. Müller, H. Müller, K. Oudrhiri, L. Phillips, A. Pichery, E. M. Rasel, A. Roura, M. Sbroscia, W. P. Schleich, C. Schneider, C. Schubert, B. Sen, R. J. Thompson, and N. P. Bigelow, *Interferometry of Atomic Matter Waves in the Cold Atom Lab onboard the International Space Station*, *arXiv (Cornell University)* (2, 2024).

[44] C. D. Panda, M. J. Tao, M. Ceja, J. Khoury, G. M. Tino, and H. Müller, *Measuring gravitational attraction with a lattice atom interferometer*, *Nature* **631** (6, 2024) 515–520.

[45] H. Breuer and M. Holthaus, *Quantum phases and Landau-Zener transitions in oscillating fields*, *Physics Letters A* **140** (10, 1989) 507–512.

[46] H. P. Breuer and M. Holthaus, *Adiabatic processes in the ionization of highly excited hydrogen atoms*, *Zeitschrift für Physik D Atoms Molecules and Clusters* **11** (3, 1989) 1–14.

[47] K. Drese and M. Holthaus, *Floquet theory for short laser pulses*, *The European Physical Journal D* **5** (1, 1999) 119–134.

[48] L. Landau, *Zur theorie der energieubertragung i*, *Z. Sowjetunion* **1** (1932) 88–95.

[49] L. Landau, *Zur theorie der energieubertragung. II*, *Physikalische Zeitschrift der Sowjetunion* **2** (1932) 46.

[50] C. Zener, *Non-adiabatic crossing of energy levels*, *Proceedings of the Royal Society of London. Series A, Containing Papers of a Mathematical and Physical Character* **137** (1932), no. 833 696–702.

[51] M. Greiner, I. Bloch, O. Mandel, T. W. Hänsch, and T. Esslinger, *Exploring phase coherence in a 2D lattice of Bose-Einstein condensates*, *Physical Review Letters* **87** (10, 2001).

[52] H. Katori, K. Hashiguchi, E. Y. Il' inova, and V. D. Ovsiannikov, *Magic wavelength to make optical lattice clocks insensitive to atomic motion*, *Physical Review Letters* **103** (10, 2009).

[53] K. E. McAlpine, D. Gochnauer, and S. Gupta, *Excited-band Bloch oscillations for precision atom interferometry*, *Physical review. A/Physical review, A* **101** (2, 2020).

[54] X. Zhang, R. P. Del Aguila, T. Mazzoni, N. Poli, and G. M. Tino, *Trapped-atom interferometer with ultracold Sr atoms*, *Physical Review A* **94** (Oct., 2016) 043608.

[55] L. D. Landau, E. M. Lifshits, and E. M. Lifshits, *Mechanics*. Pergamon, 1, 1976.

[56] S. Rahav, I. Gilary, and S. Fishman, *Effective Hamiltonians for periodically driven systems*, *Physical Review A* **68** (7, 2003).

[57] F. L. Moore, J. C. Robinson, C. F. Bharucha, B. Sundaram, and M. G. Raizen, *Atom Optics Realization of the Quantum δ-Kicked rotor*, *Physical Review Letters* **75** (12, 1995) 4598–4601.

[58] A. Cao, R. Sajjad, H. Mas, E. Q. Simmons, J. L. Tanlimco, E. Nolasco-Martinez, T. Shimasaki, H. E. Kondakci, V. Galitski, and D. M. Weld, *Interaction-driven breakdown of dynamical localization in a kicked quantum gas*, *Nature Physics* **18** (9, 2022) 1302–1306.

[59] K. Singh, C. J. Fujiwara, Z. A. Geiger, E. Q. Simmons, M. Lipatov, A. Cao, P. Dotti, S. V. Rajagopal, R. Senaratne, T. Shimasaki, M. Heyl, A. Eckardt, and D. M. Weld, *Quantifying and controlling prethermal nonergodicity in interacting floquet matter*, *Physical Review X* **9** (10, 2019).

[60] I. Kovacic, R. Rand, and S. M. Sah, *Mathieu's Equation and its Generalizations: Overview of stability charts and their features*, *Applied Mechanics Reviews* **70** (1, 2018).

[61] F. Haake, *Quantum signatures of chaos*. Springer Berlin Heidelberg, New York, NY, 4th edition ed., 2018.

[62] L. D'Alessio, Y. Kafri, A. Polkovnikov, and M. Rigol, *From Quantum Chaos and Eigenstate Thermalization to Statistical Mechanics and Thermodynamics*, *Advances in Physics* **65** (May, 2016) 239–362. arXiv:1509.06411 [cond-mat].

[63] M. Ueda, *Quantum equilibration, thermalization and prethermalization in ultracold atoms*, *Nature Reviews Physics* **2** (Oct., 2020) 669–681.

[64] J. Liu, *Spectral form factors and late time quantum chaos*, *Physical Review D* **98** (Oct., 2018) 086026.

[65] A. K. Das, C. Cianci, D. G. A. Cabral, D. A. Zarate-Herrada, P. Pinney, S. Pilatowsky-Cameo, A. S. Matsoukas-Roubeas, V. S. Batista, A. d. Campo, E. J. Torres-Herrera, and L. F. Santos, *Proposal for many-body quantum chaos detection*, June, 2024. arXiv:2401.01401 [cond-mat].

[66] K. Hashimoto, K. Murata, and R. Yoshii, *Out-of-time-order correlators in quantum mechanics*, *Journal of High Energy Physics* **2017** (10, 2017).

[67] L. Asteria, H. P. Zahn, M. N. Kosch, K. Sengstock, and C. Weitenberg, *Quantum gas magnifier for sub-lattice-resolved imaging of 3D quantum systems*, *Nature* **599** (11, 2021) 571–575.

[68] L. Asteria, *Quantum gas magnification of ultracold atoms in optical lattices*, *Journal of Physics B Atomic Molecular and Optical Physics* (5, 2025).

[69] O. Penrose, *Foundations of statistical mechanics: a deductive treatment*. Dover Publications, Newburyport, 2014.

[70] E. Fermi, P. Pasta, S. Ulam, and M. Tsingou, *STUDIES OF THE NONLINEAR PROBLEMS*, Tech. Rep. LA-1940, 4376203, May, 1955.

[71] G. Livan, M. Novaes, and P. Vivo, *Introduction to Random Matrices - Theory and Practice*, vol. 26. 2018. arXiv:1712.07903 [math-ph].

[72] D. Wakeham, *CHAOS AND THERMALISATION*, .

[73] H.-J. Stöckmann, *Quantum Chaos: An Introduction*. Cambridge University Press, 1 ed., Oct., 1999.

[74] S. Sachdev and J. Ye, *Gapless spin-fluid ground state in a random quantum Heisenberg magnet*, *Physical Review Letters* **70** (May, 1993) 3339–3342.

[75] J. Maldacena and D. Stanford, *Remarks on the Sachdev-Ye-Kitaev model*, *Physical Review D* **94** (Nov., 2016) 106002.

[76] X. Chen and A. W. W. Ludwig, *Universal spectral correlations in the chaotic wave function and the development of quantum chaos*, *Physical Review B* **98** (Aug., 2018) 064309.

[77] O. Bouverot-Dupuis, S. Pappalardi, J. Kurchan, A. Polkovnikov, and L. Foini, *Random matrix universality in dynamical correlation functions at late times*, Sept., 2024. arXiv:2407.12103 [cond-mat].

[78] L. Colmenarez, D. J. Luitz, I. M. Khaymovich, and G. D. Tomasi, *Sub-diffusive Thouless time scaling in the Anderson model on random regular graphs*, *Physical Review B* **105** (May, 2022) 174207. arXiv:2201.04673 [cond-mat].

[79] M. Srednicki, *Chaos and quantum thermalization*, *Physical Review E* **50** (Aug., 1994) 888–901.

[80] M. Srednicki, *Does Quantum Chaos Explain Quantum Statistical Mechanics?*, 1994. Version Number: 2.

[81] M. Rigol, V. Dunjko, and M. Olshanii, *Thermalization and its mechanism for generic isolated quantum systems*, *Nature* **452** (Apr., 2008) 854–858.

[82] J. M. Deutsch, *Eigenstate Thermalization Hypothesis*, *Reports on Progress in Physics* **81** (Aug., 2018) 082001. arXiv:1805.01616 [quant-ph].

[83] J. M. Deutsch, H. Li, and A. Sharma, *Microscopic origin of thermodynamic entropy in isolated systems*, *Physical Review E* **87** (Apr., 2013) 042135.

[84] L. F. Santos, A. Polkovnikov, and M. Rigol, *Entropy of Isolated Quantum Systems after a Quench*, *Physical Review Letters* **107** (July, 2011) 040601.

[85] J. R. Garrison and T. Grover, *Does a single eigenstate encode the full Hamiltonian?*, *Physical Review X* **8** (Apr., 2018) 021026. arXiv:1503.00729 [cond-mat].